NOVEL TECHNOLOGIES AND TECHNIQUES FOR LOW-COST PHASED ARRAYS AND SCANNING ANTENNAS

A Dissertation

by

CHRISTOPHER TIMOTHY RODENBECK

Submitted to the Office of Graduate Studies of
Texas A&M University
in partial fulfillment of the requirements for the degree of

DOCTOR OF PHILOSOPHY

August 2004

Major Subject: Electrical Engineering

NOVEL TECHNOLOGIES AND TECHNIQUES FOR LOW-COST PHASED ARRAYS AND SCANNING ANTENNAS

A Dissertation

by

CHRISTOPHER TIMOTHY RODENBECK

Submitted to Texas A&M University
in partial fulfillment of the requirements
for the degree of

DOCTOR OF PHILOSOPHY

Approved as to style and content by:

Kai Chang (Chair of Committee)	Robert D. Nevels (Member)
Frederick J. Strieter (Member)	Donald G. Naugle (Member)
Chanan Singh (Head of Department)	

August 2004

Major Subject: Electrical Engineering

ABSTRACT

Novel Technologies and Techniques for Low-Cost Phased Arrays and Scanning Antennas. (August 2004)

Christopher Timothy Rodenbeck, B.S.; M.S., Texas A&M University

Chair of Advisory Committee: Dr. Kai Chang

This dissertation introduces new technologies and techniques for low-cost phased arrays and scanning antennas. Special emphasis is placed on new approaches for low-cost millimeter-wave beam control.

Several topics are covered. A novel reconfigurable grating antenna is presented for low-cost millimeter-wave beam steering. The versatility of the approach is proven by adapting the design to dual-beam and circular-polarized operation. In addition, a simple and accurate procedure is developed for analyzing these antennas.

Designs are presented for low-cost microwave/millimeter-wave phased-array transceivers with extremely broad bandwidth. The target applications for these systems are mobile satellite communications and ultra-wideband radar.

Monolithic PIN diodes are a useful technology, especially suited for building miniaturized control components in microwave and millimeter-wave phased arrays. This dissertation demonstrates a new strategy for extracting bias-dependent small-signal models for monolithic PIN diodes.

The space solar-power satellite (SPS) is a visionary plan that involves beaming electrical power from outer space to the earth using a high-power microwave beam. Such a system must have retrodirective control so that the high-power beam always points on target. This dissertation presents a new phased-array architecture for the SPS system that could considerably reduce its overall cost and complexity.

In short, this dissertation presents technologies and techniques that reduce the cost of beam steering at microwave and millimeter-wave frequencies. The results of this work should have a far-ranging impact on the future of wireless systems.

ACKNOWLEDGMENTS

My sincere thanks go to Dr. Chang. He has been my benefactor and counselor for so long -- since my junior year here at A&M. I owe him a continuing debt of gratitude. I also must thank Mr. Ming-yi Li for working with me throughout my graduate studies at A&M. He has been a great teacher, partner, and friend.

None of the PIN diode research presented in this Chapter VII would have been possible without Dr. James Carroll's mentorship and continued support even after my summer term at TriQuint ended. The work on broadband MMIC-based phased array transceivers presented in Chapter VI could hardly have been so successful without generous donations from Raytheon made possible by James Klein and Brad Heimer. My papers on reconfigurable grating antennas were markedly improved by the critiques of Dr. Julio Navarro. Dr. Nevels kindly lent me his personal notes on diffraction gratings, which have considerably enhanced the material presented in Chapter II.

There are many other engineers to acknowledge... the institutions which have provided me with funding for my graduate studies, the special professors on my committee at A&M who have given me so much encouragement, the wonderful mentors and coworkers I have had at TriQuint, and all my friends and fellow researchers at Texas A&M's microwave lab.

TABLE OF CONTENTS

CHAPTER Page

LIST OF TABLES

LIST OF FIGURES

FIGURE Page

FIGURE Page

FIGURE Page

CHAPTER I

INTRODUCTION

A vast array of consumer wireless applications is envisioned at millimeter-wave frequencies in areas ranging from mobile satellite communications to intelligent transportation. Some examples of emerging millimeter-wave wireless services are listed in Table 1.

Table 1. Emerging millimeter-wave consumer applications.

Application	**Frequency Band**
Local multipoint distribution systems	24 - 42 GHz
Broadband mobile satellite communications	30 - 31GHz
Highly localized wireless local area networks	59 - 64 GHz
Intersatellite links	59 - 71 GHz
Intelligent highway systems and intelligent transportation	76 - 77 GHz
Consumer radar and civilian airborne radiolocation	*Q*- through *W*-band

---

The journal model is *IEEE Transactions on Antennas and Propagation*.

These applications run a broad spectrum from 24 GHz to 110 GHz and from broadband communications to highway safety. Futurists have speculated that the future boom in millimeter-wave wireless systems could eventually eclipse the boom seen in the 1990s in the mobile telephony market. Using millimeter-wave frequencies has important advantages including broad bandwidth and high data rates, small antennas with high directivity, and a large amount of available spectrum. In contrast to most commercial wireless services currently being offered, many of the anticipated millimeter-wave applications require the capability to steer or redirect wireless signals to different positions in order to track a moving target or user. Unfortunately, current technology for steering and redirecting millimeter-wave wireless signals faces numerous obstacles such as exuberant cost and technological difficulties in integration. State-of-the-art phased arrays and smart antennas offer excellent speed and performance but require advanced integration procedures, sophisticated RF technologies, and considerable supporting electronic equipment. Additional requirements, such as broad bandwidth, multiple agile spot beams, and circular polarization further increase the overall system expense and complexity.

In order to broaden the opportunities for commercial applications at millimeter-wave frequencies, this dissertation presents novel technologies and techniques for low-cost phased arrays and scanning antennas. Although the work described herein encompasses several topics, all are related by this common goal.

Chapters III-V describe how versatile millimeter-wave scanning antennas and phased arrays can be produced inexpensively using novel reconfigurable grating antennas. These reconfigurable antennas achieve low loss and broad bandwidth at high millimeter-wave frequencies, can scan highly directive beams of radiation across wide angles, and are adaptable to dual-beam and circular-polarized operation. The approach used is to reconfigure an antenna aperture by scrolling a thin dielectric film across the surface of a stationary dielectric waveguide feed. Not only is this approach simple, inexpensive, and mass-producible, but it also is capable of steering an excellent radiation pattern across wide angles for a broad range of millimeter-wave frequencies.

The ability to accurately design and prototype these new reconfigurable antennas is critical to their eventual acceptance by industry. A simple and accurate analytical procedure is presented in Chapter IV and applied to the design of a dual-beam grating antenna. Unlike more rigorous approaches, the new simplified analysis is computationally economical and easy to implement. Unlike other approximate approaches, the new analysis is applicable for the complete range of practical grating dimensions.

An additional chapter is included in order to provide a broader context for the material in Chapters III-V. Chapter II provides technical background on grating antennas, describes their fundamental principles of operation, and discusses the current applications of gratings at millimeter-wave frequencies.

Recent advances in broadband RF and microwave components are making possible the realization of very broadband phased arrays for use in multi-frequency mobile satellite communications and in broadband radar. Chapter VI describes novel, broadband phased array architectures for these applications using some of the latest advances in broadband, low-cost microwave components. The system-level design for an 8 to 21 GHz phased array communication systems is presented, together with measured results describing system performance. In addition, designs for a 10 to 35 GHz communications system and an 8 to 20 GHz radar system are also presented.

Increasing the level of integration in a phased array is another method that can be used to decrease overall system cost. Monolithic PIN diodes can be used to miniaturize the phase shifters, switches, variable attenuators, and limiters commonly used in phased arrays. The diodes can be integrated onto monolithic microwave integrated circuits (MMICs) and directly interfaced with on-chip inductors, capacitors, and bipolar transistors. Chapter VII presents a bias-dependent small-signal modeling methodology for monolithic PIN diodes at frequencies up through 40 GHz. The methodology is demonstrated for a variety of diode sizes and geometries produced at TriQuint Semiconductor in Dallas. A number of interesting conclusions are made as a result of this work.

Chapter VIII demonstrates a novel phased-array architecture for retrodirective wireless power transmission from the space solar power satellite (SPS). Since 1968, aerospace engineers have dreamed of placing an SPS system in geosynchronous orbit to collect the sun's power, convert it to electricity, and beam it down to the earth using a high power microwave beam. On the earth's surface, the microwave beam can be received and converted back to electrical power on the gigawatt scale using a rectifying antenna array or "rectenna" array. To ensure maximum operating efficiency and to eliminate environmental concerns, the microwave transmission system requires retrodirective control. To accomplish this, a pilot beam signal should be transmitted from the rectenna site to the orbiting satellite so that the high-power microwave beam always points on-target. The phased array architecture proposed in Chapter VIII uses a 2.9-GHz pilot beam and a 5.8-GHz transmit beam, with retrodirective phasing implemented directly at RF in order to potentially reduce system cost and increase operating efficiency for the SPS application. Experimental and theoretical results are presented in order to validate this approach.

Chapter IX concludes this dissertation with a review and discussion of the relevant accomplishments of this work.

In summary, the research presented in this dissertation demonstrates new technologies for low-cost phased arrays and scanning antennas. Special emphasis is placed on developing low-cost approaches for beam steering at millimeter-wave frequencies where

cost becomes a critical issue. This work should have broad commercial applications in the emerging millimeter-wave wireless systems and a far-reaching impact on the future of wireless technology.

CHAPTER II

GRATINGS AND GRATING ANTENNAS*

A grating is an array of parallel obstructions separated from one another at a distance comparable to a wavelength. When an electromagnetic wave is incident upon a grating, it scatters to one or more specific angles determined by the spacing of the grating and the frequency of the wave. Since this effect is a diffraction phenomenon, gratings are often also referred to as diffraction gratings.

One of the most important uses of the diffraction grating is as an antenna for millimeter-wave through optical frequencies. This type of diffraction grating is the primary focus of this chapter. In integrated optics, grating antennas are used to couple power into and out of dielectric waveguides. For millimeter-wave systems, grating antennas have received attention because of several key advantages they have in comparison with other conventional microwave antennas. They have excellent radiation efficiency, they are inexpensive and easy to fabricate, and they are planar. There is also considerable interest in using grating antennas to implement low-cost beam steering at millimeter-wave frequencies.

---

* Parts of this chapter are reprinted from C.T. Rodenbeck and K. Chang, "Gratings and grating antennas," to appear in the *Wiley Encyclopedia of Microwave and RF Engineering*, vol. 1, K. Chang, Ed. New York: Wiley, 2004.

This chapter examines gratings and grating antennas in a series of four sections. Each of these sections is presented in such a way that it may be read independently from the others. An overview of the historical development of diffraction gratings is presented. The fundamental principles behind grating diffraction are explained in a manner suitable for those with an RF/microwave background. Grating antennas and some of their latest and most impressive applications at millimeter-wave frequencies are described. The chapter concludes with a brief discussion of the future of this field.

A. Historical Background

Despite its fundamental importance, the early origins of the diffraction grating are a remarkable tale of discovery and rediscovery. An intense period of research into optical technology had begun during the early 1600s following the invention of the telescope by the Dutch. During that century, the fundamental principles of refraction and diffraction were discovered and applied to numerous optical components such as lenses, mirrors, reflectors, slits, pinholes, etc. Gratings, however, were not invented until a much later date.

The first discovery of the diffraction grating occurred in Philadelphia in 1785. Francis Hopkinson, one of the signers of the Declaration of Independence, held a finely-woven silk handkerchief up to a bright light and observed the interference pattern produced by the light passing through the fabric. Hopkinson consulted his friend David Rittenhouse, a self-trained physicist. Recognizing the phenomenon as a diffraction effect,

Rittenhouse designed his own diffraction grating made of human hairs wound around two fine screws. He then used the device to measure the approximate wavelength of visible light. Hailing his invention in an American scientific journal, Rittenhouse exclaimed that "new and interesting discoveries may be made respecting the properties of this wonderful substance, light, which animates all nature in the eyes of man, and perhaps, above all things, disposes him to acknowledge the Creator's bounty" [1]-[3].

Since few researchers of that era read American scientific journals, Thomas Young of London had the opportunity to re-invent the diffraction grating in 1803. Young used his invention to measure the wavelengths of the various visible colors, but his main objective was to lend support to his view that light is a wave rather than a particle. Opponents of the wave theory attacked Young's work, labeling it as "destitute of every species of merit" [3], [4]. The practical importance of Young's invention was thus unfortunately lost amid the then viscous debate concerning the nature of light.

The grating would be discovered for the final time by Joseph von Fraunhofer in 1821. Fraunhofer had earlier established an optical company in Bavaria that produced optical components of the highest quality. After unexpectedly observing grating diffraction during an experiment, Fraunhofer built increasingly precise gratings, ultimately etching the profile of a grating directly onto the surface of a glass plate. Using this arrangement, Fraunhofer was able to separate visible light into the different colors and measure their wavelengths. Although his primary objective was to use the device to make precise

optical measurements and thereby improve his company's products, Fraunhofer did popularize additional uses for optical gratings, including chemical spectroscopy and astronomical observation [1]-[4]. After his death, the diffraction grating eventually became an indispensable component of optics. As one researcher put it in 1960, "It is difficult to point to another single device that has brought more important information to every field of science than the diffraction grating" [3].

The first use of gratings at radio frequencies came during Heinrich Hertz's revolutionary experiments in 1887 through 1891. Hertz used a narrowly-spaced wire grating in order to test the polarization of his "electric waves" [5], [6]. Shortly after Hertz's death in 1894, Chandra Bose of Calcutta built an impressive 60 GHz transmitter and receiver. During these experiments, Bose used a diffraction grating to measure the wavelength of his millimeter-wave source [7]. Subsequent decades saw rapid progress in the area of RF/microwave antennas and arrays. Early researchers in this area were heavily influenced by their familiarity with the already well-known diffraction grating. This is not surprising since gratings and array antennas are both governed by the same fundamental principles of wave interference. In fact, the designation "grating lobe" is still commonly used to refer to the additional maxima emitted by an array of widely spaced antennas.

The first grating antennas were developed and popularized at optical frequencies during the 1970s. Researchers at IBM etched a grating profile along the surface of a dielectric

waveguide and used the device to transmit and receive laser light [8]. Called a grating "coupler", this optical antenna is used in integrated optics for coupling optical power into and out of dielectric waveguides. In 1977, Tatsuo Itoh demonstrated the first microwave grating antenna at 15 GHz [9]. Shortly afterward, a team of researchers at the US Army Communications-Electronics Command presented the development of a 60-GHz grating antenna fabricated along a silicon dielectric waveguide [10]-[14]. The design established the grating antenna as a new kind of low-loss low-cost antenna for millimeter-wave frequencies. This work captured the interest of researchers worldwide. Progress was rapid and was aided by inherent similarities between grating antennas and earlier traveling wave antennas designed at lower microwave frequencies [15]-[17]. With increasing contemporary interest in the commercial and military applications of millimeter waves, much of the research on grating antennas published over the last twenty-five years is now receiving renewed attention. And what is more, new and exciting applications of this antenna continue to be developed and are beginning to find commercial success for a wide range of millimeter-wave applications.

B. Fundamental Principles

The early investigators who popularized gratings were intelligent men who were able to grasp the underlying principles of grating diffraction even before those principles had been formalized. Grating diffraction can in fact be accurately explained by an analogy between light and sound [1]:

> If a sudden sharp noise such as is made by clapping the hands together is reflected from a high flight of steps, the sound comes back to us as a musical note; in other words, the steps impress the element of periodicity upon the reflected disturbance, each step throwing off an echo wave…

Sound incident on the staircase scatters in different directions. Those directions are determined by the step spacing and by the wavelength of each tone. In the case of a grating, an electromagnetic wave incident on a periodic interface scatters in a direction determined by the grating spacing and frequency of the wave.

This section presents a brief description of the fundamental principles behind grating diffraction. The discussion draws on material found in [3], [18]-[21] and is crafted in a manner suited for those with an RF/microwave background.

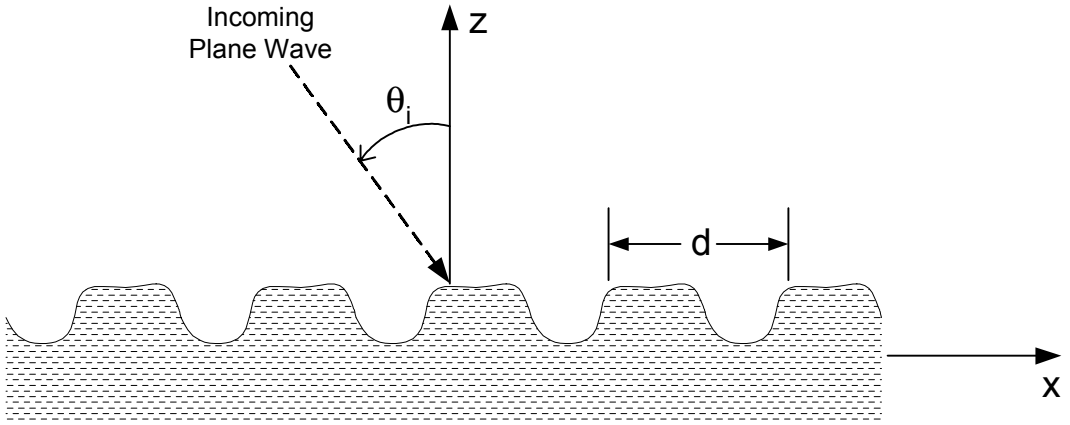

Fig. 1. A generalized reflection grating of periodicity *d* illuminated by a plane wave incident at the angle θ_i.

To begin with, consider the generalized two-dimensional grating interface shown in Fig. 1. The structure is infinite and periodic in the *x*-direction and is excited by a plane wave incident at the angle θ_i. Since the grating interface is periodic in *x*, the scattered field should also be periodic in *x*. This suggests that the scattered field can be expanded in terms of a Fourier series:

$$F_s(x,z) = \left[\sum_{n=-\infty}^{\infty} F_n(z) e^{-j\frac{2n\pi}{d}x} \right] e^{-jk_o(\sin\theta_i)x} \tag{1}$$

where $F_n(z)$ is the unknown Fourier coefficient for the n^{th} space harmonic $e^{-j\frac{2n\pi}{d}x}$. The $e^{-jk_o(\sin\theta_i)x}$ term outside the expansion accounts for the phase distribution of the incident field along the surface of the grating interface. Bringing that term within the expansion simplifies (1) to:

$$F_s(x,z) = \sum_{n=-\infty}^{\infty} F_n(z) e^{-jk_{x,n}x} \tag{2a}$$

where

$$k_{x,n} = k_o \sin\theta_i + \frac{2\pi n}{d} = k_o \sin\theta_n \tag{2b}$$

and θ_n denotes the angle of radiation for the nth space harmonic. Equation (2b) is the well-known "grating equation". By convention, θ_i and θ_n are defined so that θ_i is positive in the reverse quadrant and θ_n is positive in the forward quadrant.

Since the scattered field must satisfy the Helmholtz equation:

$$\nabla^2 F_s(x,z) + k_o{}^2 F_s(x,z) = 0 \ , \tag{3}$$

it is possible to define

$$k_{z,n} = \pm\sqrt{k_o{}^2 - k_{x,n}^2} = k_o \cos\theta_n \tag{4}$$

where the above sign is chosen to satisfy the radiation condition. The wave vector for the scattered field can now be expressed in terms of the unit vectors $\boldsymbol{u}_x$ and $\boldsymbol{u}_z$:

$$\boldsymbol{k_n} = k_{x,n}\boldsymbol{u_x} + k_{z,n}\boldsymbol{u}_z = k_o \sin\theta_n \boldsymbol{u_x} + k_o \cos\theta_n \boldsymbol{u}_z \ . \tag{5}$$

The incident wave vector likewise has the following form:

$$\boldsymbol{k_i} = k_o \sin\theta_i \boldsymbol{u_x} - k_o \cos\theta_i \boldsymbol{u}_z \ . \tag{6}$$

For a given incident angle θ_i and grating spacing d, it is possible to plot the incident and scattered wave vectors from (5) and (6) on an illustrative diagram. An example is shown in Fig. 2. All the radiating field vectors lie together on a unit circle of radius k_o, with each vector pointing in its direction of radiation. All the non-radiating field vectors lie outside this circle. These non-radiating or *evanescent* modes decay exponentially away from the surface of the grating. What makes this diagram is especially useful is that it gives the designer the ability to visualize how changing θ_i or d changes how many modes radiate and in which direction each radiates.

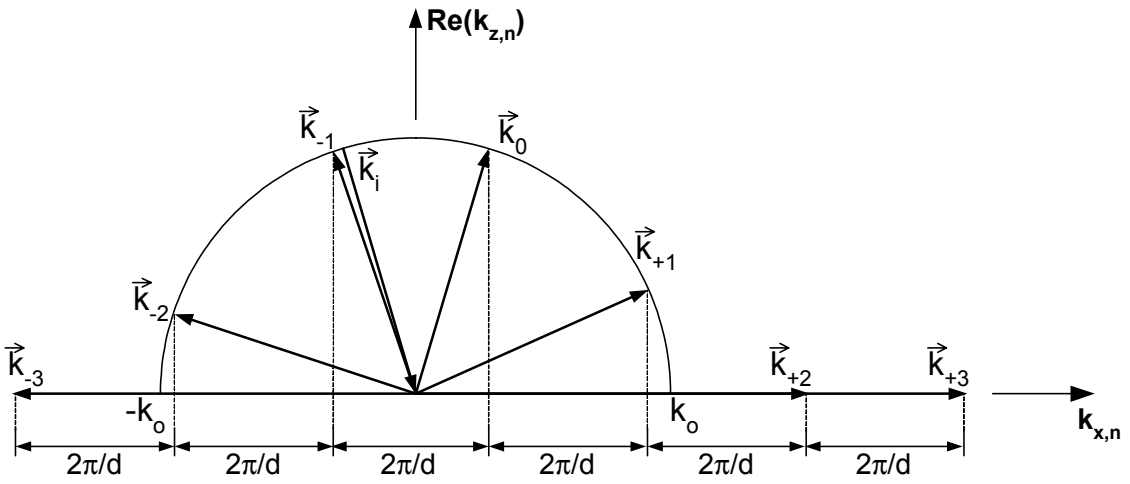

Fig. 2. Diagram illustrating the incident and scattered wave vectors from a hypothetical reflection grating.

In the case of a grating antenna, the grating interface lies along the surface of a dielectric waveguide, and the grating is excited by the signal propagating within that waveguide. The grating equation (2b) should then be rewritten as

$$k_{x,n} = k_{x,0} + \frac{2\pi n}{d} = k_o \sin\theta_n \tag{7}$$

where $k_{x,0}$ is the propagation constant within the dielectric waveguide. The scattered wave vectors from Equation (5) can be plotted as shown in Fig. 3. Each radiating space harmonic corresponds to a beam radiated by the antenna. Although grating antennas are typically designed so that only the $n = -1$ beam radiates, this example shows two radiating beams. The $n = -1$ beam is radiating in the forward quadrant ($\theta > 0°$), and the $n = -2$ beam in the reverse quadrant ($\theta < 0°$). This diagram can be used to design the grating so that a single main beam radiates in some desired direction.

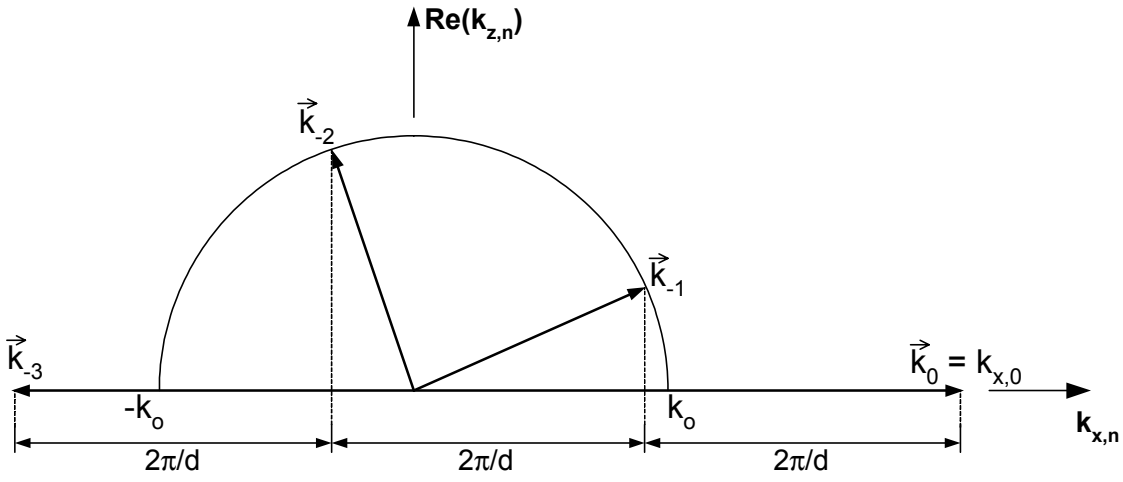

Fig. 3. Diagram illustrating the wave vectors along a hypothetical grating antenna.

C. Applications

The chief purpose of this section is not to present a comprehensive review of all applications of gratings and grating antennas. Instead, the objective is to capture the reader's interest and identify the major applications of gratings. A special emphasis is given to antenna applications at millimeter-wave frequencies.

1. Array Antennas

Grating antennas are based on dielectric waveguide technology. Unlike printed-circuit transmission lines, dielectric waveguides exhibit low loss even at very high millimeter-wave frequencies. Unlike rectangular metal waveguides, dielectric waveguides are easily fabricated and compatible with mass production at frequencies through *W*-band and beyond. Dielectric waveguides are thus ideal candidates for feeding millimeter-wave antenna arrays. Diffraction gratings are perhaps the most natural and inexpensive implementation of an array antenna to be based on this class of transmission line.

A conventional grating antenna is shown in Fig. 4. The grating antenna is a type of leaky-wave antenna. A leaky-wave antenna is essentially a waveguiding structure perturbed either continuously or periodically so that it leaks power all along its length [22]. In the case of a grating antenna, the waveguiding structure is a dielectric waveguide perturbed by a periodic grating placed along its surface. The conventional configuration is shown in Fig. 4. A periodic array of transverse strips is arranged along the surface of a dielectric waveguide, in this case a dielectric image line. The strips can

be either metallic or dielectric. These strips form a grating that perturbs the signal traveling along the guide. If the antenna is designed correctly, the grating excites a single leaky mode above the surface of the guide to create a directive beam of radiation in the far field. The radiated beam is fan-shaped, with narrow beamwidth in the array-effect dimension. The key design parameters for the antenna are the waveguide cross-section and dielectric constant, which determine the propagation constant inside the guide; the grating spacing d, which determines the angle of radiation θ; and the strip width w, which determines the rate of radiation along the antenna and the shape of the beam in the far field.

Many variations on the configuration in Fig. 4 are possible. The strips can be metal [10] or dielectric [23]. The strips can be replaced with slots, grooves, or cavities in the ground plane [24]. These strips, slots, and other perturbations don't necessarily have to be rectangular; they can also be circular. Their cross-sections can be "blazed" or non-rectangular [3]. In addition, the perturbations can be made self-similar to allow broadside radiation [24], [25]. If desired, the image line can also be replaced with another type of dielectric waveguide, such as insular image guide, nonradiative dielectric guide (NRD), inverted-strip dielectric guide, or rectangular dielectric waveguide [24]. Gratings fabricated on circular dielectric waveguides can radiate omnidirectionally [26]. Gratings based on rotated strips can radiate circular polarization [27], [28].

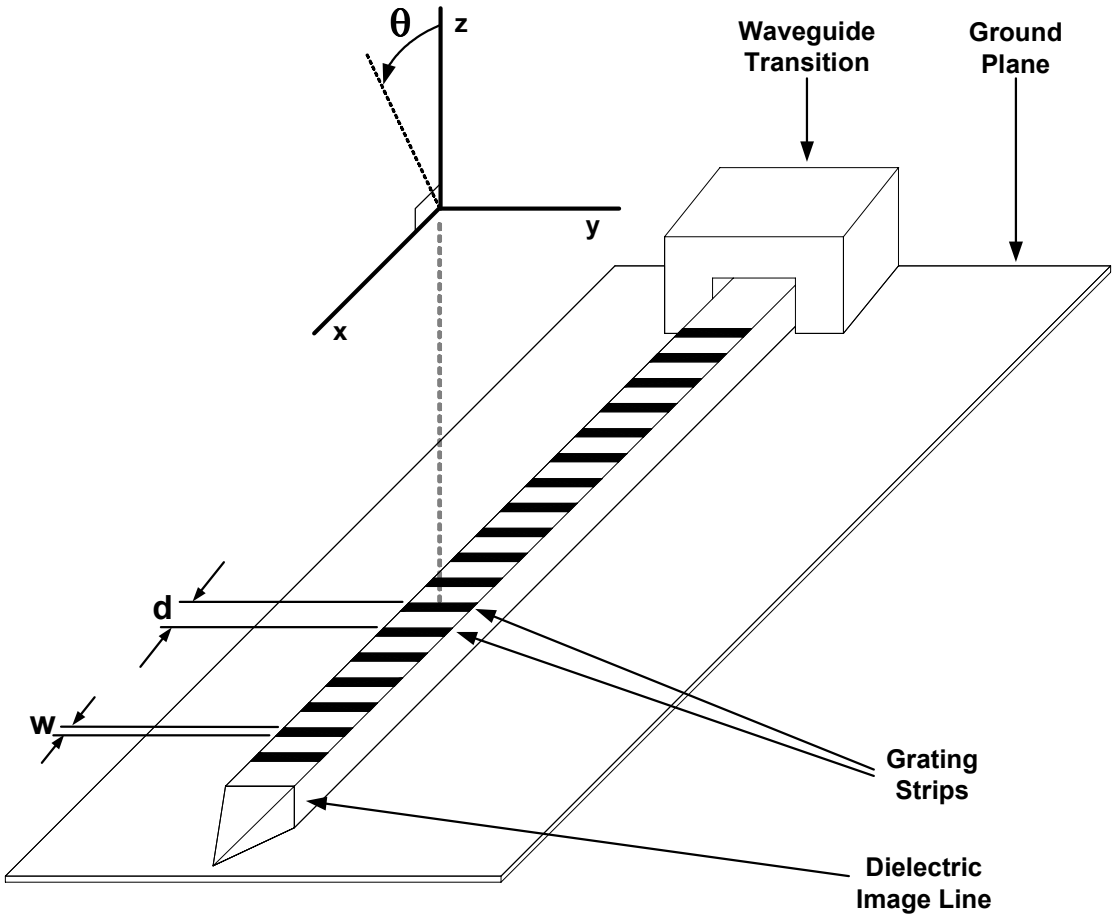

Fig. 4. Configuration of a conventional grating antenna.

Several methods are available for increasing the gain of a grating antenna. The gain in the non-array plane can be increased by embedding the dielectric guide within a trough [29] or flared trough [30] or by placing the guide in proximity to a parabolic reflector [31]. Pencil-beam radiation can be achieved by etching a two-dimensional grating on a surface-wave excited dielectric slab [32]-[34]. This kind of grating is designated a "hologram" or "holographic antenna". This is matter of nomenclature, however, since the standard grating antenna is itself a type of hologram. Other research has

demonstrated unconventional circular and linear polarized pencil-beam antennas fed by NRD gratings [35]. Planar arrays of grating antennas can also be formed to increase the directivity of the beam [36]. One planar grating array reported in the literature can radiate a broadside beam at 65 GHz with a total efficiency, including power divider and feed losses, of 27% [37].

2. Scanning Antennas

A wide array of consumer wireless applications is anticipated at millimeter-wave frequencies [38], [39]. Many of these emerging applications require the ability to track a user or moving target. Unfortunately, conventional technology for steering and redirecting millimeter-wave wireless signals is often prohibitively expensive for consumer applications. Rotating antennas use RF gimbal feeds that require precision machining and costly maintenance. Millimeter-wave phased arrays, on the other hand, are often exuberantly expensive, requiring exotic technologies and extensive supporting electronic equipment. In order to reduce the cost and broaden the commercial applications millimeter-wave frequencies, considerable research is currently directed at developing low-cost scanning antennas and phased arrays for the *Ka*-band and above. Several approaches based on the grating arrays are under investigation, including electromechanical, electronic, and electro-optic. Some of these approaches are also classified as "reconfigurable antennas" since the central tactic is often to provide beam-steering by reconfiguring the aperture of the grating.

The following chapter discusses a simple scanning antenna based on the grating antenna that can be electromechanically reconfigured to provide low-cost millimeter-wave beam steering. Another interesting electromechanical approach is to form a grating antenna from a spring coiled around a dielectric waveguide [40]. Flexing the spring provides beam steering. In addition, several interesting electromechanically scanning grating antennas are now available commercially and are disclosed in a US patent [31].

Other researchers are developing electronically-scanned grating antennas by integrating PIN diodes into the grating structure. In [13], [14], a PIN diode integrated into the sidewall of a grating antenna is used to modulate the propagation constant within the dielectric guide in order to steer the beam. In [41], PIN diodes are integrated into the grating strips themselves in order to switch the radiated beam between one of two scan states. Most impressively, in [34], an array of PIN diodes is integrated onto the back of a silicon wafer in order to create a dynamically reconfigurable hologram. Holographic antennas are the two-dimensional analog of grating antennas. Fig. 5 illustrates the conducting pattern formed by the PIN diodes on the silicon wafer and the corresponding far field pattern.

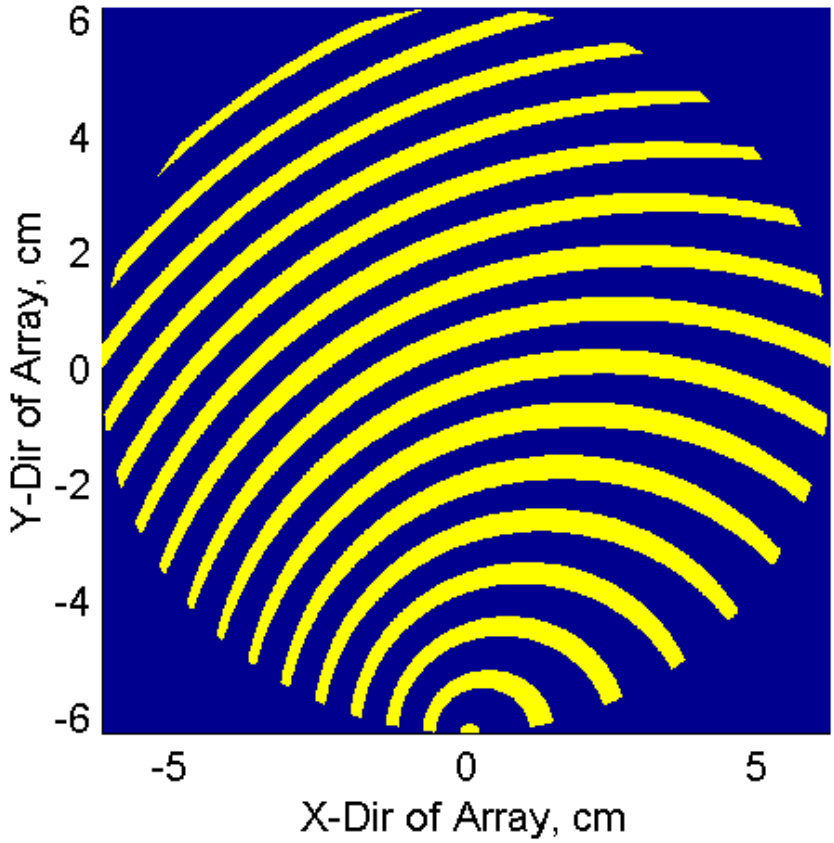

(a)

Fig. 5. Electronically-reconfigurable holographic antenna: (a) conducting regions formed on a silicon wafer and (b) corresponding far-field radiation pattern. (Courtesy of Dr. A. Fathy, University of Tennessee.)

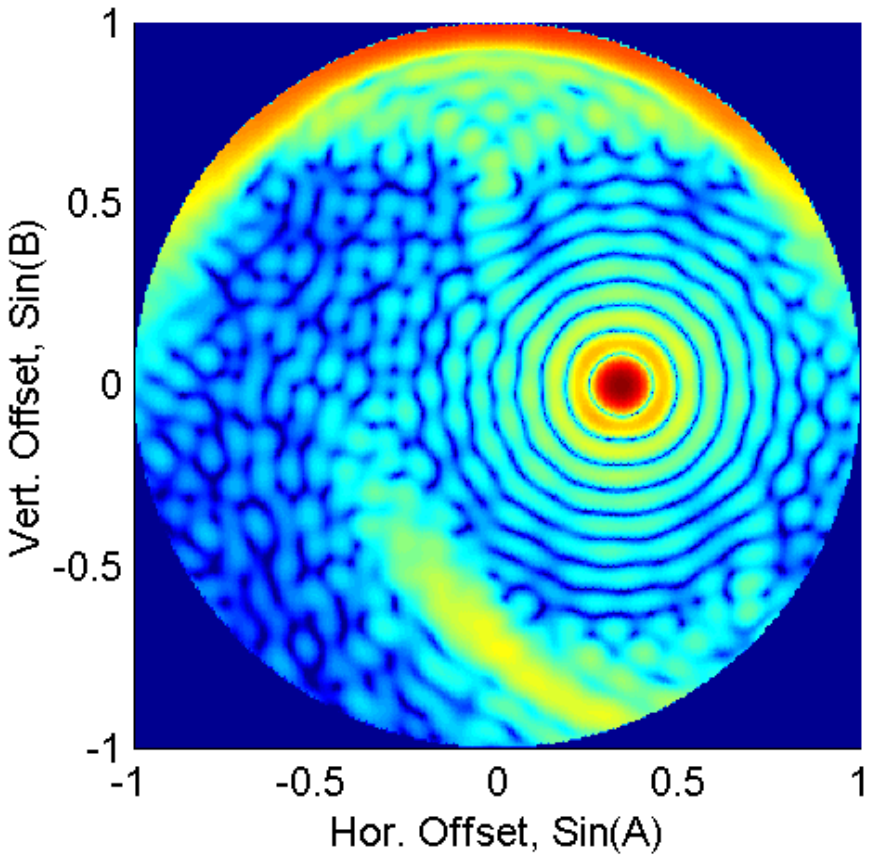

(b)

Fig. 5 continued.

Optical and ferro-electric scanning grating antennas are also a topic of investigation [42]-[47]. In many cases, however, the experimental results require improvement in order for the systems to find broad acceptance. Fig. 6 illustrates the configuration of one design [46]. A circular dielectric waveguide is coupled to a semiconducting dielectric slab. Laser light illuminates the surface of the dielectric slab in order to create islands of conducting plasma on the surface. The spacing between these islands can be changed in

order to steer the main beam angle of the radiated beam. Ferro-electric scanning grating antennas are also commercially available at frequencies from 10 to 76 GHz [47].

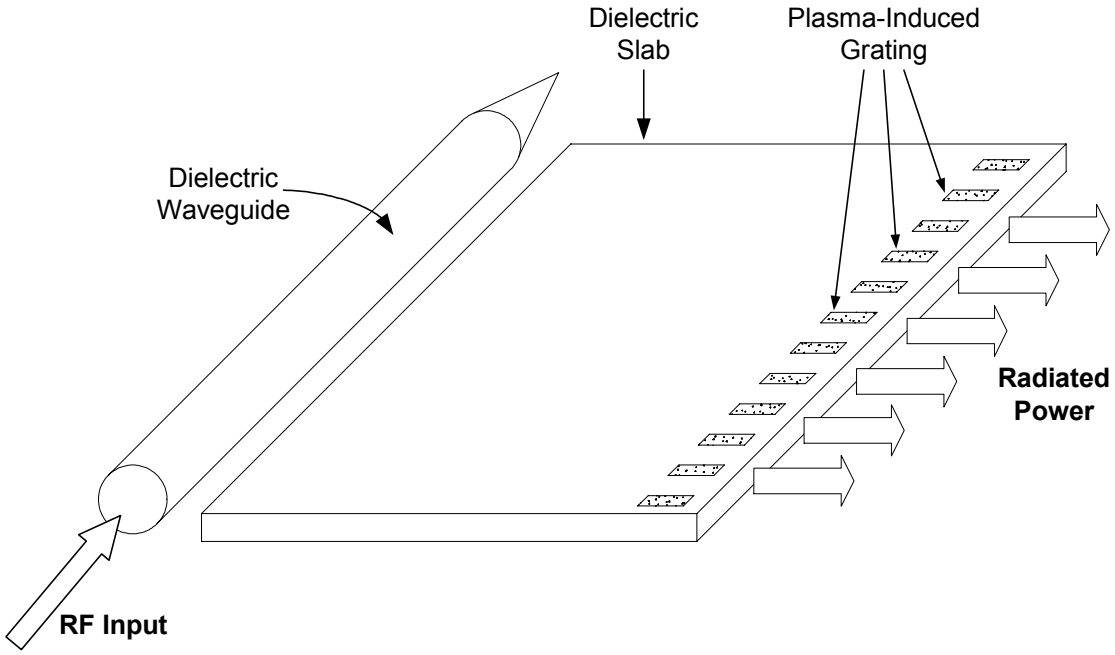

Fig. 6. A commercially available optically controlled grating antenna.

3. Other Applications

Many other uses for millimeter-wave gratings do exist. For example, on the circuit level gratings can be used as resonators for notch filters or for oscillators [9], [48]. Closely-spaced gratings are often used as polarizers in grid amplifiers [49]. In the far-field zone, millimeter-wave gratings are used for as spectrometry [7], [50], spatial filtering and beam shaping [51], spatial power combining and dividing [52]-[54], and remote beam control [55]-[57]. These applications are likely to increase in importance as millimeter-wave systems become more and more common.

D. Summary

Interest in millimeter-wave technology has been building steadily over the past 30 years. Today, several applications have already become established; numerous others are quickly emerging. These new millimeter-wave wireless systems require inexpensive, mass-producible, low-loss antenna arrays. Grating antennas meet these demands at frequencies up through the *W*-band and beyond.

CHAPTER III

MILLIMETER-WAVE BEAM-STEERING USING A DIELECTRIC-IMAGE-LINE-FED GRATING FILM*

This chapter presents a novel, broadband, low-cost technique for beam steering at millimeter-wave frequencies using a moveable grating film fed by dielectric image line. An excellent radiation pattern is maintained over wide scan angles across the 30 to 40 GHz range, with up to 53° scanning achieved at 35 GHz. Theoretical calculations closely predict the observed scan angle across the entire range of measurement.

A. Background

Several high-profile wireless applications are emerging at millimeter-wave frequencies in such areas as mobile satellite communications, local multipoint distribution systems, and intelligent cruise control. As wireless applications continue to diversify in this portion of the spectrum, there is an increasing demand in the commercial market for high-performance, low-cost methods of beam steering. Conventional phased-array systems and components suffer from significant tradeoffs between cost and performance at millimeter-wave frequencies. Interest in developing broadband, low-cost methods of

---

 Parts of this chapter are reprinted, with permission, from C.T. Rodenbeck, M. Li, and K. Chang, "A novel millimeter-wave beam-steering technique using a dielectric-image-line-fed grating film," *IEEE Trans. Antennas Propagat*., vol. 51, no. 9, pp. 2203-2209, Sept. 2003.

beam control in the millimeter-wave region has accordingly been the inspiration for much recent research.

Integrated dielectric guides are a promising technology finding application in wireless millimeter-wave systems. Like printed-circuit transmission lines, integrated dielectric guides are low-cost and mass-producible [10]. Unlike printed-circuit transmission lines, which suffer from inherently significant conduction losses at millimeter-wave frequencies, integrated dielectric guides have lower loss at higher frequencies, since most of the signal propagates within the low-loss dielectric region [57]. Thus, these transmission lines are excellent candidates for feeding millimeter-wave arrays. Several studies have demonstrated new beam-steering techniques using array-effect antennas fed by integrated dielectric guides [10], [12], [13], [30], [33], [39], [40], [42]-[46], [54]-[56], [58]-[63]. Unfortunately, these beam-steering techniques rely either upon frequency scanning, which is inconvenient in most system applications, or upon fixed-frequency techniques that display limited scanning, few scan states, or severe degradation of the antenna pattern across the scan range.

This chapter presents a simple new technique for millimeter-wave beam steering that uses a thin, moveable grating film fed by a stationary dielectric image line. Although leaky-wave antennas of the grating type are well described in literature [20], the concept and implementation reported here are unique and demonstrate a simple means of scanning a highly directive beam over a wide angle at frequencies across the 30 to 40

GHz range. No previously published work on scanning antenna arrays fed by integrated dielectric guide has demonstrated a continuous range of scanning comparable to the results presented here.

B. Concept

A general class of leaky-wave antenna can be constructed by placing dielectric or conducting strips periodically along a dielectric waveguide. The strips form a grating that perturbs the energy traveling along the guide, exciting leaky modes above the surface that determine the nature of the far-field pattern [20]. The radiated beam is fan-shaped, being highly directive in the array-effect dimension. Assuming the grating strips themselves have a negligible effect on the propagation constant along the perturbed guide, the angle of radiation in the direction forward from broadside can be calculated at any given frequency of excitation as a simple function of the guide wavelength λ_g and strip spacing d:

$$\theta_n = \arcsin\left(\frac{\lambda_o}{\lambda_g} + \frac{n\lambda_o}{d}\right), \qquad \left|\frac{\lambda_o}{\lambda_g} + \frac{n\lambda_o}{d}\right| \le 1 \tag{8}$$

where λ_o is the free space wavelength and n, the space harmonic (0, ±1, ±2, ···), is conventionally chosen as −1 for single beam operation [58]. Previous studies on scanning antennas of the grating type have focused on scanning θ_n by varying the operating frequency or by finding a means to modulate the guide wavelength. The

approach taken in this investigation is to alter the grating spacing d along the guide while leaving the guiding structure itself intact.

Fig. 7 illustrates the configuration of the proposed scanning antenna. A thin, moveable dielectric film is extended across a stationary dielectric image line. The portions of the film on either side of the image line are held in direct contact with the ground plane. Continuous metal grating strips are etched along the underside of the film, with the strips depicted as visible in the figure. The widths of these strips are designed to increase away from the input to the guide in order to gradually perturb the electromagnetic signal propagating along the image line. The spacing between the metal strips varies linearly along the length of the film from d_{max} to d_{min}. Scrolling the grating layer in the $\pm y$-direction varies the spacing between grating elements, scanning the radiated beam along θ in the xz-plane. The radiation pattern of the main beam is E-polarized in the x-direction, with the angle of radiation given by Equation (8).

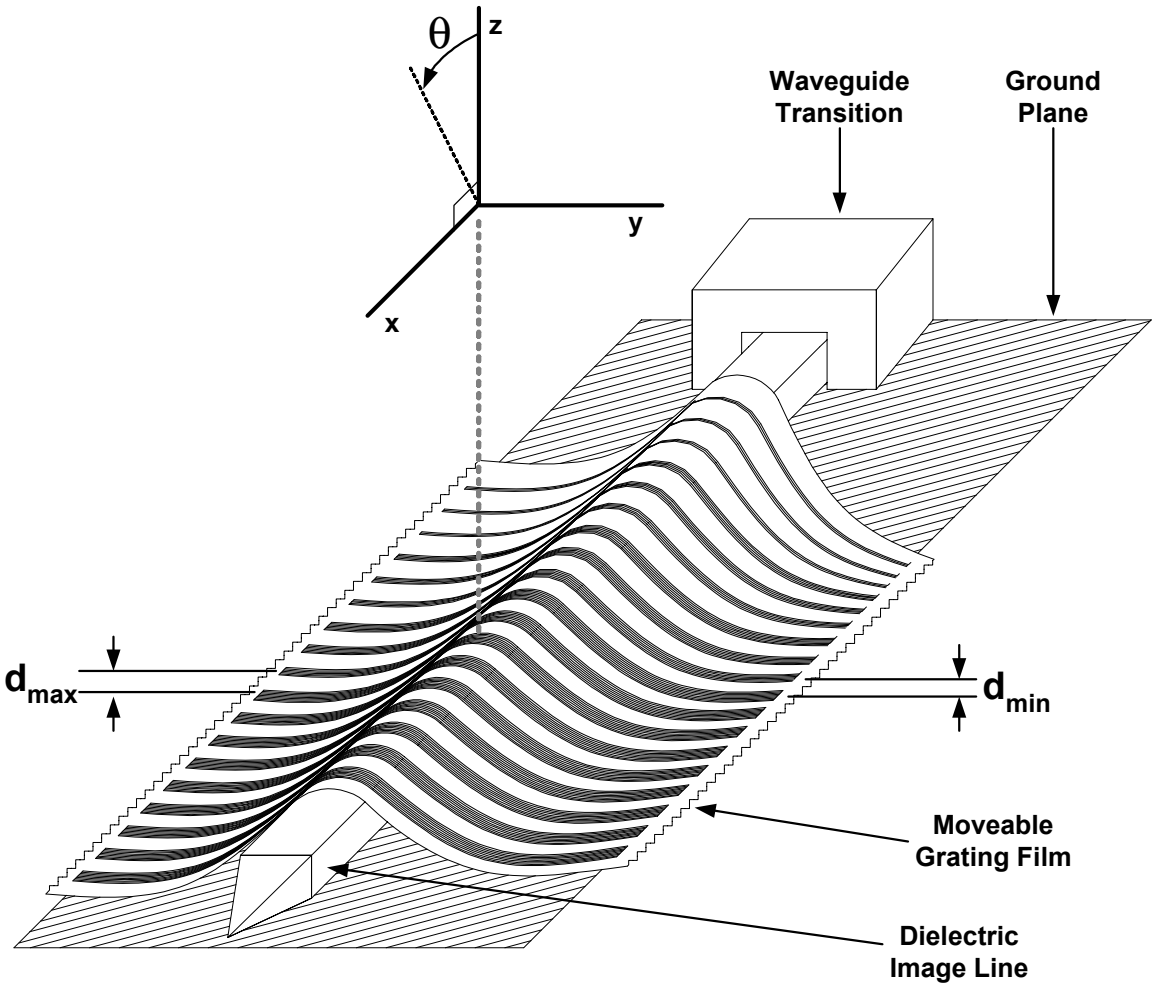

Fig. 7. Scanning antenna configuration.

By using a sufficiently wide image line and sufficiently thin, flexible grating film, the curvature of the film above the image line can be minimized. Other mechanical implementations for the grating layer are also possible – for example, using a thin, flat, rigid material rather than a flexible film. In the case of the thin, flexible film used in this study, a variety of low-profile electromechanical implementations can be used, in practice, to reposition the grating layer along the dielectric image line. One simple

technique would be to spool the film along the image line much as a printing press spools paper. In addition, although the design presented in this study uses continuous grating strips to achieve continuous beam steering, discrete sets of grating strips can instead be etched on the moveable dielectric film if continuous beam steering is not required, as shown in Fig. 8. Depending on the number of scan states required, such an arrangement could permit the overall film size to be reduced.

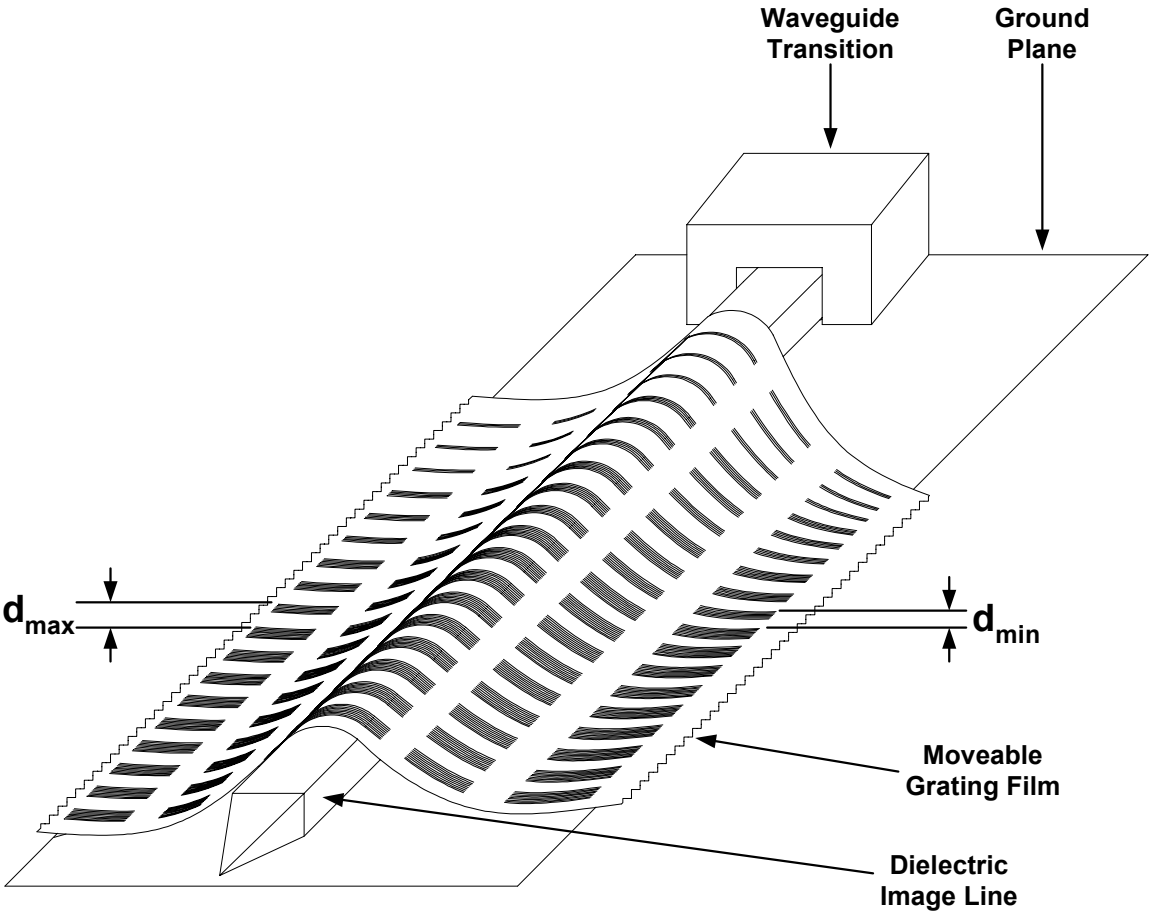

Fig. 8. An alternative implementation of the technique using discretized grating strips.

C. Theory and Design

Image line, like any other refractive waveguide, supports degenerate E^z_{mn} and E^y_{mn} hybrid modes. Referring to the coordinate system of Fig. 7, the primary field components of the E^z_{mn} modes are TM-to-z. Likewise, the primary field components of the E^y_{mn} modes are TE-to-z [23]. The presence of the ground plane, however, shorts out most of the E^y_{11} mode, allowing single-mode propagation over a considerable frequency range using the dominant E^z_{11} mode [63]. Suppose an image line has a relative dielectric constant ε_r, width $2a$ and height b, as shown in Fig. 9. If ε_r is "small" and the aspect ratio $2a/b$ is "large", the propagation characteristics of the E^z_{mn} modes can be simulated using an approximate technique [20], [64]. Referring to the coordinate system shown in Fig. 9, the transverse propagation constants k_y and k_z and longitudinal propagation constant k_x can be determined for particular values of m and n by simultaneous solution of the following set of coupled, transcendental equations:

$$ak_y = \frac{m\pi}{2} - \arctan\left\{ k_y \left[\left(\varepsilon_r - \left(\frac{k_z}{k_o} \right)^2 - 1 \right) k_o^{\,2} - k_y^{\,2} \right]^{-1/2} \right\}, \; m = 1,\ 2,\ 3\ \ldots \tag{9a}$$

$$bk_z = \frac{n\pi}{2} - \arctan\left\{ k_z \cdot \frac{1}{\varepsilon_r} \left[(\varepsilon_r - 1) k_o^{\,2} - k_z^{\,2} \right]^{-1/2} \right\}, \; n = 1,\ 2,\ 3\ \ldots \tag{9b}$$

$$k_x = \sqrt{\varepsilon_r k_o^{\,2} - k_y^{\,2} - k_z^{\,2}} \tag{9c}$$

where k_o denotes the free-space propagation constant at a specific frequency of excitation. The guided wavelength $\lambda_{g,mn}$ of the E^z_{mn} mode is given by $2\pi/k_{x,mn}$.

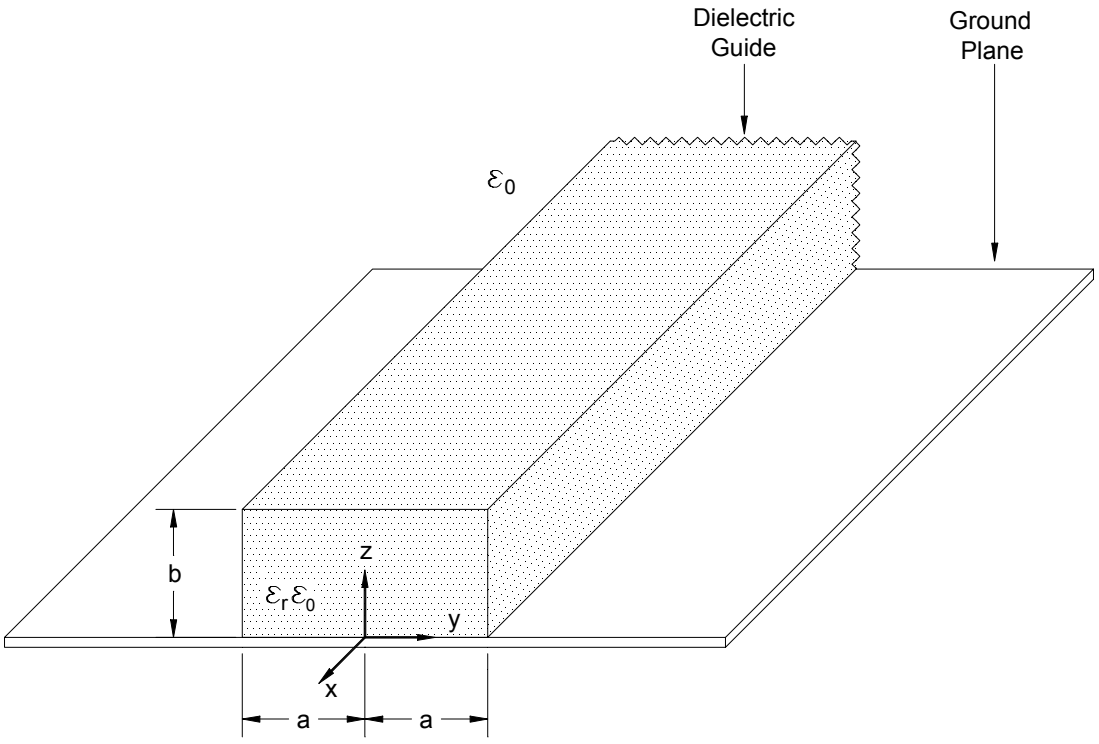

Fig. 9. Image line configuration.

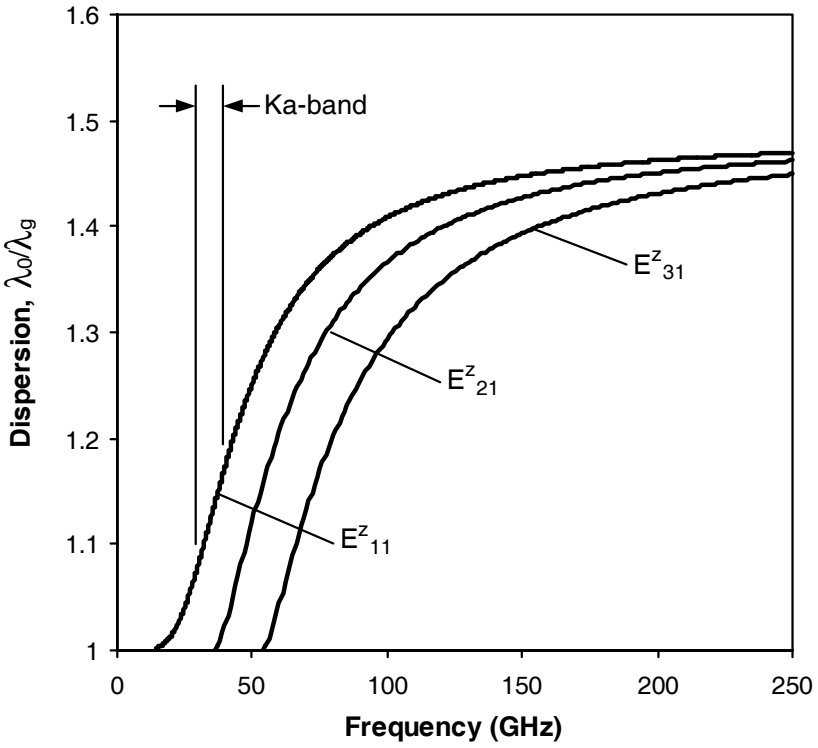

Fig. 10. Calculated dispersion of the guided wavelength along the dielectric image line for the fundamental mode and next two highest order E^{y}_{mn} modes with $\varepsilon_r = 2.2$, $a = 3.30$ mm, and $b = 1.57$ mm.

The image line feed incorporated into the novel scanning antenna featured in this study is fabricated from a 165-mm long strip of RT-Duroid 5880 ($\varepsilon_r = 2.2$) and bonded to an aluminum ground plane using low-loss dielectric epoxy. The cross-section dimensions, $a = 3.30$ mm and $b = 1.57$ mm, are designed in order to support a well-guided dominant mode across the *Ka*-band while allowing the image line to fit comfortably within the waveguide transition described in [65]. A microstrip-to-image-line transition can also be used [66]. The image line is terminated with a strip of Arc DD-10214 *Ka*-band silicone

absorber in order to prevent the reflection of any unradiated power from the open end of the antenna. Simulated dispersion curves, generated using (9), are shown in Fig. 10 for the fundamental mode and next two highest order E^z_{mn} modes.

The dielectric film is also fabricated from RT-Duroid 5880, using a substrate 0.13 mm thick. Designing the grating pattern etched onto this film involves several basic steps: (*i*) designing the maximum and minimum spacings between the grating strips, (*ii*) designing the number of grating strips, and (*iii*) designing the tapered distribution of strip widths along the surface of the image line. To begin with, the simulated value for $\lambda_{g,11}$ at the chosen center frequency of 35 GHz is obtained using (9). Substituting this value into (8) makes it possible to choose the maximum and minimum spacings between the strips in order to obtain the full range of scanning for the first space harmonic at the 35 GHz design center frequency. The designed values for d_{max} and d_{min}, as identified in Fig. 7, are chosen to be 8.60 mm and 4.56 mm, respectively. In practice, neither the first nor the second space harmonic (n = -1 and n = -2, respectively) radiates well for θ_n less than about -50°, thus limiting the useful scanning range of this antenna to those angles for which $\theta_{-1} > -50°$ and $\theta_{-2} < -50°$.

To allow convenient measurement up to 40 GHz in an available indoor far-field antenna range, the length of the entire structure shown in Fig. 7 is limited to 19 cm. This correspondingly limits the length of the film along the x-direction to 165 mm and the number of grating strips to 18. It is important to note that designs not constrained by the

far-field distance of the measurement facility have the additional degree of freedom to choose the length of the antenna in order to control the amount of residual unradiated power terminated at the end of the image line [22].

The final step in the design of the grating film is to design the tapered distribution of strip widths. The widths of the grating strips determine the rate of radiation along the antenna and, correspondingly, the amplitude distribution along the surface of the antenna. Although most grating antenna designs that appear in the literature use grating strips of uniform width, there exists a direct tradeoff between the chosen strip width and the performance of the antenna. Narrow strips radiate less efficiently, while wide strip widths, on the other hand, are associated with high side lobe levels [20]. Experimental investigations, however, have shown that tapering the distribution of strip widths can significantly reduce the observed side lobe level. Narrow strips near the input to the guide gradually perturb the signal launched along the guide; wide strips near the output to the guide radiate power more efficiently. In addition, by providing more optimal conversion of the guided wave to the radiating wave, the gradually increasing radiation rate along a tapered distribution of strip widths can produce a narrower beamwidth than can be achieved using the constant radiation rate along a uniform distribution of strip widths [29].

Numerous analytical approaches are available for characterizing the radiation rate along metal-strip grating antennas. Partial summaries of the various analyses are found in

[67]-[69]. Unfortunately, these methods can become considerably involved for designs using strips wider than 0.2*d* [67], after which experimental methods begin to gain favor [20]. This investigation draws on the empirical guideline suggested in [29], which uses

$$w_m = \begin{cases} \left(0.15 + 0.015\left(m-1\right)\right)\lambda_g, & m \le 18 \\ 0.4\lambda_g, & m > 18 \end{cases} \tag{10}$$

where w_m is the width of the m^{th} strip and $d \approx \lambda_g$ is assumed. To determine the distribution of strip widths along the entire continuous grating film shown in Fig. 7, the simulated value for λ_g at 40 GHz is obtained from (9) and used in (10) to calculate a set of strip widths. These strip widths are separated by an inter-element spacing equal to the simulated value for λ_g at 40 GHz. The width of each continuous grating strip is then scaled along the length of the film to increase or decrease linearly as the spacing between strips increases or decreases between d_{max} and d_{min}. The calculated width varies from 1.255 mm to 3.359 mm at $d_{max} = 8.60$ mm and from 0.663 mm to 1.782 mm at $d_{min} = 4.65$ mm. Experimental results indicate that this tapered design produces side lobes at close to the same power level as the spurious radiation emitted over the region $45° < \theta < 90°$ by the simple waveguide-to-image-line transition [65] used in this study. As demonstrated in the following section, this design preserves an excellent radiation pattern over a wide range of scan angles across the entire 30 to 40 GHz band.

D. Measured Performance

Fig. 11 illustrates the measured and calculated main-beam angle of the scanning antenna as the element-to-element spacing of the perturbing grating is varied along the guide. Over the entire range shown in Fig. 11, maximum side-lobe levels are at least 10 dB below the main beam. Averaging over all scan states, the typical maximum side-lobe level is greater than 13 dB below the main beam. 32° scanning is achieved at 30 GHz, 53° at 35 GHz, and 35° at 40 GHz. The calculated values for the main-beam angle of (8) are generated using simulated values from (9) for the dispersion of $\lambda_{g,11}$ along the image line. This calculation includes the 0.13-mm thickness of the grating film in the overall image line height but neglects the perturbational effect of the metal grating strips on the guided wavelength of the signal propagating along the image line. The resulting curves accurately predict the measured scan angle across the entire range of measurement.

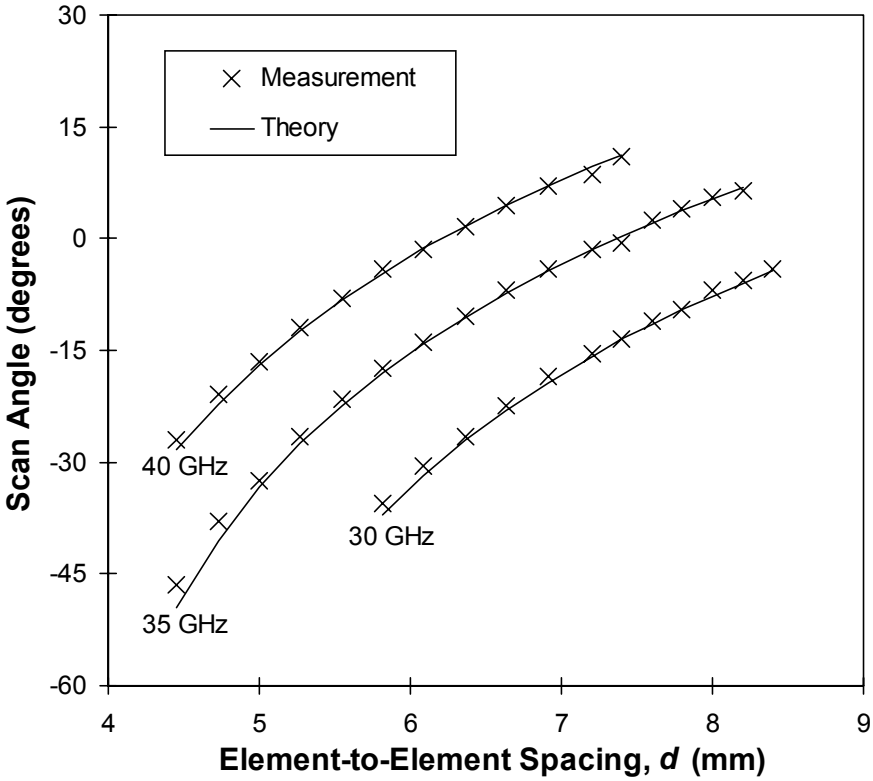

Fig. 11. Measured and calculated beam scanning along the θ-direction at 30, 35, and 40, GHz.

Fig. 12 displays the main-beam gain and 3-dB beamwidth as a function of element-to-element spacing. Isotropic gains observed at 30, 35, and 40 GHz are 17.7 ± 1.5 dBi, 19.1 ± 1.7 dBi, and 19.0 ± 1.2 dBi, respectively. For applications requiring greater gain flatness across the scanning range, additional grating elements may be added to the film as the spacing between elements narrows to effectively compensate for the rolloff in gain as the beam steers away from broadside. The gains recorded in Fig. 12 include the termination loss at the end of the image line, the loss of the waveguide-to-image-line

transition, and the return loss from the antenna. The unradiated power measured at the end of the image line for each discrete scan angle shown in Fig. 11 varies from 0.7 to 3.4% at 30 GHz, from 5.9 to 12.5% at 35 GHz, and from 3.0 to 16.3% at 40 GHz. The loss of the waveguide-to-image-line transition is 0.76 dB at 30 GHz, 0.74 dB at 35 GHz, and 0.56 dB at 40 GHz. The return loss varies as a function of the element-to-element spacing, as indicated in Fig. 13. Return losses are typically below -15 dB across the scanning range. The grating structure itself, however, exhibits a stopband resonance when $d = \lambda_g$ [58]. At this grating spacing, incremental reflections from each perturbing element add in-phase at the input port so that a significant percentage of the power directed to the grating reflects back toward the source. This effect causes the return loss to increase and the gain to drop significantly within a narrow range of $\theta = 0°$. Referring to Fig. 12, the depression in gain is weakly noticeable in the 40 GHz scan at d = 6.2 mm but more pronounced in the 35 GHz scan for d = 7.6 mm.

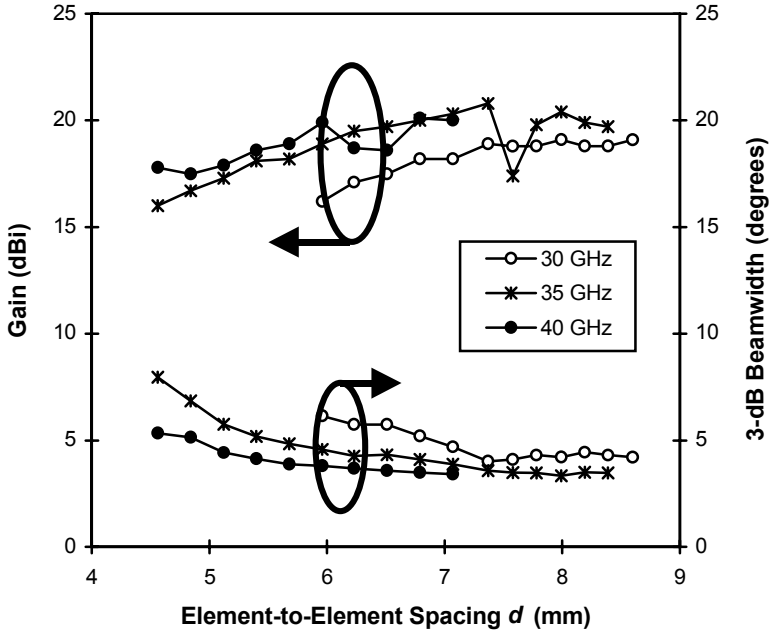

Fig. 12. Gain and 3-dB beamwidth versus element-to-element spacing at 30, 35, and 40 GHz.

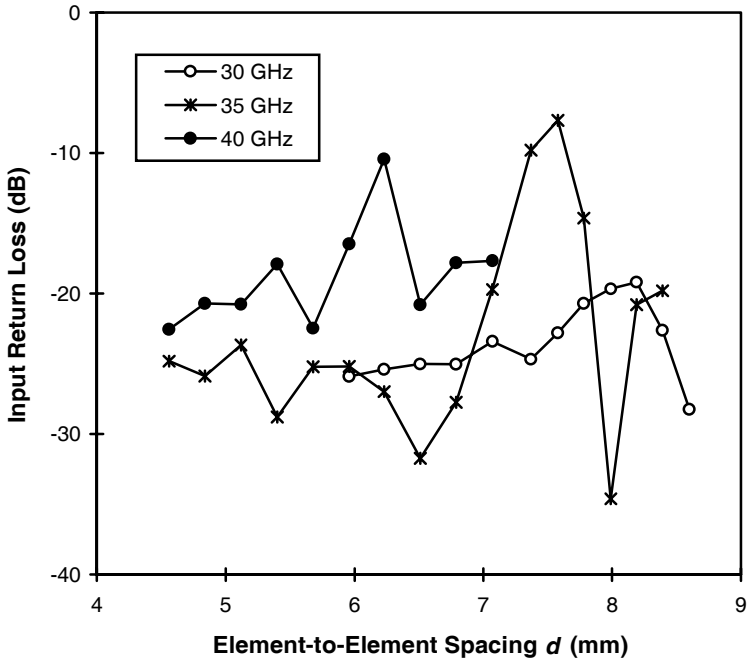

Fig. 13. Input return loss versus element-to-element spacing at 30, 35, and 40 GHz.

Figs. 14 and 15 illustrate the *E*- and *H*-plane co- and cross-polarization patterns at 35 GHz for d = 7.8 mm. As expected, the one-dimensional array-effect antenna produces a fan-shaped beam, directional in the *E*-plane but broad in the *H*-plane. Low-level ripples observable in the co- and cross-polarization patterns are attributable, in part, to edge diffraction from the finite ground plane and waveguide-to-image-line transition. Numeric calculation for the directivity indicates that the antenna efficiency for this radiation pattern is approximately 68%. The polarization of the main beam is highly linear, as indicated by the low cross-polarization levels near the scan angle. In order to gauge the variation in cross-polarization levels as the antenna scans, cross-polarization patterns are tested at 30, 35, and 40 GHz for d = 7.6 mm. This grating spacing is within the 30-GHz scanning range shown in Fig. 11 but outside the 40-GHz scanning range. Moreover, at 35 GHz, the beam scans to the broadside resonance when d = 7.6 mm. Even so, at this representative element-to-element spacing, cross-polarization levels at the scan angle are greater than 25 dB down from the main beam for 30, 35, and 40 GHz.

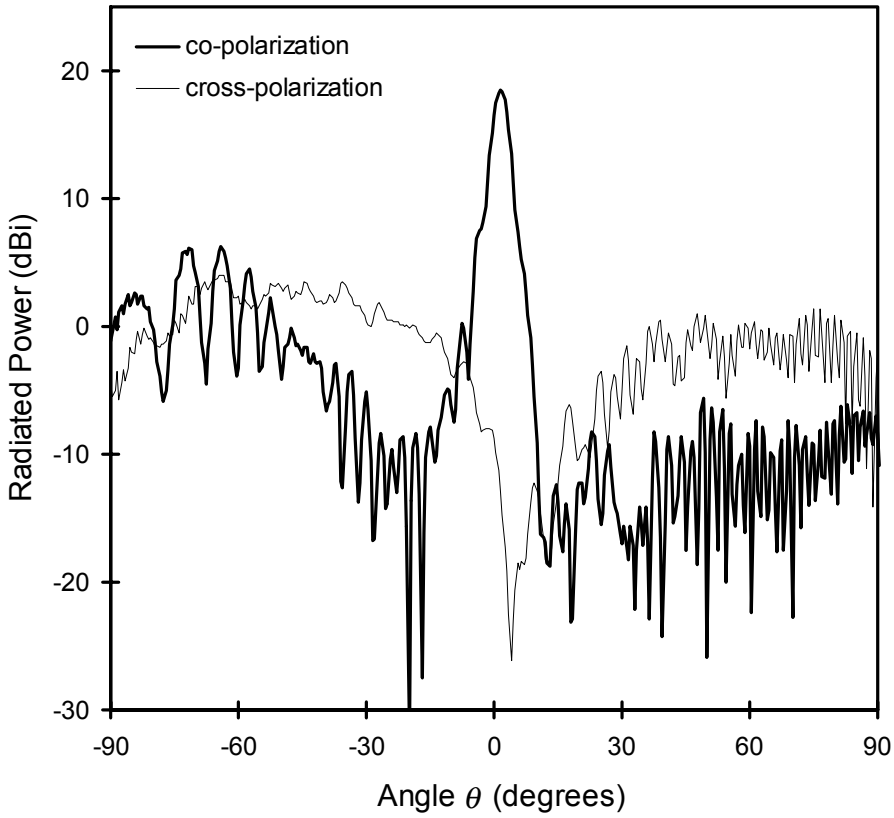

Fig. 14. *E*-plane co- and cross-polarization patterns at 35 GHz for $d = 7.8$ mm.

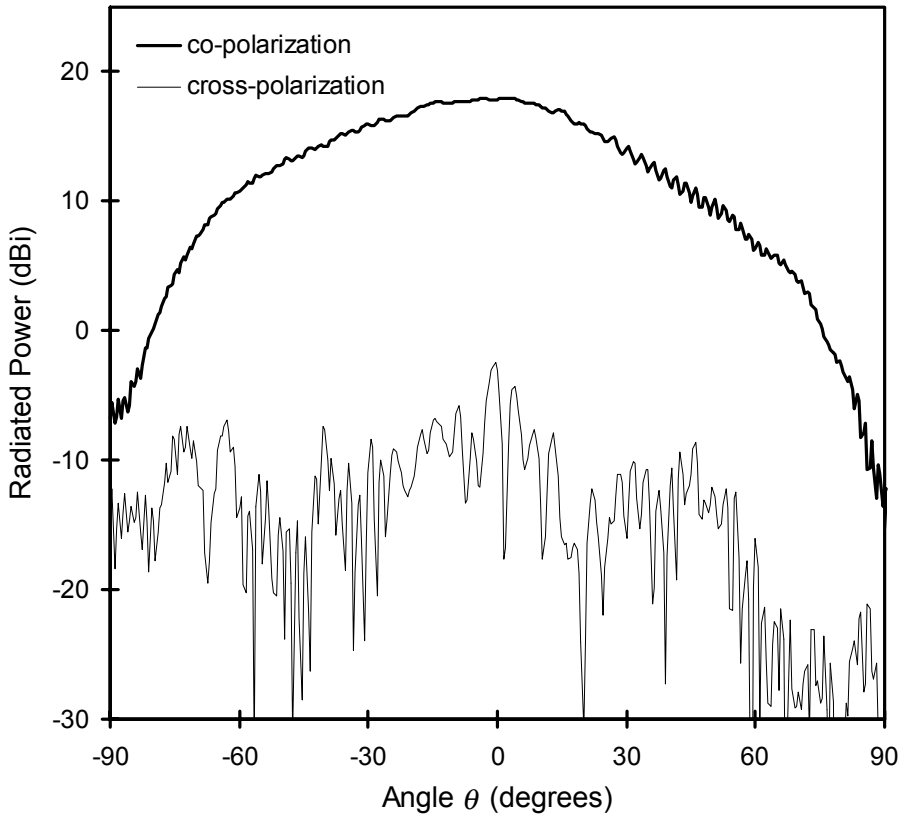

Fig. 15. *H*-plane co- and cross-polarization patterns at 35 GHz for d = 7.8 mm.

Figs. 16, 17, and 18 provide snapshots of selected *E*-plane radiation patterns as the beam scans at 30, 35, and 40 GHz, respectively. In the cases of the 35 and 40 GHz scans, scanning in the $+\theta$ direction is limited by the propagation of the n = -2 space harmonic, as predicted in (8). These plots illustrate in detail the key finding of this section – that an excellent radiation pattern is maintained over wide scan angles across the 30 to 40 GHz range.

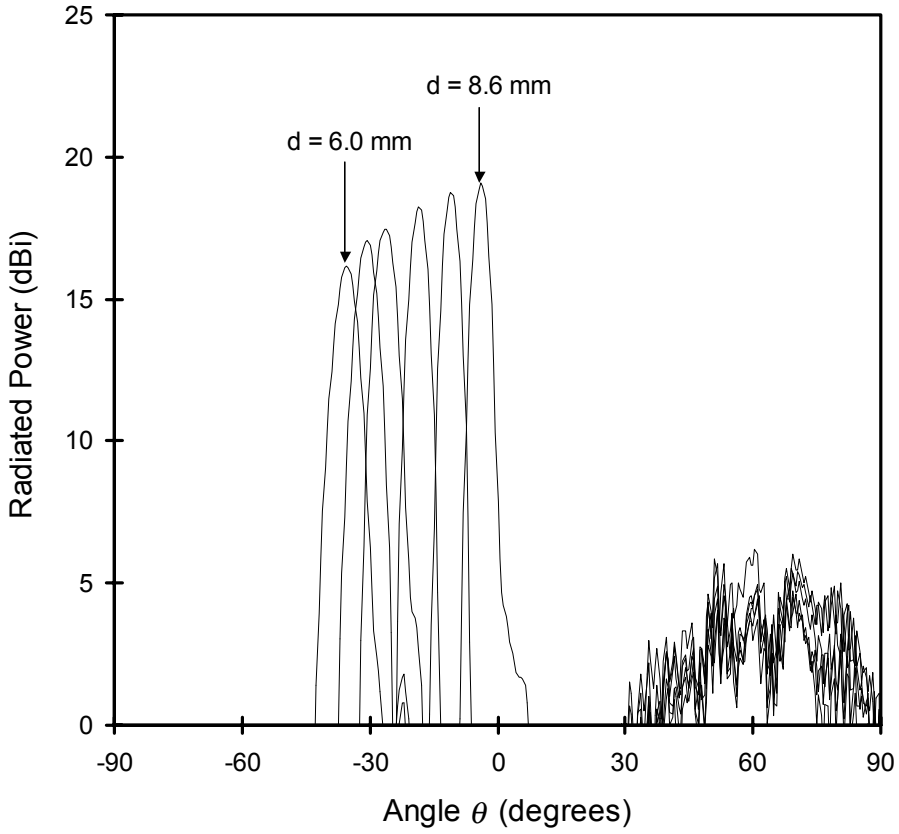

Fig. 16. *E*-plane radiation pattern as the beam scans at 30 GHz.

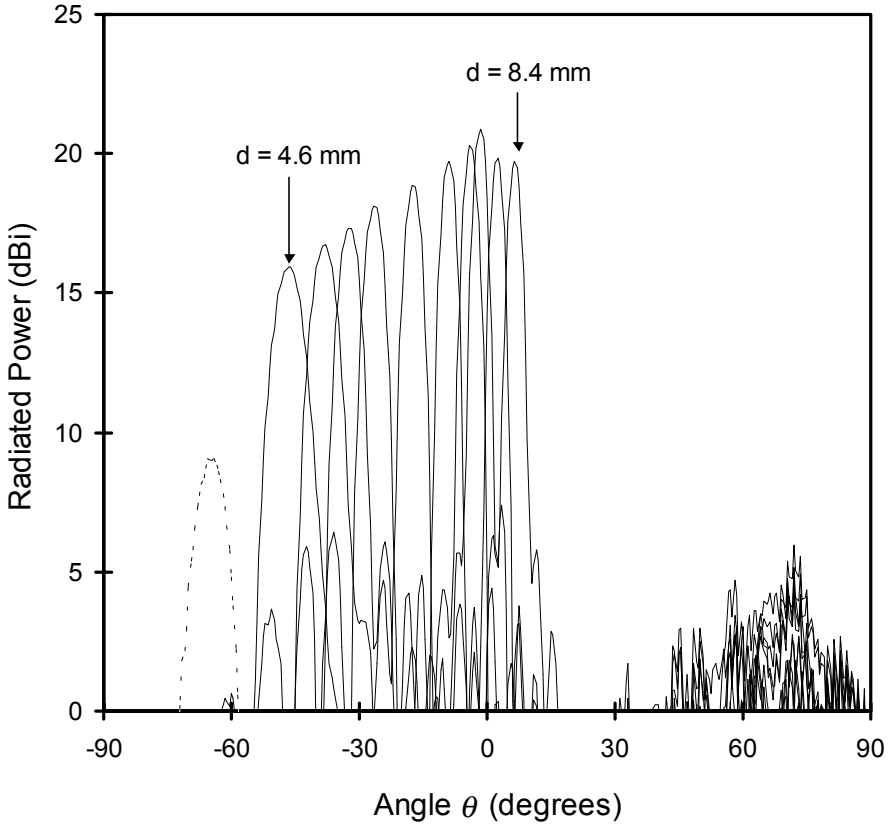

Fig. 17. *E*-plane radiation pattern as the beam scans at 35 GHz. The second space harmonic (dashed) is associated with the maximum forward scan.

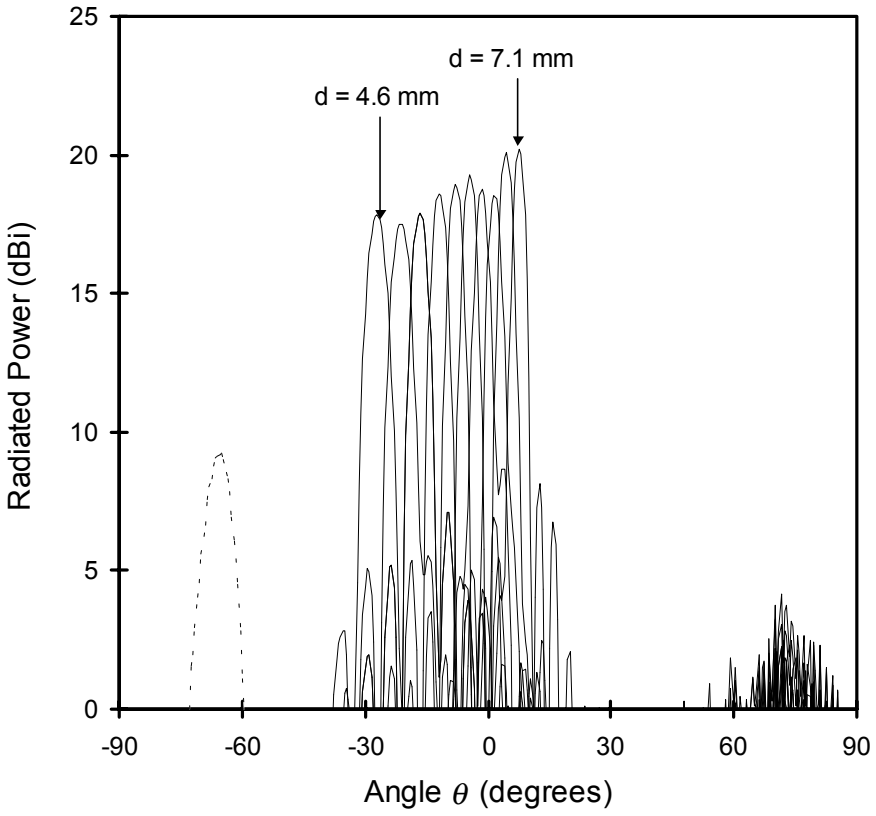

Fig. 18. *E*-plane radiation pattern as the beam scans at 40 GHz. The second space harmonic (dashed) is associated with the maximum forward scan.

E. Summary

This chapter has presented a novel leaky-wave antenna design in which a moveable grating film extended across a stationary dielectric image line allowed wide-angle, continuous beam scanning at 30, 35, and 40 GHz. The approach is broadband, low-cost, extremely simple in implementation, and shows an excellent radiation pattern across wide scanning ranges. Measured and calculated results for the main-beam scan angle

were in good agreement. The results should have many applications in broadband millimeter-wave beam-control techniques.

CHAPTER IV

A RECONFIGURABLE DUAL-BEAM GRATING ANTENNA FOR LOW-COST MILLIMETER-WAVE BEAM-STEERING*

This chapter presents a reconfigurable dual-beam grating antenna for low-cost millimeter-wave beam steering. Experimental results indicate that this multibeam approach provides over ±50° beam steering at fixed frequencies across the entire 35 to 40 GHz band, with excellent radiation patterns maintained across the scans. Measured beam scanning agrees well with design calculations. In addition, an approximate analysis developed for the reconfigurable antenna closely predicts the variation in the main beam radiation pattern across the complete range of scan states. These results should have numerous applications in millimeter-wave beam-steering technology.

A. Background

Over the past decade, the wireless telecommunications industry has established itself as one of the strongest growth areas in the world economy. In the US alone, the wireless telephony sector serves nearly 110 million customers, up from only 24 million in 1995 [70]. Although vigorous expansion is expected to continue in established wireless

---

applications, the next major growth areas in the wireless revolution have already begun to emerge. A variety of new applications are envisioned at the *Ka*-band and above in such areas as intelligent highway systems, autonomous landing systems, mobile satellite communications, intersatellite links, tracking and data relay, advanced security systems, and local multipoint distribution systems. Desirable capabilities for these systems often include the ability to exchange information between mobile terminals and a mother-station; the ability to acquire and track moving targets; and the ability to periodically reconfigure an antenna's aperture at will, without the need for human intervention.

Unfortunately, before many of these new millimeter-wave applications can penetrate the marketplace, significant advancements must take place in the development of low-cost technology for steering and redirecting millimeter-wave wireless signals. Conventional rotating gimbals are slow, unreliable and costly; yet they still remain representative of much of the beam-steering technology currently in use [71]. Phased-array systems, on the other hand, provide excellent speed and performance but require a wide range of state-of-the-art technology and supporting electronic equipment [72]. These systems are especially expensive, lossy, and complicated at millimeter-wave frequencies; they find use primarily in high-end military and space applications. To overcome these limitations, it is important to develop low-cost, mass-producible methods for beam control in the millimeter-wave region.

This chapter presents an especially simple and inexpensive approach for wide-scan millimeter-wave beam steering. The approach features a reconfigurable grating antenna designed for bidirectional excitation. Over ±50° scanning is achieved at fixed frequencies across the complete 35 to 40 GHz band, with excellent radiation patterns maintained across the entire range. The design itself is readily scalable to higher frequency bands and should have broad commercial applications in the emerging millimeter-wave wireless systems. Furthermore, the capability of the design to scan two beams simultaneously has direct applications in such areas as traffic management [73], [74], Janus sensors and dual-beam doppler radar [75]-[77], and wireless communications links [78]-[80].

A useful analytical procedure is also presented for calculating the radiation pattern of the reconfigurable antenna for varying distributions of grating strips. The analysis revises a classical spectral domain technique for gratings [69], significantly extending its range of applicability by eliminating the need to assume that the grating strips are narrow. In contrast to more rigorous procedures and numerical techniques, this approximate analysis is simple and particularly rapid, and yet it is still able to accurately predict the main beam characteristics of the radiation pattern across the complete ±50° range of scan states.

B. Concept and Design

Dual-beam antennas based on bidirectionally-excited printed-circuit leaky-wave antennas (LWAs) have recently gained interest [78], [79], [81], [82] due to their simple construction, wide scan range, and dual-beam capability. These designs use forward and backward traveling waves sharing the aperture of a single LWA to produce two beams, one forward from broadside and the other to the reverse of broadside. The dual radiated beams scan symmetrically with frequency or assymetrically using independent variable-frequency sources at each beamport [79]. Unfortunately, frequency scanning is inconvenient in many system applications. Also, the conductor loss of these dual-beam printed-circuit LWAs becomes an increasing obstacle at the high millimeter-wave frequencies where low-cost beam steering is especially required. As an alternative approach, this investigation presents a reconfigurable grating antenna designed for bidirectional excitation. The method of reconfigurability proposed in [83], [84] is applied to a new bidirectional grating design in order to achieve frequency-independent scanning of a dual-beam radiation pattern across wide angles both forward and reverse of broadside. Since the dual beams can be operated simultaneously or individually, this multibeam approach effectively doubles the scan range available using a single scanning beam [83] while providing the additional benefits of dual-beam capability that are especially useful for applications such as millimeter-wave consumer radar [73]. With the advantage of inherent low-loss operation at frequencies up to 120 GHz [23], this reconfigurable dual-beam antenna is well suited for the millimeter-wave wireless applications.

Fig. 19 illustrates the configuration of the proposed design. A thin, moveable dielectric film is extended across a stationary dielectric image line. Continuous metal grating strips are etched along the underside of the film, with the strips depicted as visible in the figure. Two opposing matched ports excite the image line, with the signal injected from port 1 radiating at an angle $+\theta$ and the signal injected from port 2 radiating at an angle $-\theta$. The signals may be injected simultaneously, allowing two independent traveling waves to share the aperture of the same grating. The spacing between grating strips varies linearly along the length of the film from d_{min} to d_{max}. Scrolling the film across the image line along the *y*-direction steers the dual beams along the angles θ in the *xz*-plane. The distribution of strip widths along the film is tapered away from each input port to gradually perturb either signal as it is launched along the image line. Although waveguide input ports are shown in the figure, it is noted that microstrip and CPW transitions to image line [66], [85] are also available.

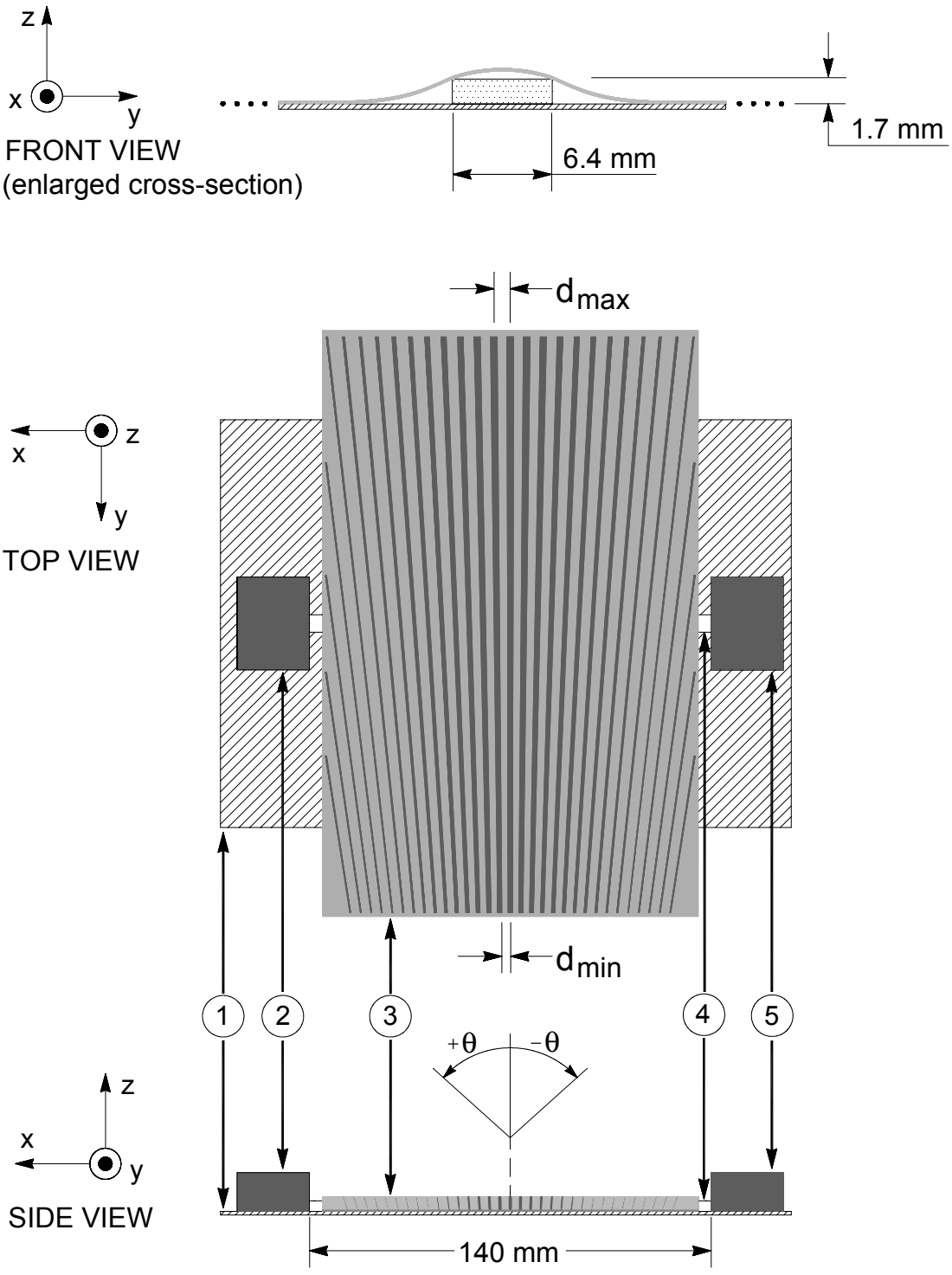

Fig. 19. Configuration of the dual-beam scanning grating antenna: 1) ground plane, 2) port 1, 3) grating film, 4) image line, 5) port 2.

The design of this antenna encompasses three key steps. The first step is to choose the aspect ratio and dielectric constant of the image line to ensure single-mode propagation over the antenna's desired frequency range. Once this is done, the dispersion of the guided wavelength across that frequency range can easily be calculated using the effective dielectric constant (EDC) technique of Knox and Toulios [64]. The accuracy of this EDC technique has been clearly demonstrated [64] for an image line whose aspect ratio is sufficiently wide and whose relative dielectric constant is sufficiently low. For designs using narrow image guides or high dielectric constant materials, full-wave simulation or rigorous methods [23] should be used. The image line used in this investigation is 1.58 mm high, 6.4 mm wide, and 139 mm long and is fabricated from RT-Duroid 5880 ($\varepsilon_r = 2.2$). This geometry and relative dielectric constant ensures single-mode propagation across the 35 to 40 GHz band.

The second step in the design is to choose the maximum and minimum spacing d between grating elements in order to steer both beams across a specified range of angles θ for the antenna's desired frequency range. Assuming the grating strips themselves have a negligible effect on the propagation constant along the perturbed guide, the angle of radiation in the direction forward from broadside can be calculated at any given frequency of excitation as a simple function of the guide wavelength λ_g and strip spacing d using Equation (8) from Chapter III. Typically, the space harmonic n (0, ±1, ±2, ···) is chosen as –1. In principle, the potential scanning range of θ_{-1} extends both

forward and reverse of broadside, across the entire ±90° range. It is difficult, however, to achieve a sufficiently high effective relative dielectric constant along an image line or other open dielectric guide in order to prohibit appearance of the $n = -2$ grating lobe for increasingly positive values of θ_{-1} while still maintaining single-mode bandwidth along the guide. Unusually high dielectric constants ($\varepsilon_r > 20$) are required, with associated tradeoffs in performance and implementation [86], [87]. Although scanning for $\theta_{-1} > 0°$ is thus typically limited by the propagation of the $n = -2$ space harmonic, the overlap between the scan ranges of the dual radiating beams should be useful for handover from one beam to the other, a feature not allowed with printed circuit dual-beam LWAs.

The maximum and minimum grating spacings used in this investigation are chosen as d_{max} = 7.14 mm and d_{min} = 3.69 mm, in order to ensure that each of the dual beams can scan at least $50°$ away from broadside for the entire 35 to 40 GHz band. The moveable film is fabricated from 0.13-mm-thick RT-Duriod 5880, measuring 139 mm in width along the *x*-direction of Fig. 19. For photolithography purposes, two sections of film are used. The first section is 258 mm long in the *y*-direction, with the spacing between strips varying from d_{max} = 6.36 mm to d_{min} = 3.69 mm along the film's length. The second section is 42.4 mm long, with the spacing varying along its length from d_{max} = 7.14 mm to d_{min} = 6.23 mm.

The third and final design step involves determining the bidirectional distribution of strip widths along the surface of the moveable dielectric film. To allow convenient

measurement up to 40 GHz in an indoor far-field antenna range, the length of the entire structure shown in Fig. 19 is limited to 19 cm, correspondingly limiting the length of the grating aperture to 14 cm. As in the case of a unidirectionally-tapered single-beam grating antenna [29], using narrower strips near the input to the guide provides a more optimal transition between the guided wave and the radiating wave, significantly reducing the observed side-lobe level. For the bidirectionally-tapered design of Fig. 19, wider strips are used near the center and narrower strips near the edges in order to provide for the gradual perturbation of both signals as they are launched along the image line. The variation in strip widths is determined at the inter-element spacing required to achieve broadside scan at the 40 GHz upper frequency limit. The widths of the strips are designed at that element-to-element spacing to vary linearly from 0.125 wavelengths at the edges to 0.4 wavelengths in the center. The width of each continuous grating strip is scaled along the length of the film to increase or decrease linearly as the spacing between strips increases or decreases. Furthermore, as the spacing between strips decreases, additional grating strips are added at the edges of the film in order to use the radiating aperture as efficiently as possible.

C. Analysis

The ability to predict how the radiation pattern varies across the scan range is especially critical for systems in which the beam steers across a wide range of angles. This section presents a simple and effective analytical procedure capable of accurately predicting the variation in the main beam radiation pattern across the entire scan range of the

reconfigurable design discussed in this chapter. The analytical procedure calculates the complex propagation constant along the interface between the grating film and dielectric image line and uses that information to reconstruct the far-field radiation pattern of the antenna for varying grating spacings and varying distributions of strip widths.

The complex propagation constant along the surface of the grating contains two parts, an imaginary part α referred to as the *leakage constant* and a real part β referred to as the *phase constant*. α determines the rate of radiation along the grating and the beamwidth in the far field. β determines the direction of the main beam. A rigorous solution for the phase constant is typically unnecessary since β can be approximated with good accuracy as $k_o \sin(\theta_{-1})$, with θ_{-1} given from the expression in Equation (8) of Chapter III. Calculating the leakage constant α, however, is typically considered an involved process, even for gratings that use a uniform distribution of strip widths [20]. For the dielectric strip gratings commonly used in integrated optics, both commercial software and curve-fit models [88] are available. For metallic strip gratings, several rapid analytical procedures are available for the limiting cases of narrow strip gratings and narrow slot gratings [16], [69], [89]. Typical designs, however, use strips whose widths fall between the two limiting cases. For such designs, more rigorous numerous numerical methods are available, with varying levels of rigor and computational effort for each approach. These methods include mode-matching techniques [3], [68], waveguide models [90], rigorous network formulations [67], and full-wave simulation [91], [92].

The approach taken in this analysis is to revise and extend the elegant spectral domain technique formulated in [69]. This revised analysis eliminates the restriction of the technique to narrow strip widths. In addition, it accelerates [69] from a three-dimensional calculation to a two-dimensional calculation; assumes a different mode of excitation; reformulates the spectral domain Green's function to account for the presence of a ground plane and a dielectric overcoat (for the grating film); and uses an approximation to address the bidirectionally tapered distribution of strip widths.

The method used in the original formulation of [69] simultaneously solves for both the real and imaginary parts of the grating's complex propagation constant. To gain computational economy, it is noted that the leakage constant α can be accurately approximated as the imaginary part of the complex propagation constant along a grating of infinite width [22]. The phase constant β along the true finite-width grating can be evaluated outside the spectral-domain calculation using the common but accurate approximation discussed above. This strategy simplifies the required spectral domain calculation from a three-dimensional problem to a two-dimensional problem. Fig. 20 illustrates the equivalent two-dimensional geometry for the design used in this chapter. t_1 and t_2 represent the thicknesses of the image line and grating film, respectively. The grating film used in this investigation is sufficiently thin and flexible such that any air gap between the film and image line is negligibly small. In the presence of an air gap, however, the rate of radiation along the guide should necessarily decrease, especially for

high frequencies of operation or with high dielectric constant materials. In such a case, the effect of the air gap can also be modeled using this same analysis by straightforward modification to the spectral domain Green's function for this structure. The metal grating strips themselves are assumed to be infinitesimally thin and of uniform width.

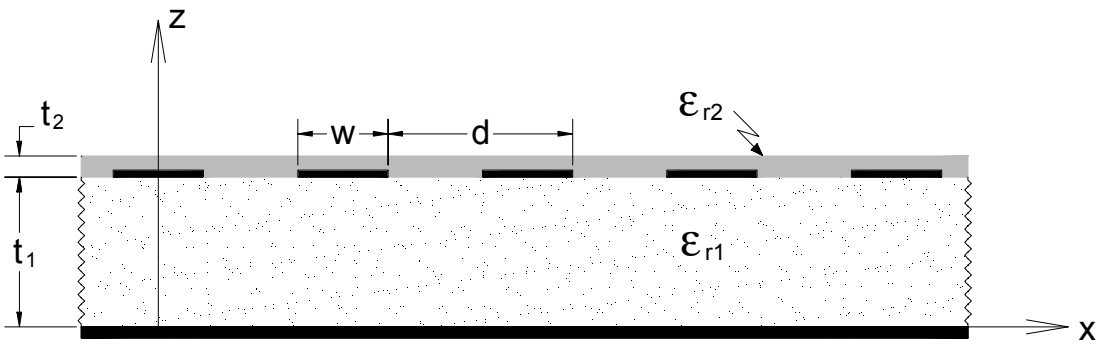

Fig. 20. Two-dimensional model for a grating antenna with a dielectric overcoat.

The polarization of the far-field radiation is determined by the field distribution along the dielectric guide, which in turn depends on the method of excitation. Referring to the coordinate system of Fig. 19, the primary field components under *E*-wave excitation are H_y, E_x, and E_z, and the antenna's *E*-plane is located in the *xz*-plane. Under *H*-wave excitation, the primary field components are E_y, H_x, and H_z, and the *H*-plane is located in the *xz*-plane. The configuration used in this chapter uses *E*-wave excitation. *E*-wave excitation can be modeled in the plane of the grating interface via the spectral domain Green's function for an infinite line source of current density $\boldsymbol{J}_{\boldsymbol{LS}} = J_o\,\delta(x)\,\delta(z-t_1)\,\boldsymbol{u}_{\boldsymbol{x}}$ [93]. The appropriate Green's function for the boundary conditions given in Fig. 20 can

be derived directly in the spectral domain using the spectral domain immittance method [94]. The resulting expression is given as

$$\widetilde{G}_{xx} = -\frac{\eta_0}{k_0}\frac{k_{z1}k_{z2}A}{\varepsilon_{r2}k_{z1}B - j\varepsilon_{r1}k_{z2}A\cot\left(k_{z1}t_1\right)} \tag{11a}$$

with

$$A = k_{z2} - j\varepsilon_{r2}k_{z3}\cot\left(k_{z2}t_2\right) \tag{11b}$$

$$B = \varepsilon_{r2}k_{z3} - jk_{z2}\cot\left(k_{z2}t_2\right) \tag{11c}$$

and

$$k_{z1} = \sqrt{\varepsilon_{r1}k_o^2 - k_x^2} \tag{11d}$$

$$k_{z2} = \sqrt{\varepsilon_{r2}k_o^2 - k_x^2} \tag{11e}$$

$$k_{z3} = \sqrt{k_o^2 - k_x^2} \tag{11f}$$

where η_o is the impedance of free space, k_o is the free-space wavenumber, and k_x is the unknown complex-valued propagation constant. The branch choices for the roots in (11d)-(11f) must be chosen so that the real parts are positive and the imaginary parts are negative.

For *E*-wave excitation, the current distribution along each strip is accurately described using an analytic approximation [95], mitigating the need for a computationally intensive spectral-domain moment method solution [90] or for the limiting assumption of constant current along each strip [69]. In the spectral domain, the current distribution along a strip centered at $x = 0$ may be written, to within a constant, as

$$\tilde{\boldsymbol{J}} = \boldsymbol{u}_x \tilde{J}_x = \boldsymbol{u}_x \int_0^{w/2} \cos(k_x x) \sqrt{1 - \left(\frac{2x}{w}\right)^2}\, dx \tag{12}$$

The integral in the above equation reduces to

$$\tilde{J}_x = \frac{\pi}{2k_x} \cdot J_1\left(\frac{w k_x}{2}\right) \tag{13}$$

where $J_1(\xi)$ signifies a Bessel function of the first kind of order 1 evaluated for some argument ξ. An equivalent expression can likewise be derived for the current distribution under *H*-wave excitation by transformation of the result in [96].

The appropriate eigenvalue equation for the two-dimensional metal-strip grating is obtained by simplification of the result found in [69]:

$$\sum_{n=-\infty}^{+\infty}\left\{\tilde{G}_{xx}\left(k_x\right)\cdot\tilde{J}_x^2\left(k_x\right)\right\}\Big|_{k_x=\beta+j\alpha+\frac{2\pi n}{d}}=0 \tag{14}$$

This equation is solved in the complex plane for α and β by truncating the infinite summation to a finite number of Floquet modes. The calculated value for β along the two-dimensional structure is subsequently discarded in favor of the common approximation discussed earlier. The results presented in this chapter use $|n|=30$, after which the calculated values for both α and β are well converged for the range of strip widths and spacings considered.

The design illustrated in Fig. 19 uses continuous metal grating strips. The widths of the strips vary in a bidirectional taper along the *x*-direction while the spacings between strips vary linearly along the *y*-direction. For a fixed value of *d*, the leakage constant α is calculated for each strip width *w*. Repetitive solution of Equation (14) for successive values of w and fixed values of d is especially straightforward since the calculated value for β varies only slightly for a specified grating spacing *d*. The leakage constant along the variable-width grating is then approximated as a continuously varying function $\alpha(x)$ sampled at each strip location along the grating.

The dual-beam radiation pattern in the far field can be found using the spatial Fourier transform of the calculated near-field distribution. For example, in the case of equal

phase excitation at both ports, the far-field radiation pattern in the *E*-plane (*xz*-plane) of Fig. 19 may be expressed, to within a constant, as

$$R(\theta) = \int_0^L \cos\left[k_o x \sin(\theta)\right] \cdot e^{-(\alpha(z) + jk_o \sin(\theta_{-1}))x}\, dx \tag{15}$$

where L is the total length of the grating along x and θ_{-1} is the angle given in Equation (8). In [22], the authors suggest that a $\sin(\pi x/L)$ weighting function be applied to the near-field distribution in order to more accurately model the aperture distribution near the input port and termination of the antenna. In the present case, using this weighting function is found to greatly increase the accuracy of the calculation at the extreme scanning limit of the reconfigurable grating where the beam broadens considerably. Including this term within the integrand of Equation (15) results in only a small loss of accuracy at the other scan angles. Comparisons between measurement and theory are presented in the following section, with excellent agreement demonstrated across the entire range of measurement.

D. Experimental Results

Fig. 21 illustrates the variation in the main beam scan angle as the element-to-element spacing of the reconfigurable grating is varied along the surface of the bidirectionally-excited dielectric image line. The test setup uses a *Ka*-band magic tee to combine received CW power from the two beamports. The signal amplitudes are equalized at

both ports, with arbitrary phase excitation to each port. Experimental results agree well with the designed values obtained using Equation (8) together with the calculated dispersion of the guided wavelength along the image line. Over the entire range shown in Fig. 21, maximum sidelobe levels are greater than 10 dB below the main beam for both beams, and input return loss is less than −15 dB at both ports. Using these conservative criteria to define the scan range, over ±52° scanning is reported at 35 GHz and over ±51° scanning at 40 GHz. For the purposes of handover between the beams, either beam may be steered to about 5° in the reverse of broadside [83]. Scanning within ±5° of broadside, however, is not illustrated in this figure since the characteristics of the dual-beam radiation pattern near broadside are dependent on the relative phase between the signals injected at each beamport. In practice, if two beams operate simultaneously at the same frequency, either a sum or difference pattern may be obtained at broadside, depending on the relative phase.

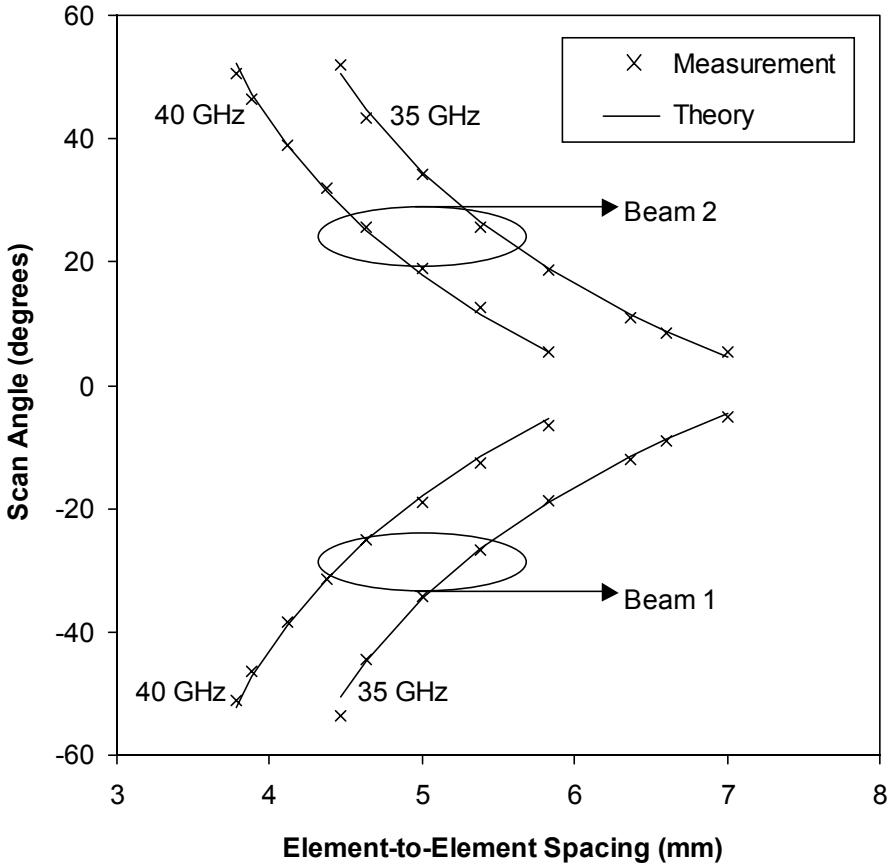

Fig. 21. Measured and calculated scanning angles for both beams.

An important consideration in many system applications is the maximum bandwidth available at a given scan angle. In the case of leaky-wave radiators such as the grating antenna, the overall system bandwidth is limited by the dispersion in the main beam angle with frequency rather than by the impedance matching to the antenna. To characterize this effect for the design presented in this chapter, the antenna's *instantaneous bandwidth* can be defined as the range of frequencies surrounding the nominal operating frequency across which the main beam angle remains within the

original half-power beamwidth [97]. This parameter can be accurately approximated using the information included in Fig. 21 together with the measured beamwidth at each scan state. Across the 35 GHz scan, the instantaneous bandwidth varies from 877 to 1888 MHz. Similarly, across the 40 GHz scan, the instantaneous bandwidth varies from 1301 to 1796 MHz. In both cases, minimum bandwidth occurs at the maximum scan angle. Although the instantaneous bandwidth using this scanning antenna is only on the order of a few percent, the design is suitable for numerous radar and tracking applications as well as for moderate data-rate wireless communications. In addition, the very broad overall bandwidth seen in this design provides potential system-level advantages. For example, the results presented in Fig. 21 indicate that, for the case of simultaneous dual-beam operation, using frequency scanning in conjunction with reconfigurability allows the opportunity for independent control of both beams.

Figs. 22 and 23 illustrate the variation in the *E*-plane (*xz*-plane) radiation pattern at 35 and 40 GHz as the dual beams simultaneously steer away from broadside with decreasing grating spacings. A highly directive dual-beam radiation pattern is maintained over the entire range of scan states, with low side lobes and excellent symmetry between the beams. The gain does not monotonically decrease as the beam steers away from broadside due to the fact that additional grating strips are added into overall grating film as the spacing between strips narrows in order to counteract the rolloff in gain with increasing scan angle. Isotropic gains of 18.37 ± 0.75 dB and 18.29 ± 1.12 dB are observed across the 35 and 40 GHz scans, respectively. Across the same

range of scan states, transmission from port 1 and port 2 increases from –15.2 dB to –11.0 dB at 35 GHz and from –12.2 dB to –9.2 dB at 40 GHz. The rms gain imbalance between beams is 0.14 dB at 35 GHz and 0.22 dB at 40 GHz. Likewise, the rms asymmetry between beam pointing angles is 0.85° at 35 GHz and 0.50° at 40 GHz. The maximum cross-polarization level at a specific scan state varies from 15.3 to 32.7 dB down (from the co-polarization) at 35 GHz and from 14.2 to 23.9 dB down at 40 GHz. These relatively low cross-polarization levels nonetheless represent a decrease in cross-polarization suppression of about 10 to 15 dB in comparison with a conventional unidirectional grating antenna. This increase is attributed to the opposing slopes used for the continuous grating strips in the bidirectional design of Fig. 19. Nonetheless, if additional cross-polarization suppression is required and continuous scanning is not, discrete sets of grating strips can be etched onto a single grating film, with each set of strips having a specific spacing between grating elements. Not only would such an arrangement further increase the cross-polarization suppression, but it would also allow the overall film size to be reduced if only a limited number of scan states is required.

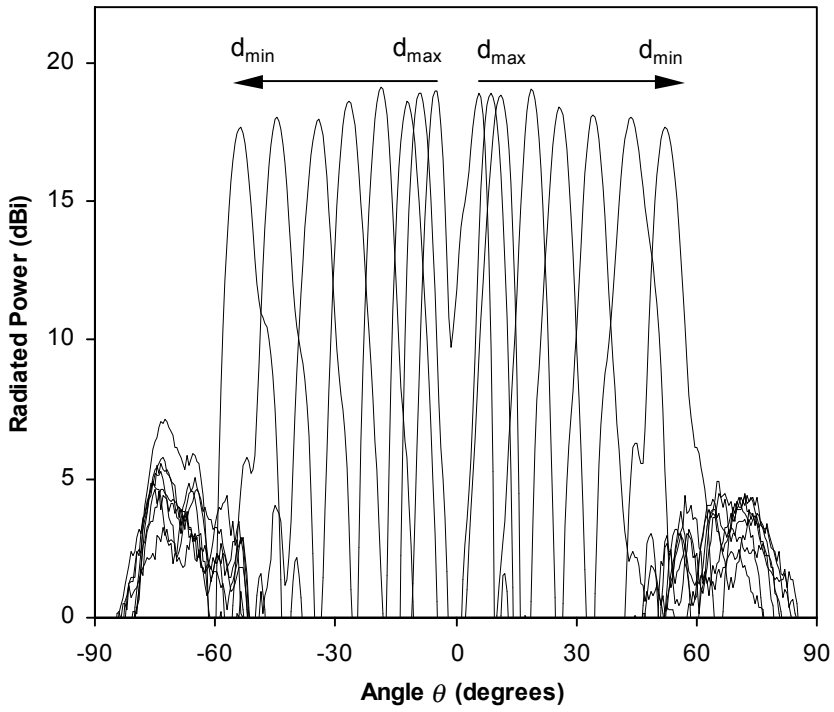

Fig. 22. Beam steering for the dual-beam radiation pattern at 35 GHz.

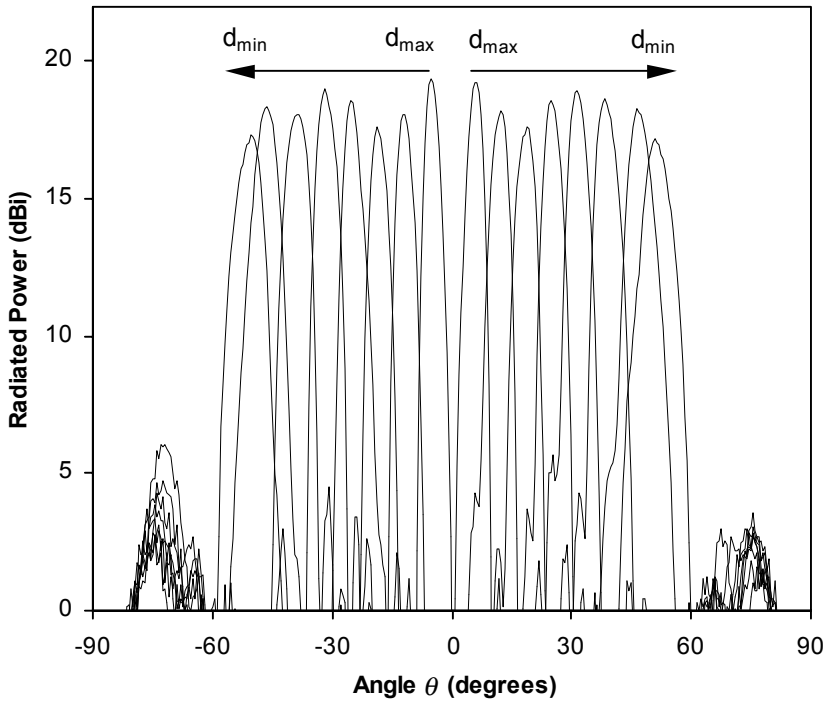

Fig. 23. Beam steering for the dual-beam radiation pattern at 40 GHz.

Measured results indicate that this millimeter-wave beam-steering approach provides fixed-frequency beam-steering across a wide range of scan angles and broad range of frequencies, with an excellent radiation pattern maintained across the scans. The variation in the antenna's aperture efficiency across the measured scanning ranges can be evaluated by comparing the physical area of the grating's radiating aperture to the area of a uniformly illuminated aperture capable of producing the same principle-plane beamwidths. Using this approach, the efficiency of the grating decreases, as the dual beams steer away from broadside, from 85 percent to 57 percent at 35 GHz and from 62 percent to 32 percent at 40 GHz. To increase the efficiency, the image line can be

embedded in a flared trough [29] to narrow the very broad *H*-plane beamwidth. In addition, a more elaborate transition [98] may be used to increase the efficiency by decreasing the spurious radiation from the image line feed that dominates the sidelobe pattern for $60° < |\theta| < 90°$.

Figs. 24 and 25 provide a comparison between measured and calculated radiation patterns for representative scan states at both 35 and 40 GHz, respectively. The calculated patterns are obtained by the analysis discussed in this chapter. In order to eliminate the angle errors already illustrated in Fig. 21, the calculations use measured values for the Beam 1 scan angle from Fig. 21 in Equation (15) rather than calculated values of θ_{-1} from Equation (8). Excellent agreement between measured and calculated main beam radiation patterns is demonstrated across the entire range of measurement. The side-lobe levels for this class of antenna, however, are in practice dominated by spurious radiation from the image-line feed [69].

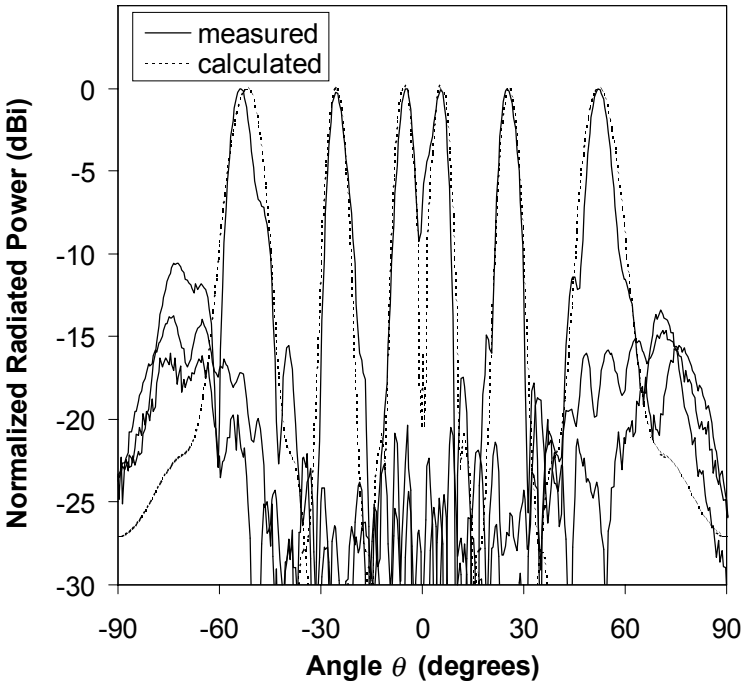

Fig. 24. Measurement vs. theory at 35 GHz illustrated for three representative scan states.

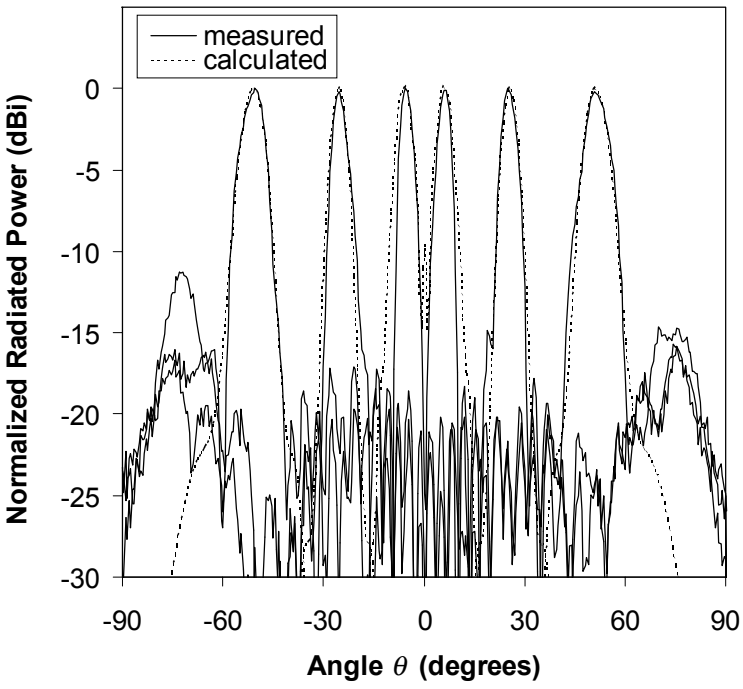

Fig. 25. Measurement vs. theory at 40 GHz illustrated for three representative scan states.

Finally, it is noted that one limitation in the use of grating antennas has been the difficulty in synthesizing a beam pointed directly at broadside due to the bandstop resonance of the grating [9]. An attractive feature of the new bidirectional design is the capability to create a broadside beam by allowing two equiphase beams to approach but not reach broadside. The two beams combine to form a single broadside beam before the bandstop resonance occurs. To demonstrate this feature, a broadside sum pattern generated using two beams of approximately equal phase is shown at 35 GHz in Fig. 26.

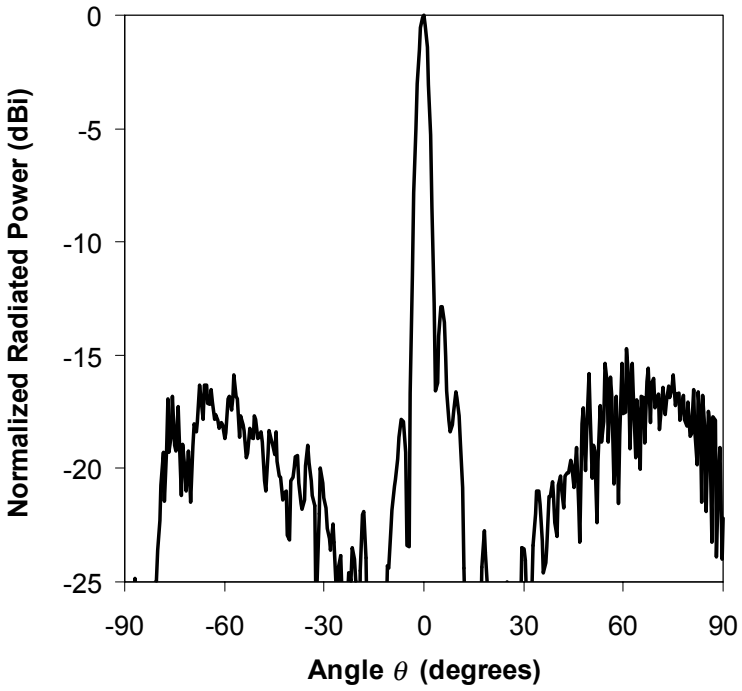

Fig. 26. Broadside radiation pattern generated at 35 GHz.

E. Summary

A vast array of consumer applications is envisioned at millimeter-wave frequencies in areas ranging from mobile communications to intelligent transportation. Unfortunately, current technology for steering and redirecting millimeter-wave wireless signals is prohibitively expensive for many of the anticipated applications. State-of-the-art millimeter-wave phased array systems require advanced integration procedures, sophisticated RF technologies, and considerable supporting electronic equipment. Similarly, rotating antennas become undesirable at these frequencies due to the costly gimbals and delicate manufacturing required. To provide an alternative, low-cost approach for millimeter-wave beam steering, this chapter has introduced a

reconfigurable dual-beam grating antenna. Based on the millimeter-wave beam steering technique introduced in the previous chapter, this dual-beam approach effectively doubles the scan range available using a single scanning beam, giving the device the ability to track a target or user across a wide range of angles both forward and reverse of broadside. In addition, the capability to produce simultaneous dual beams, if desired, offers further practical advantages, including, in the case of radar and navigation systems, abilities such as soft degradation of performance with frequency drift, level correction, averaging, etc., [73], [74].

The reconfigurable dual-beam antenna presented in this chapter provides over ±50° beam steering at fixed frequencies across the entire 35 to 40 GHz band, with excellent radiation patterns maintained across the scans. An approximate analytical procedure developed for the reconfigurable design closely predicts the observed scan angles and main beam radiation patterns across the complete range of scan states. The approach itself readily scales to higher frequency bands and should have numerous practical applications in millimeter-wave beam-steering technology.

CHAPTER V

CIRCULAR-POLARIZED RECONFIGURABLE GRATING ANTENNA FOR LOW-COST MILLIMETER-WAVE BEAM-STEERING*

This chapter presents a circular-polarized (CP) reconfigurable grating antenna for low-cost millimeter-wave beam steering. A CP grating array is introduced. Using an inertialess mechanical movement, the grating design can be reconfigured along the surface of a dielectric image line, allowing a directive CP beam to steer across a wide range of angles. Over 43° of beam steering is achieved at 32.5 GHz with axial ratio less than 1 dB across the entire scan range. Measured performance agrees well with theory. These results are inherently scalable to higher millimeter-wave frequencies and should have numerous uses in emerging millimeter-wave satellite communications applications and other related systems for mobile communications and radar.

A. Background

Circular-polarized phased arrays and scanning antennas play an increasingly important role in satellite communication systems, finding use not only aboard satellites

---

 Parts of this chapter are reprinted, with permission, from C.T. Rodenbeck, M. Li, and K. Chang, "Circular-polarized reconfigurable grating antenna for low-cost millimeter-wave beam-steering," to appear in *IEEE Trans. Antennas Propagat*.

themselves but also in mobile earth stations and related ground-based systems for satellite monitoring and tracking. Unfortunately, the deployment of phased arrays in this market is constrained by limitations of cost, size, power and performance [72]. Such limitations become especially critical at the *Ka*-band frequencies allocated to next-generation satellite systems [71]. Likewise, conventional rotating antennas face limitations of cost and reliability that escalate dramatically in the millimeter-wave region.

Recent research has demonstrated a new low-cost approach for millimeter-wave beam steering based on a reconfigurable grating antenna fed by dielectric image line [38]. This approach is particularly inexpensive and yet is capable of providing fixed-frequency beam steering across a wide range of angles. To extend the technique and broaden its commercial applications, this chapter presents a CP grating antenna that can be reconfigured to achieve low-cost CP beam steering at millimeter wavelengths.

Fig. 27 illustrates the configuration of the reconfigurable CP antenna. A thin, movable dielectric film is extended across the surface of a dielectric image line. Multiple linear arrays of metal grating strips are etched along the underside of the film. These arrays of strips are depicted as being visible in the figure. The spacing and rotation of the strips within each array are determined in order to create a CP beam at a preferred angle θ when that array is positioned above the dielectric image line. Scrolling the film in the *y*-

direction along the surface of the image line scans the CP beam from one angle θ to another.

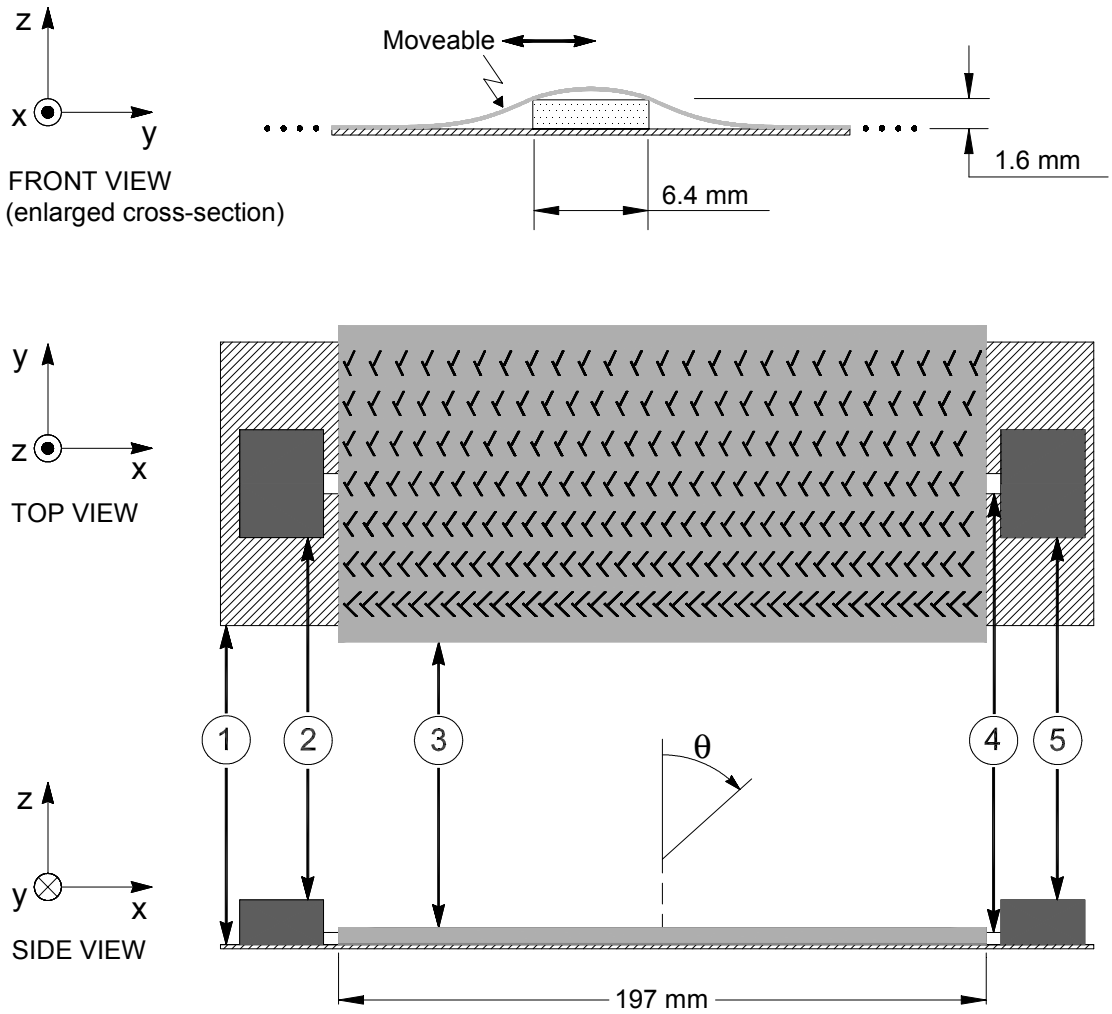

Fig. 27. The CP reconfigurable grating antenna: 1) ground plane, 2) port 1, 3) grating film, 4) image line, 5) matched load.

Unlike other millimeter-wave phased arrays, this approach is inexpensive due to the low loss and easy fabrication of dielectric integrated guides for applications at 30 GHz and

above. Unlike conventional mechanically rotating antennas, this design uses a mechanical motion that is inertialess and completely external to the millimeter-wave feed. The movement of the film can be implemented using a simple dc motor, and the construction of the image line is compatible with mass-production [10], [57].

Experimental results presented in this chapter demonstrate over 43° beam steering at 32.5 GHz with axial ratio less than 1 dB over the entire scan range. The reconfigurable CP grating antenna is simple, inexpensive, and readily scalable to frequencies up through the *W*-band and beyond. The design should have many commercial and military applications in emerging millimeter-wave mobile communication and radar systems.

B. Design

A conventional grating antenna is constructed by placing a periodic array of transverse strips along the surface of a dielectric waveguide, such as a dielectric image line. These strips perturb the signal propagating along the guide, exciting one or more leaky modes above the surface to produce a fan-shaped beam of radiation in the far field. Although the far-field pattern is typically highly linear-polarized (LP) at the main beam angle, the cross-polarization at the main beam angle increases significantly if the strips are not parallel with one another. This effect can be exploited to create a CP grating antenna.

Fig. 28 shows the configuration of the proposed CP grating antenna. Two sets of grating strips are placed along the surface of an image line in a “fishbone” pattern similar to the

arrangement used in CP slot arrays fed by image line [99], microstrip line [100], coaxial line [101], and radial cavities [102]. Unlike the image-line-fed slot array, the proposed CP grating array radiates unidirectionally, can be easily fabricated using conventional photolithography, and is adaptable to the reconfiguration technique of [38].

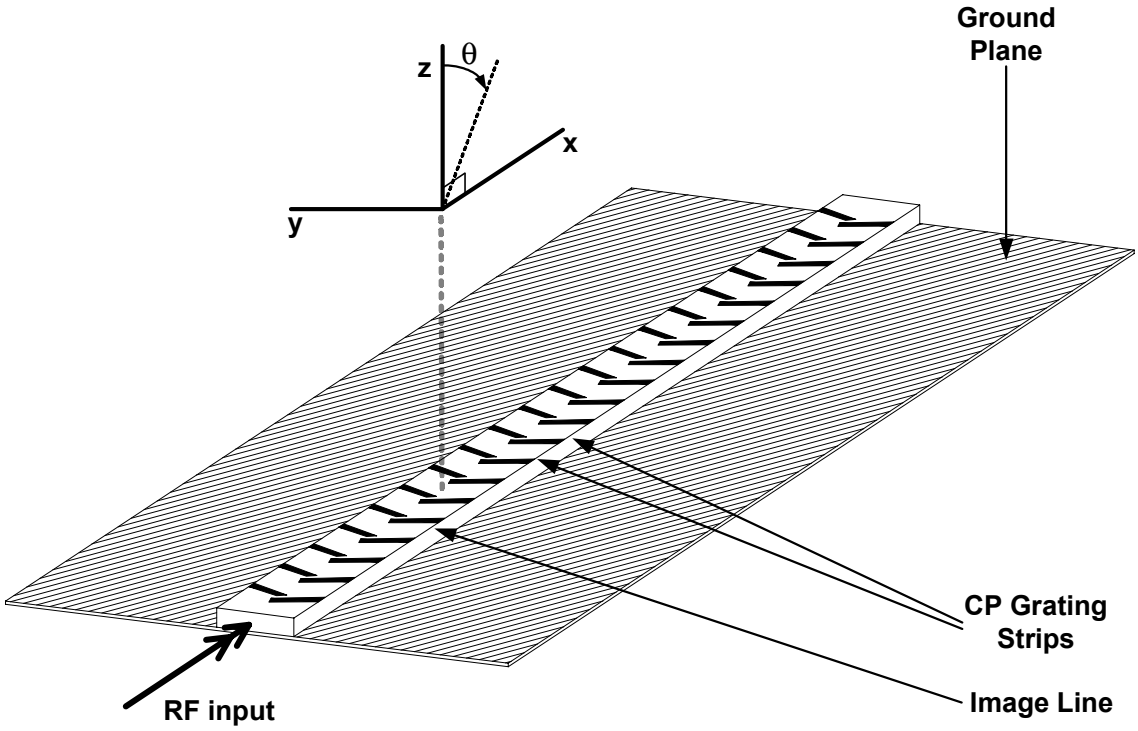

Fig. 28. Circular-polarized grating antenna.

The spacing and rotation of the strips are determined in order to create a CP beam at a preferred angle θ with respect to broadside. A magnified view of the metal strip pattern along the image line is illustrated in Fig. 29 for two unit cells of the CP grating array. The design parameters include the grating spacing d_1, the offset spacing d_2, the strip rotation angle α, the strip width w_s, the strip length l_s, and the offset distance δ of each strip from the centerline. The angle of radiation θ is determined by the spacing d_1 between unit cells and by the guide wavelength λ_g according to the relationship given in Equation (8) in Chapter III. As in the previous two chapters, the space harmonic *n* (0, ±1, ±2, ···) is chosen as –1. For dielectric image lines whose aspect ratio is wide and whose dielectric constant is low, λ_g can be accurately calculated using the technique of [64]. For high-dielectric constant materials, full-wave 3-D electromagnetic simulation should be used.

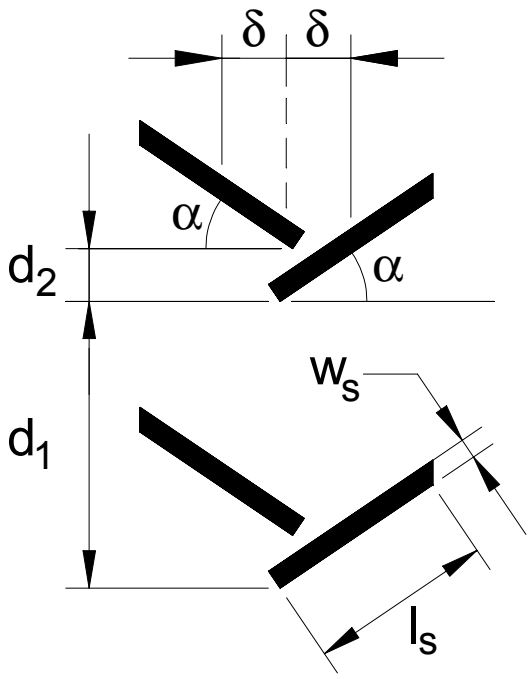

Fig. 29. Two unit cells of the CP grating array.

The three key parameters controlling the main beam polarization are d_1, d_2, and α. By considering the radiation pattern produced by a single unit cell of the grating array, it is possible to determine what values to choose for these parameters so that circular polarization is produced at the scan angle θ_{-1}. The mode of excitation used in this investigation is such that the primary field components along the image line are H_y, E_x, and E_z. In this case, the surface of the grating can be modeled as a sheet of x-directed current with a complex propagation constant [22]. This surface-current model can be reduced to a single unit cell (*i*) by conceptually replacing area covered by a pair of grating strips with an equivalent area of x-directed current and (*ii*) by ignoring, to a good approximation, the imaginary part of the propagation constant over the distance of a

single unit cell. Using this approach, the θ- and ϕ-polarized components of the radiation pattern for the single unit cell can be written in the *xz*-plane as

$$E_\theta = f(\theta)\cos(\alpha)\left[1 - e^{j(k\sin\theta - \beta)d_2}\right] \tag{16a}$$

$$E_\phi = -f(\theta)\sin(\alpha)\cos(\theta)\left[1 + e^{j(k\sin\theta - \beta)d_2}\right] \tag{16b}$$

where k is the propagation constant in free space and β is the propagation constant in the image line. The function $f(\theta)$ is also dependent on the dimensions shown in Fig. 29; it is the same for both field components and is not considered here. To achieve right-hand circular polarization at the main beam angle, the left-hand component $E_L = E_\theta - jE_\phi$ must equal zero when $\theta = \theta_{-1}$. After making the appropriate substitutions, the condition for circular polarization reduces to

$$\tan\alpha = -\sec\theta_{-1}\tan\left(\frac{\pi d_2}{d_1}\right) \tag{17}$$

The above relation is an approximation in that it does not consider other effects such as the mutual coupling between the strips. In addition, although the radiation pattern is fan-shaped, (17) promises circular-polarization in the *xz*-plane alone, with axial ratio degrading away from the peak of the beam. A CP pencil beam may be produced, if desired, by building a planar array [23] of CP grating antennas.

The reconfigurable grating antenna previously shown in Fig. 27 is designed to demonstrate CP beam steering at 32.5 GHz. The image line's aspect ratio and dielectric constant are chosen in order to ensure single mode propagation over the *Ka*-band and to allow the dielectric cross-section to fit comfortably within the dimensions of a *Ka*-band waveguide. The image line used is 1.6 mm high, 6.4 mm wide and is fabricated from RT-Duroid 5880 ($\varepsilon_r = 2.2$). The image line is bonded to an aluminum ground plane, fed by a waveguide transition, and terminated with a matched load as shown in Fig. 27. Other transitions, including microstrip [66] and CPW [85] transitions, are also available.

The moveable dielectric film, also fabricated from RT-Duroid 5880, is 0.1 mm thick. Seven linear arrays of CP grating strips are used, with the grating spacing varying from $d_1 = 8.0$ mm to $d_1 = 5.0$ mm. This range of spacings is chosen to scan the main beam angle from $\theta_{-1} = -2°$ to $\theta_{-1} = -47°$ at 32.5 GHz. Once the grating spacings are chosen for each linear array, the parameters d_2 and α can be designed according to Equation (17) to achieve circular polarization at each main beam angle. All seven grating arrays use $d_2 = 1.2$ mm, with the strip rotation α chosen to increase according to (17) as d_1 decreases in order to maintain circular polarization across the scan range of the antenna. The widths of the grating strips are set at $w_s = 0.43$ mm, and the lengths of the strips l_s are chosen in accordance with the width of the dielectric image line. The length of the grating aperture is limited to 197 mm, as shown in Fig. 27, in order to allow convenient measurement in an available indoor antenna range.

C. Results and Discussion

Fig. 30 illustrates the variation in the main beam scan angle as the CP grating pattern is reconfigured along the surface of the image line. Experimental results agree well with the designed values obtained using Equation (8) together with the calculated guided wavelength along the image line. Axial ratio less than 1 dB is maintained at each scan state within the 32 to 33 GHz band. Input return loss is less than –15 dB across the same range of conditions.

Fig. 31 illustrates the θ- and ϕ-polarized components of the radiation pattern as the beam scans in the $\phi = 0°$ plane at 32.5 GHz. As the beam steers beyond –45° toward endfire, the axial ratio degrades. As the beam steers beyond –2° toward broadside, axial ratio remains low but the gain and pattern quality degrade due to the stopband resonance of the grating. The linear-polarized sidelobes in the $30° < \theta < 90°$ range are a result of spurious radiation from the waveguide feed. The sidelobes nearest the main beam, however, are circular polarized. The 3-dB beamwidth varies from 2.3° to 4.5° as the beam steers away from broadside. As expected, the radiation pattern in the non-scanning plane ($\phi = 90°$) is very broad, with axial ratio less than 3 dB maintained across only about 10° of arc near the main-beam angle. Table 2 lists the variation in the axial ratio, sidelobe level, and power gain as the beam scans at 32.5 GHz. The RHCP sidelobe level is more than 10 dB below the main beam across the scan range, and the axial ratio is below 1 dB over the same range within a ±500 MHz bandwidth.

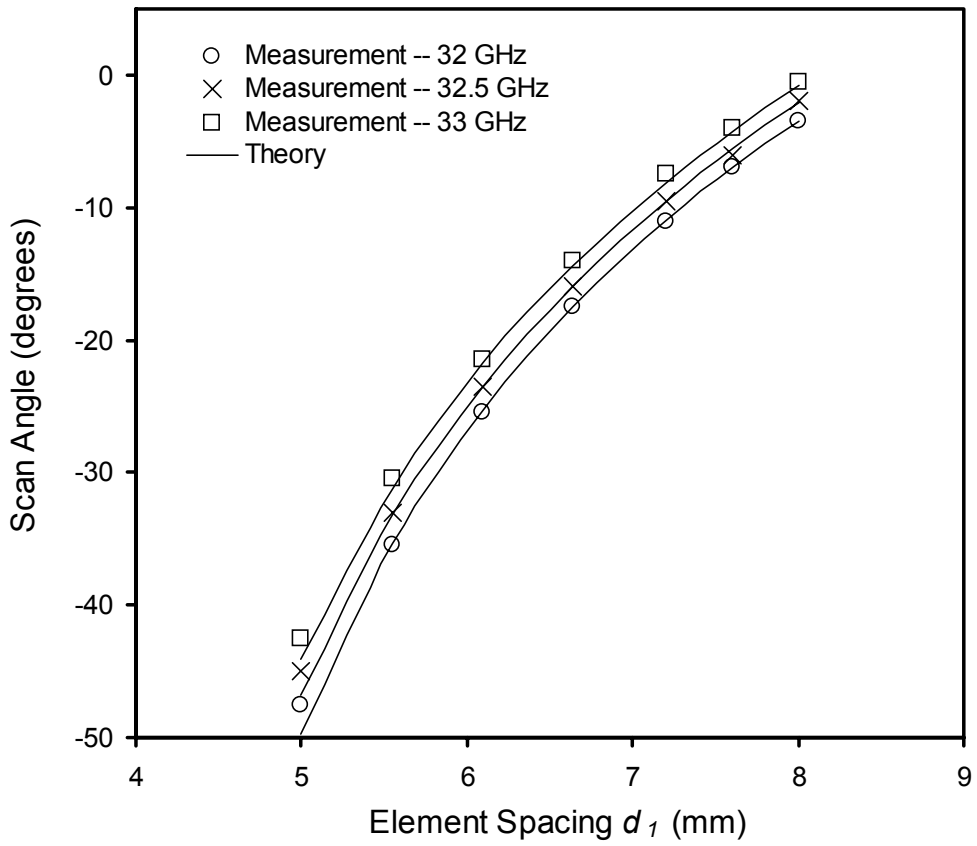

Fig. 30. Measured and calculated variation of the scan angle versus the inter-element spacing d_1 as the CP grating pattern is reconfigured along the surface of the image line.

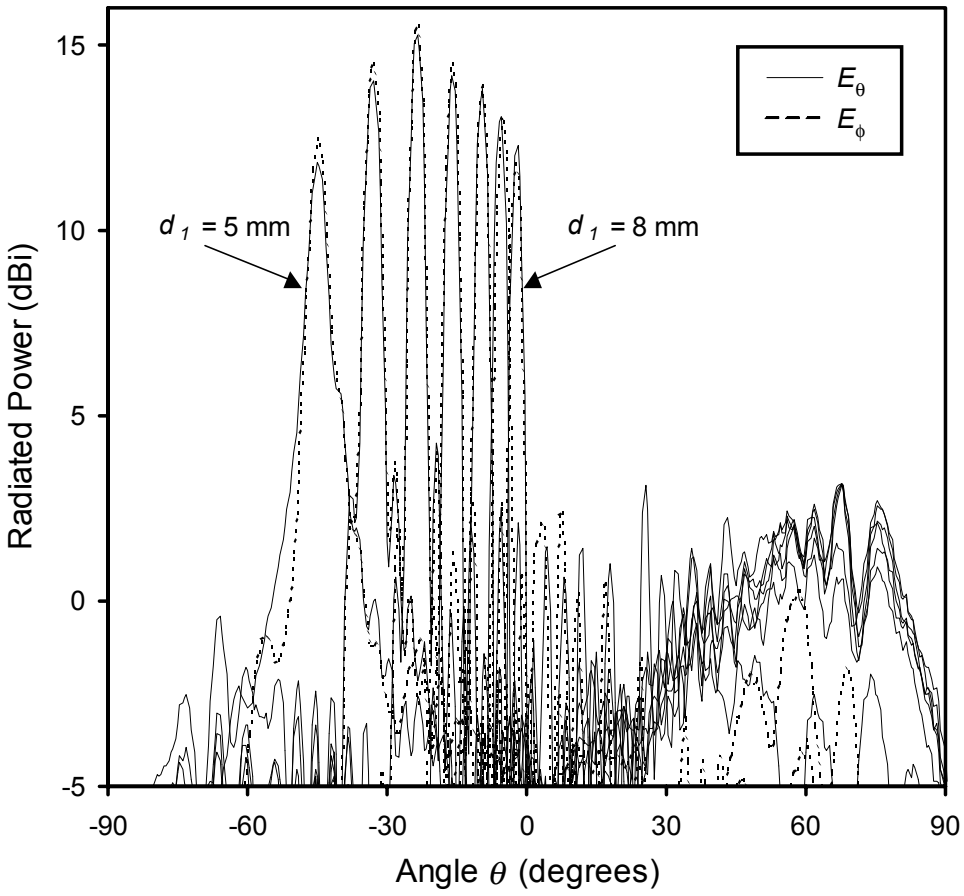

Fig. 31. Variation in the measured radiation pattern as the CP grating is reconfigured along the surface of the dielectric image line.

Table 2. Axial ratio, sidelobe level, and gain vs. element spacing at 32.5 GHz.

Scan Angle	Axial Ratio (dB)	Max Sidelobe Level, *RHCP* (dB down)	Power Gain *RHCP* (dBi)
-2°	0.47	10.7	14.6
-6°	0.09	11.3	16.8
-9.5°	0.13	11.6	16.0
-16°	0.31	11.9	17.2
-23.5°	0.25	11.3	18.3
-33°	0.45	10.7	17.1
-45°	0.63	12.6	14.7

The aperture efficiency of the grating itself reaches a maximum of 82 percent for the $d_1 = 6.09$ mm grating spacing. Including losses from the waveguide transition and from the unradiated power terminated at the end of the image line, the overall efficiency at this scan state is 36 percent. This underscores an important tradeoff in the CP grating design. For traditional grating antennas, the length of the antenna and the shape of the main beam can be designed by modifying the distribution of strip widths along the surface of the antenna. Unfortunately, for the CP grating design the strips must be sufficiently narrow in order to accommodate two strips within each unit cell. Since narrow strips radiate more slowly than wide strips, the CP design requires a longer length for the array in order to reduce the termination losses and achieve a desired level

of efficiency [22]. Optimizing the dielectric constant along the image line can help to increase the radiation rate, with associated tradeoffs [22], [87]. In this demonstration, the length of the antenna and its efficiency are restricted by the size of the available measurement range.

As mentioned above, axial ratio less than 1 dB is maintained within bandwidth of at least 1 GHz across a 43° scan range. It is noted that the reconfigurable antenna proposed in this chapter can easily accommodate multiple frequencies of operation by designing additional arrays of strips on the film to produce CP radiation at other *Ka*-band frequencies. Yet, the idealized theory given in (16) and (17) actually predicts axial ratio less than 1 dB across the entire 29 to 40 GHz range. In practice, other effects such as mutual coupling not included in the derivation of (17) limit the frequency response of each unit cell in the grating array. Even so, an extended 1-dB axial ratio bandwidth is achieved at the center of the scan range when $d_1 = 6.09$ mm. As shown in Fig. 32, the beam scans from –33.5° to –15° as the frequency varies from 30 to 35 GHz. As detailed in Table 3, axial ratio is better than 1 dB and sidelobes are more than 10 dB down across this range.

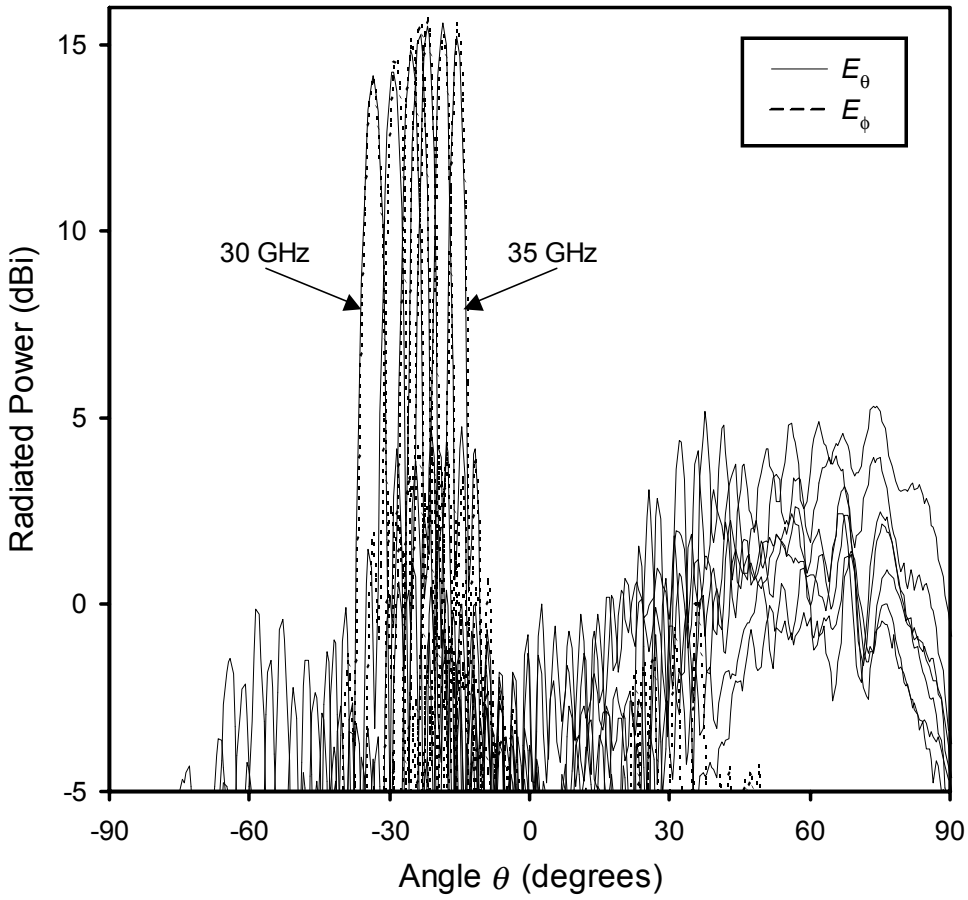

Fig. 32. Frequency scanning of the radiation pattern from 30 to 35 GHz for $d_1 = 6.09$ mm.

Table 3. Axial ratio, sidelobe level, and gain vs. frequency for $d_1 = 6.09$ mm.

Frequency (GHz)	Axial Ratio (dB)	Max Sidelobe Level, *RHCP* (dB down)	Power Gain *RHCP* (dBi)
30	0.13	10.7	17.1
31	0.30	10.4	17.3
32	0.29	10.6	17.9
32.5	0.25	11.3	18.3
33	0.19	11.5	18.5
34	0.36	11.3	18.2
35	0.34	11.4	18.2

For most system applications, the maximum bandwidth available at a given scan angle is limited not only by the degradation in the axial ratio with frequency but also by the dispersion of the main beam angle with frequency. The instantaneous bandwidth of the reconfigurable antenna can be defined as the range of frequencies surrounding the nominal operating frequency across which the main beam angle remains within its original half-power beamwidth [97]. This parameter is accurately approximated using the information included in Fig. 30 together with the measured beamwidth at each scan state, which varies on average by only 0.11° between the E_θ and E_ϕ patterns. Across the 32.5 GHz scan, the instantaneous bandwidth increases from 780 MHz at –45° to 890 MHz at –2°. Thus, the useful bandwidth of this scanning antenna is in practice limited

by the frequency scanning of the main beam angle rather than by the finite CP bandwidth of the grating structure.

D. Summary

This chapter has presented a low-cost reconfigurable antenna for circular-polarized millimeter-wave beam steering. The design features a CP grating array that can be reconfigured along the surface of a dielectric image line to allow fixed-frequency steering of a CP beam. A demonstration model designed using a simple analytical model has demonstrated over 43° of CP beam steering at 32.5 GHz with low axial ratio across the scan range. It is expected that this research will stimulate further investigations in the area of CP leaky-wave antennas and scanning antennas. The reconfigurable CP grating antenna presented in this chapter readily scales to higher frequency bands and should have many commercial and military applications in emerging millimeter-wave mobile satellite communications and related systems.

CHAPTER VI

NOVEL BROADBAND PHASED ARRAY TRANSCEIVERS*

This chapter presents novel phased array transceiver designs developed at Texas A&M University for extremely wide bandwidth operation. These designs use new broadband, low-cost microwave components to achieve system-level goals with minimal overall complexity. The system-level design for an 8 to 21 GHz phased array communication system is described, together with measured results that demonstrate the system's performance. Designs for a 10 to 35 GHz communications system and an 8 to 20 GHz radar system are also presented.

 Parts of this chapter are reprinted, with permission, from C.L. Wang, C.T. Rodenbeck, M.R. Coutant, and K. Chang, "A novel broadband T/R module for phased array applications in wireless communications," in *Proc. IEEE MTT-S Int. Microwave Symp. Dig.*, Seattle, WA, June 2002, pp. 1325-1328 and from T.Y. Yun, C.L. Wang, P. Zepeda, C.T. Rodenbeck, M.R. Coutant, M. Li, and Kai Chang, "A 10- to 21-GHz, low-cost, multifrequency, and full-duplex phased-array antenna system," *IEEE Trans. Antennas Propagat.*, vol. 50, no. 5, pp. 641-650, May 2002.

A. A 10 to 21 GHz Multi-Frequency Phased Array Transceiver for Mobile Satellite Communications

In mobile satellite communications (MSAT) systems, the idea is to use a constellation of low-earth-orbit (LEO) or medium-earth-orbit (MEO) satellites to communicate with mobile users on the earth's surface. This arrangement allows the mobile users to use their phones (or other data-transfer services) at remote locations not covered by traditional cellular communication systems. ICO Global Communications, Ellipsat, Archimedes, GlobalStar, and Iridium are examples of commercial MSAT systems [71]. The military is also actively interested in MSAT communications.

These MSAT systems can require beam-steering capability either for the mobile user or for the satellite or for both because LEO/MEO satellites move rapidly across the sky. However, classical phased arrays are overly expensive for the commercial market, and low-cost designs are called for. In addition, different MSAT systems may operate using different frequency bands. If a user needs to communicate with both systems, it would be useful if he could do so using a single mobile earth unit.

This section describes a low-cost phased array transceiver capable of operating at two widely separated frequency bands. The transceiver can transmit at 10 or 19 GHz and receive at 12 or 21 GHz. Both transmit and receive links use the same antenna array and operate simultaneously. A simplified diagram, shown in Fig. 33, illustrates the system's architecture. A single broadband, low-loss piezo-electric transducer (PET) phase shifter

[103] operates across all four frequency channels. This type of phase shifter is a new invention developed by researchers at Texas A&M. The four microstrip lines of the PET phase shifter connect at 90° angles with four transmit/receive (T/R) modules using K-connectors. Within each T/R module, two symmetric four-channel microstrip multiplexers [104] separate the transmit and receive links for amplification by discrete ultrabroadband monolithic microwave integrated circuit (MMIC) amplifiers. To avoid unintended feedback oscillations, both multiplexers together provide sufficient isolation across all frequencies to suppress the gain at any particular frequency around the T/R loop. Because the total gain of the amplifiers around the loop is nominally 50 dB, isolation for each of the two multiplexers must be 25 dB or greater in-band. A 1 x 4 H-plane array of broadband Vivaldi tapered slot antennas (TSAs) is connected to the front-ends of the T/R modules. Direct connections between the microstrip-line multiplexer and stripline TSA are used with low loss over the frequency range. An antenna element spacing of 10 mm is chosen by considering grating lobes, scanning blindness, and the size of the coaxial K-connector. Circular or dual-polarization can be accomplished by using another array perpendicular to the array shown in Figure 33.

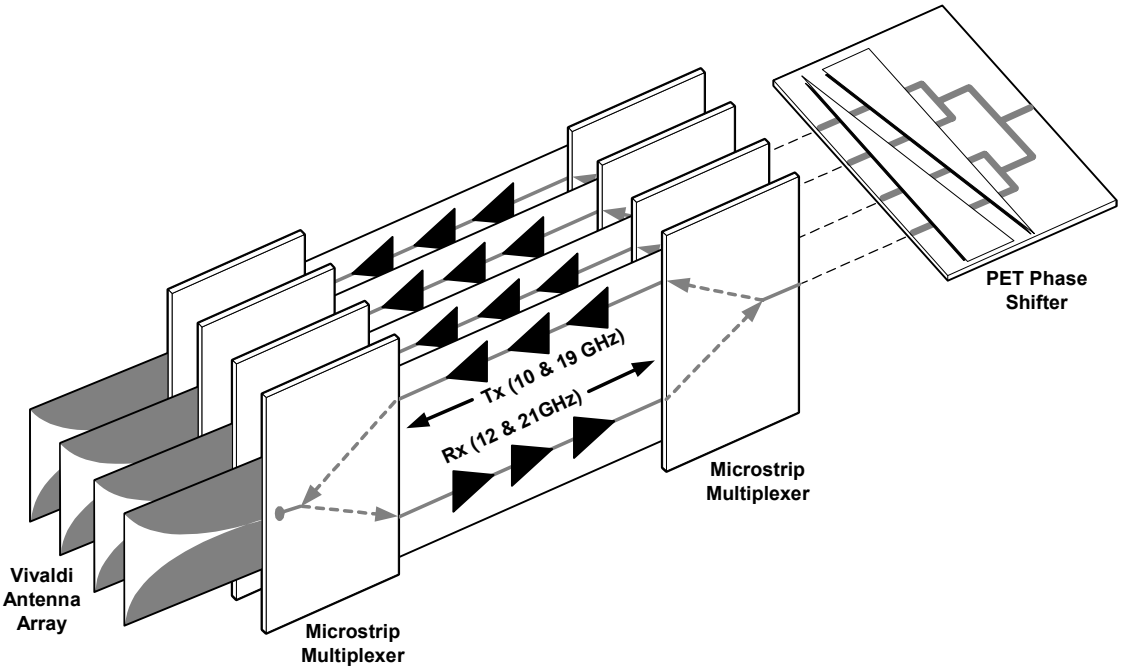

Fig. 33. System block diagram for the 8 to 21 GHz phased array.

Fig. 34 illustrates the layout of an individual T/R module. Two identical microstrip multiplexers are used in each module as separate broadband gain blocks for the transmit and receive paths, as shown in Fig. 33. The multiplexers are fabricated on an RT-Duroid soft substrate. Three MMIC amplifiers are used in both the transmit and the receive gain blocks. Each MMIC amplifier is mounted on a copper-molybdenum carrier to allow for individual testing as needed. Alumina thin-film networks (TFNs) and external bias capacitors and resistors are also mounted on the carriers. The TFNs provide connection pads for the bias wires and for the RF inputs and outputs of the MMICs.

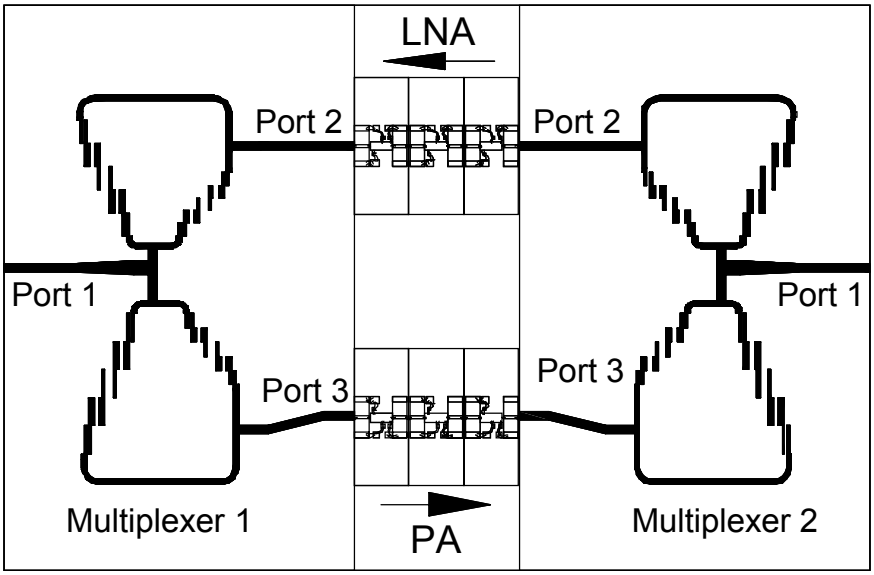

Fig. 34. Layout of the T/R module.

The MMIC amplifiers used in the transceiver are products available from TriQuint Semiconductor in Dallas, Texas. Table 4 lists the part number, nominal gain, P_{1dB} (output power at 1-dB power compression), and noise figure for each amplifier. The TGA8334 is a power amplifier (PA). The TGA8310 and TGA1342 are low-noise amplifiers (LNAs). The transmit channel amplifiers are chosen to provide moderate amplification with high P_{1dB} across the band, while the receive channel amplifiers are chosen to provide high gain with moderate noise figure across the band. In the transmit path, a TGA8310 acts as an initial gain stage, feeding a TGA8334 that has enough P_{1dB} to drive a final TGA8334 to saturation. In the receive path, two TGA1342s feed a TGA8310 because the TGA1342 has a lower noise figure, lowering the overall system noise figure.

Table 4. Nominal performance of the MMIC amplifiers.

Part Number	Component Type	Frequency (GHz)	P_{1dB} (dBm)	Gain (dB)	Noise Figure (dB)
TGA8334	PA	10	27	5.41	---
		19	20	8.17	---
TGA8310	LNA	10	17	9.60	---
		12	17	10.0	3.5
TGA1342	LNA	21	14	9.18	6.5
		12	17.5	10.7	3.7

Power compression curves for an entire T/R module are shown in Fig. 35. These results agree well with predictions based on the data in Table 4. Table 5 compares the measured and predicted gain, P_{1dB}, and noise figure for the same T/R module. Predicted performance agrees remarkably well with measurement. The receive gain at 21 GHz, however, is too low due to a defect in the upper limit of the frequency response of the LNAs. The parts donated by TriQuint are not fully qualified commercial parts; their poor high frequency response is the reason why they are available for use at Texas A&M. Fully operational parts should show improved gain at 21 GHz.

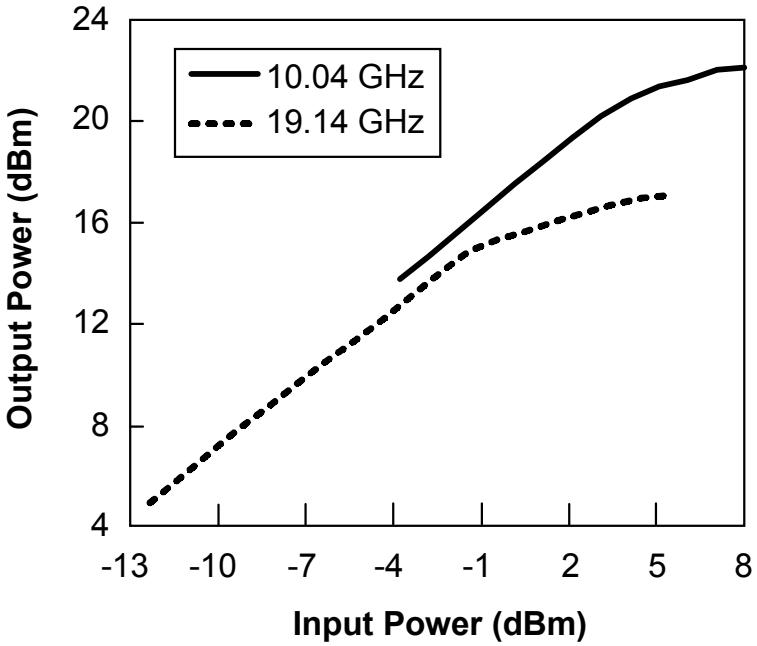

Fig. 35. Power compression curves for the T/R module.

Table 5. Measured and *predicted* performance of the transceiver.

Frequency (GHz)	Gain (dB)	P_{1dB} (dBm)	Noise Figure (dB)
10	16.7	21.0	------
	16.9	*21.1*	------
12	23.9	------	6.4
	23.7	------	*6.1*
19	17.2	15.1	------
	16.8	*15.6*	------
21	17.6	------	10.9
	19.0	------	*10.8*

The overall system in Fig. 33 achieves maximum scan angles of about 38° at all four frequency channels. For further information on the antenna patterns and phase shifter performance, the reader is referred to [105].

B. An 8 to 20 GHz CW/FMCW Phased Array Radar System Design

Ultra-wideband radar is currently an active field of research in the defense sector [106]. To be considered "ultra-wideband", a radar must have fractional bandwidth in excess of 25%. This is in contrast to conventional radars, which typically operate using bandwidths less than 1%.

This section presents the design of an 8 to 20 GHz CW/FMCW phased array radar. Continuous-wave (CW) radars can detect the direction and velocity of a target. Frequency-modulated CW (FMCW) radars can detect the direction, velocity, and range of a target. Fig. 36 shows the system block diagram of the proposed system. A CW or FMCW source feeds a broadband 1-W MMIC power amplifier module and transmit antenna array. The return signal is picked up by a receive antenna array, amplified by broadband low noise amplifier, and downconverted to baseband where information about the target can be identified using a spectrum analyzer. Both arrays are controlled by PET phase shifters that can be biased using a single variable voltage source.

Unlike the phased array communications system described in the previous section, the design in Fig. 36 uses separate antenna arrays for the transmitter and receiver. The

approach is referred to as bi-static radar and is required in this design to protect the receiver from RF transmit power. In the case of a communications system, the transmitter and receiver are isolated from one another typically by using separate transmit and receive frequencies. In a radar system, the transmitter and receiver must operate at the same frequency. If only one antenna is used, the receiver must be protected so that a portion of the high-power transmit signal does not leak into the receiver and damage or desensitize the LNA.

In the case of CW/FMCW radar, the transmitter and receiver must operate simultaneously. The antenna therefore cannot be switched between the transmitter and receiver as a means of isolating the two. In the ideal case, a circulator can be used to "duplex" the antenna. Unfortunately, circulators cannot provide isolation greater than about 15 dB over very broad bandwidths. This makes receiver protection for ultra-broadband CW radars impractical unless the target is so close to the radar system that the difference between the transmit and receive powers is not great (e.g., as in subsurface sensing radars). This is the chief justification for the bi-static approach used in Fig. 36.

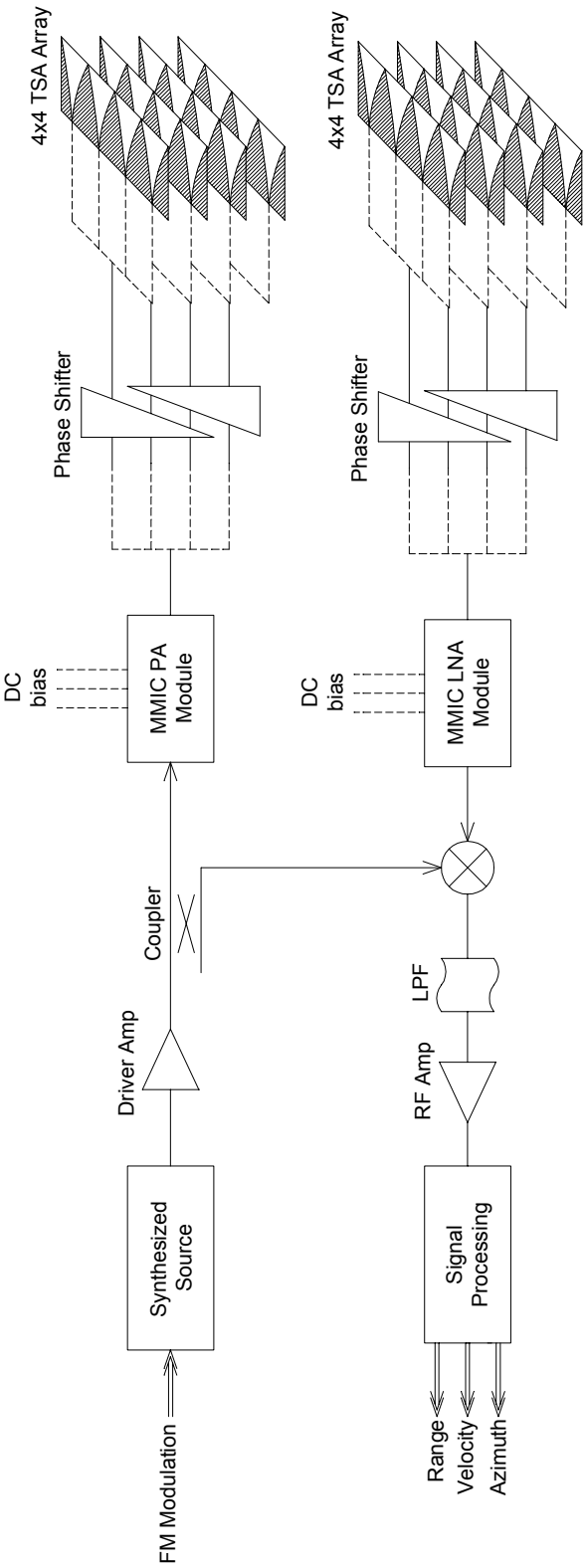

Figure 36. System block diagram for the 8 to 20 GHz phased array radar.

C. A 10 to 35 GHz Multi-Frequency Phased Array Transceiver Design

The system presented in Section A of this chapter can be extended to accommodate three transmit channels at 10, 19, and 32 GHz and three receive channels at 12, 21, and 35 GHz. A simplified diagram shown in Fig. 37 illustrates the system's architecture. There are four T/R modules in all. Each module feeds a 4 x 1 *E*-plane array of TSAs. The four T/R modules stack like bricks in the *H*-plane to form a 4 x 4 TSA array. A single PET phase shifter is used to control the relative phase length of all four T/R modules. This allows the phased array to scan one-dimensionally in the *H*-plane. Within each T/R module are four MMIC-based transmit and receive amplifiers. Two of those amplifiers operate over the 10 – 21 GHz range; the other two operate at *Ka*-band. Two multiplexers (Multiplexer A) route each of the six frequency channels to the correct amplifier. To allow the system to transmit and receive simultaneously, these multiplexers are designed as three-port passive microstrip filters. To avoid unintended feedback oscillations, both multiplexers must together provide sufficient isolation in order to suppress the gain at any particular frequency around the T/R loop. A different four-port microstrip multiplexer (Multiplexer B) is used at the back end of the entire system to interface the phased array with a modulator/demodulator.

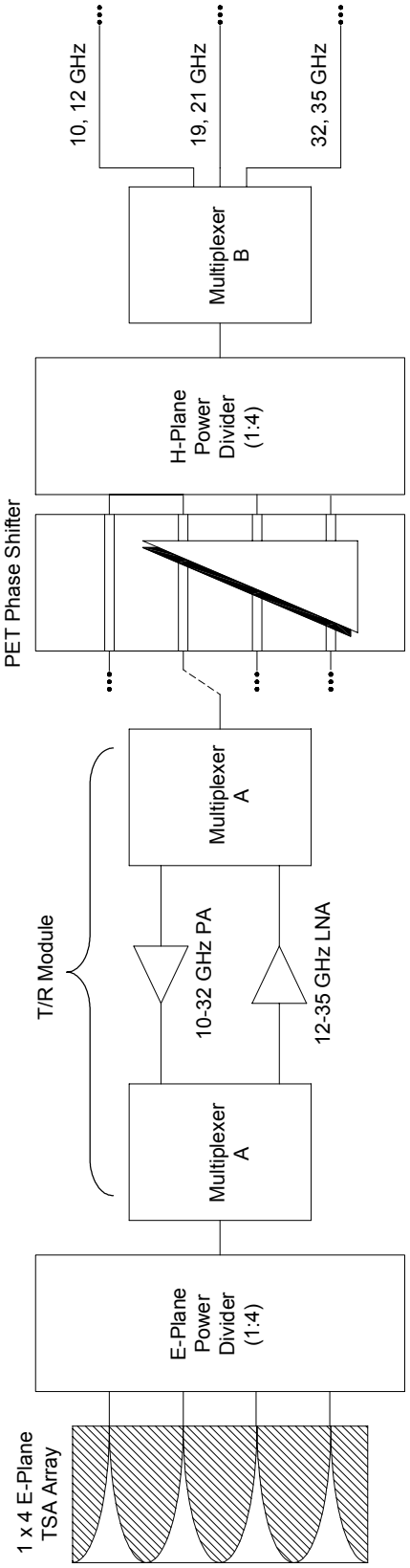

Figure 37. System block diagram for the 10 to 35 GHz phased array transceiver.

D. Summary

This chapter has presented novel designs for broadband low-cost phased array transceivers. These transceivers should have many applications in communication systems that require multi-frequency operation and in broadband CW radar systems.

CHAPTER VII

MONOLITHIC PIN DIODES*

The cost and complexity of a phased array can be reduced by increasing the level of integration within the system. Monolithic PIN diodes are a technology that can be used at frequencies up through the *Q*-band and beyond to miniaturize the phase shifters, switches, variable attenuators, and limiters commonly used in phased arrays. Furthermore, PIN diode-based control components can be integrated within monolithic microwave integrated circuits (MMICs) and directly interfaced with other active components, reducing the need for interconnects within the phased array system.

This chapter details a new bias-dependant small-signal modeling methodology for monolithic PIN diodes. The frequency-dependent responses of intrinsic *p*-*i*-*n* structures are de-embedded from MMIC PIN diodes of varying size and layout configuration and are fit from 6 to 45 GHz to a classical linear model at each of 15 different bias levels. This methodology results in a bias-dependent intrinsic diode dataset that shows excellent agreement with large samples of small-signal measurements. The models are useful for comparing tradeoffs in electrical performance among PIN diodes of varying size and

---

layout style. The methodology and resulting models have already found use in commercial design programs at TriQuint Semiconductor, Inc.

A. Background

A PIN diode is a two-port active device whose impedance at microwave frequencies is controlled by its DC bias. The diode's low off-state capacitance, small on-state resistance, and high power handling capability prove useful in a number of electronic applications including limiters, phase shifters, and both analog and digital attenuators [107]-[112]. A unique, high-yield process for fabricating GaAs MMIC Vertical PIN (VPIN) Diodes has been reported [113]. Fig. 38 illustrates the vertical profile of a typical VPIN diode. The perimeter of a VPIN "mesa" ranges from 50 μm to more than 160 μm. The thicknesses of the *p*-, *i*-, and *n*-layers, not shown to scale, are 0.25, 1.2, and 0.5 μm, respectively. VPINs have a reverse breakdown voltage greater than 35 V and display 4 nA of leakage current at 20 V reverse bias and a forward bias resistance as low as 2 ohms [114]. Implementing PIN diodes monolithically with other RF components such as resistors, capacitors, and transmission lines drastically reduces circuit size and complexity over traditional hybrid assemblies and allows designers to take full advantage of the devices' high intrinsic cutoff frequencies. Numerous commercial and military VPIN MMICs addressing frequency bands from 6 to 45 GHz have been fabricated over the past decade.

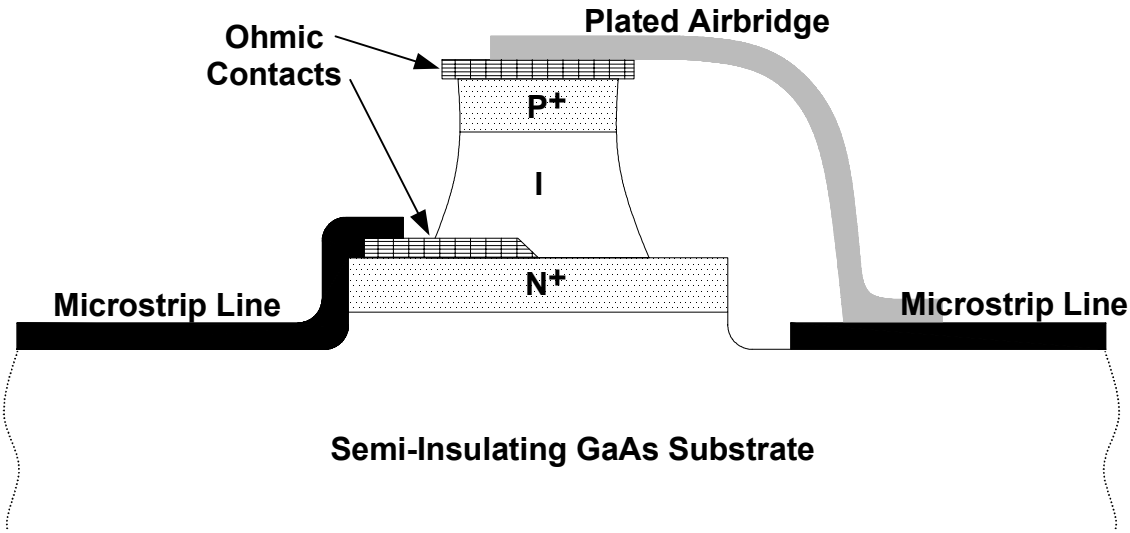

Fig. 38. Vertical profile of a VPIN diode.

Previous investigations, including those in [115] – [124], have conducted extensive research on the linear and nonlinear behavior of discrete PIN components. Very recently, two papers have presented a technique for extracting linear models for monolithic PIN diodes [125], [126]. The technique has two chief limitations. First, the models are extracted using an error function whose sensitivity to variations between measured and modeled *S*-parameters is highly dependent on the impedance state of the device. Low error function values may not necessarily indicate a good fit for both the reflection and transmission parameters at a particular bias state nor do they necessarily constrain the model to a physical solution. Secondly, the de-embedding technique used – electromagnetic simulation of the feed structure – does not scale well with frequency [127] and scales problematically with device size due to the difficulty in determining the

exact electrical reference planes between the vertical PIN structure and the upper and lower feed lines.

This study presents a systematic methodology for extracting broadband bias-dependent small-signal models for monolithic PIN diodes. Simple series and shunt test structures are used to extract the intrinsic diode parameters from the extrinsic feed structures at multiple bias levels for diodes of differing size and shape. De-embedding of the intrinsic device is accomplished using direct *S*-parameter measurements rather than electromagnetic simulation. The methodology shows excellent model versus measurement comparisons over the measurement range of 6 to 45 GHz for VPIN diodes from –3 V reverse bias through forward bias current densities as high as 100 A/mm^2. The resulting models are useful for comparing performance tradeoffs between diodes of varying size and layout style.

B. Small-Signal Response and Equivalent Circuit

The basic structure of the PIN diode consists of an intrinsic region between heavily doped *p* and *n* regions. Depending on whether the *i*-layer contains *n* or *p* impurities, a *pn* junction will form at zero bias between either the *p*- and *i*-layers or the *n*- and *i*-layers. What makes the PIN diode unique is that the *pn* junction has a negligible effect on the small-signal performance of the diode at frequencies above the transit time frequency of the *i*-layer [107]. In the TriQuint VPIN process, the response contribution of the *pn* junction can be ignored above 80 MHz [128].

Consider the classical PIN diode lumped-element model presented in Fig. 39 [129]. The parameters R_i and C_i represent the resistance and capacitance of the *i*-region. R_d represents the conductance of the depletion region. C_d models both the junction and the diffusion capacitance across the depletion region. R_s accounts for the contact resistance of the anode and cathode, together with the total bulk resistance of the *p*- and *n*-layers. All of these intrinsic parameters, except R_s, are heavily dependent on the layout of the diode as well as the operating DC current through the diode. Changes in the intrinsic diode parameters occur as mobile carriers are injected into the diode's *i*-region under applied forward bias. For the GaAs devices considered in this study, the change in the parameters is very rapid starting at zero bias and usually saturating at a current density of 15 A/mm^2 of intrinsic diode cross-sectional area. The non-linearity is particularly troublesome to model over a large frequency range for many different diode sizes and layout styles.

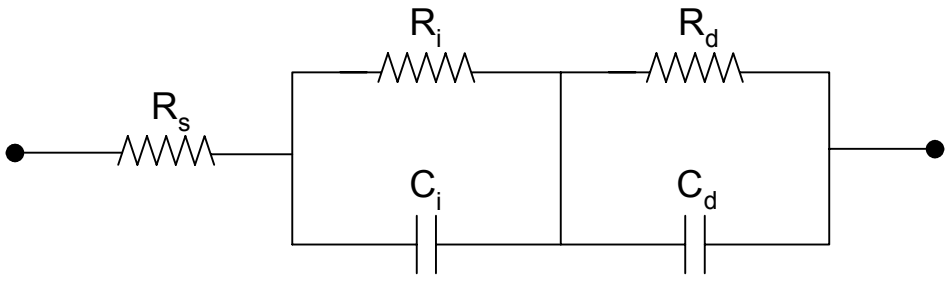

Fig. 39. Linear model for the PIN diode.

C. Modeling Methodology

There are three significant findings in the work discussed in this chapter. First, this research has shown that the classical PIN diode lumped-element model in Fig. 39 can be used up through 45 GHz on VPIN diodes providing the extrinsic feed structure is properly de-embedded. Secondly, a bias-dependant PIN model may be accurately obtained over a large frequency range using a table-based approach. Finally, this study indicates that two port measurements of simple series and shunt connected diodes should be used to obtain the greatest balance of model optimization sensitivity over all bias conditions.

1. Procedure for Fitting the Intrinsic Diode Model

Computer-controlled network analyzers using automatic bias measurement routines can change the diode current to predetermined levels and take broadband two-port vector measurements. For each particular diode size and layout style studied, vector measurements from 6-45 GHz are taken from multiple VPIN samples. The linear PIN diode model parameters are then de-embedded for each recorded bias level, averaged among the diode samples, and indexed in terms of current density into a table of intrinsic models.

Because the impedance of PIN diodes becomes very small under sufficient forward bias, it becomes difficult to obtain reasonable results for fitting the model using data taken from series or shunt configurations alone. A large number of solutions would result in a

satisfactory fit at each bias level without guaranteeing that the results are repeatable among the diodes sampled. To constrain the solution to the actual set of physical diode parameters, the same set of model parameters is fit simultaneously to both series and shunt connected diode configurations. Photographs of a series and shunt VPIN test structure are shown in Figs. 40 and 41. In the case of the shunt diode configurations, the parasitic effects of the grounding via, which become appreciable at millimeter-wave frequencies, can easily and accurately be de-embedded from the measured small-signal response through 45 GHz by using a simple empirical model.

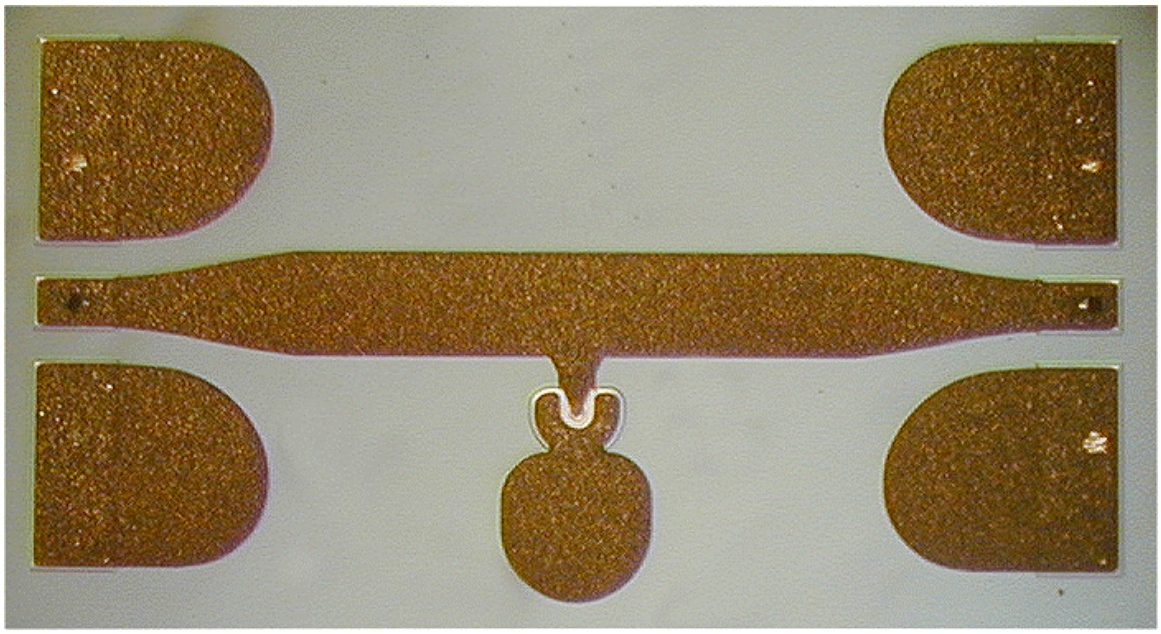

Fig. 40. Photograph of a shunt VPIN test structure.

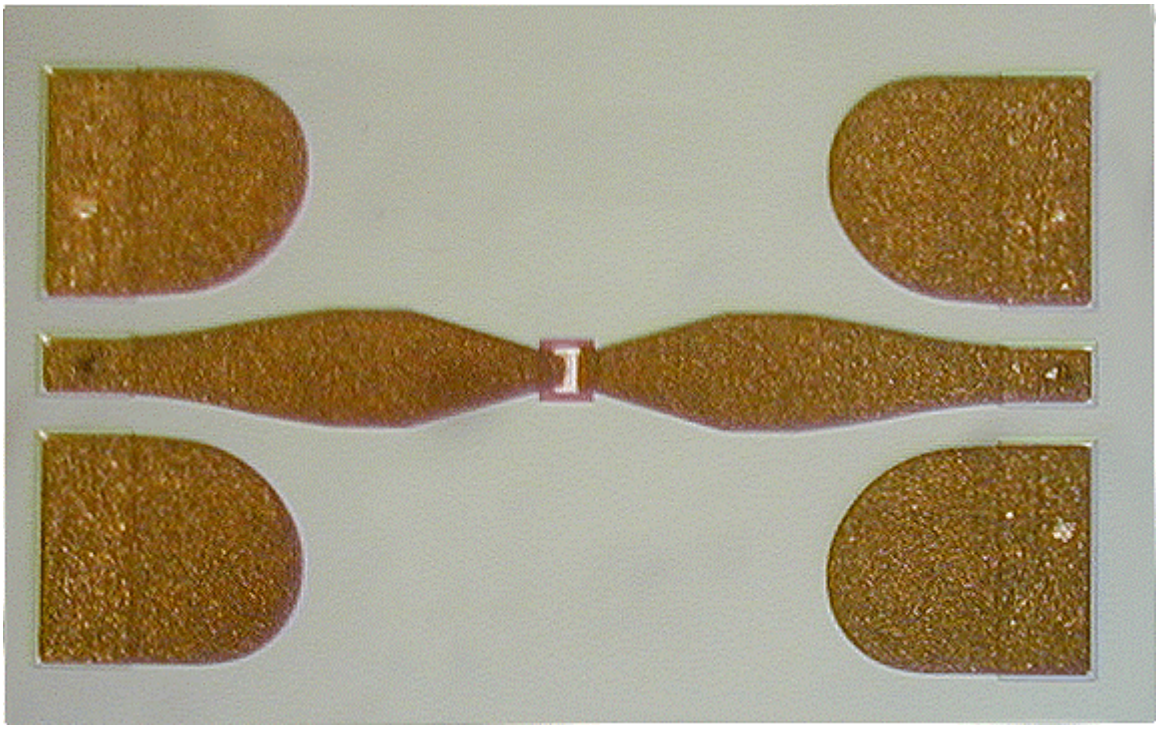

Fig. 41. Photograph of a series VPIN test structure.

The results presented in this chapter use a gradient optimizer to fit the modeled VPIN intrinsic parameters to the measured responses of the series and shunt test structures. The optimization routine uses the mean-square error function given in (18). Here, f_k represents the set of N_j frequencies in the j^{th} frequency range. $H_o(f_k)_{ij}$ and $H(f_k)_{ij}$ are the i^{th} measured and modeled frequency-dependent small-signal responses, respectively (e.g., measured and modeled S_{21}, S_{11}, etc.).

$$Error = \sum_j \frac{1}{N_j} \sum_{f_k} \sum_i \left| \frac{H(f_k)_{ij} - H_o(f_k)_{ij}}{H_o(f_k)_{ij}} \right|^2 \tag{18}$$

The frequency-dependent responses empirically found to be best for optimization are S_{21}, input impedance Z_{in}, and output impedance Z_{out} – for both the series and shunt cases. Both magnitude and phase information are included in the error calculation. Z_{in} and Z_{out} are used rather than S_{11} and S_{22} so that, when the input impedance is nearly 50 ohms, the error function is conveniently heavily weighted to S_{21}. Unimportant deviations between measured and modeled S_{11} and S_{22}, when they are so small, would otherwise produce unduly large percent errors, so their influence on the modeled parameters is accordingly minimized.

2. Procedure for De-Embedding the Diode Feed Structure

Correctly modeling the intrinsic parameters of a VPIN diode over a broad frequency range requires that the effects of the diode feed structure (extrinsic parameters) be de-embedded from the measured data before the intrinsic linear diode model is extracted at each tested bias level. The test structure that allows for the best extraction is the series configuration in a reversed biased state. Reverse biasing the diode sweeps all charge out of the i-layer allowing a simple RC element to describe the intrinsic diode model in the high-impedance state. The influence of the feed structure then becomes dominant and permits more accurate extraction of the feed parameters, which can vary significantly for different diode layouts.

The de-embedding procedure is adapted for the specific diode layout configurations shown in Fig. 42. The round diode in Fig. 42(a) represents TriQuint's traditional VPIN

diode layout. The elongated diode of Fig. 42(b) is a newer design that takes up less MMIC area than a round diode structure of equal intrinsic perimeter and whose artwork is more easily scaled to different dimensions. For each configuration, empirical models are derived from examining the layout of the diodes and creating standard microstrip models with appropriate physical lengths for the feeds. In the case of the anode airbridge, the effective dielectric constant of the tapered transmission line is modified to account for the 2 μm air gap between the microstrip and GaAs substrate. Afterward, the lengths of the distributed feeds are tuned and parasitic elements added while comparing the simulations to reverse bias measurements. Although commercial electromagnetic simulation was initially attempted to model the extrinsic diode feed structure, standard microstrip transmission line models are found to yield equally accurate results for de-embedding purposes and yet are less time-consuming to formulate. Due to slight variations in measurement probe placement, difficulties arise in precisely determining the reference planes between the measurement probes and the intrinsic anode and cathode. For this reason, the microstrip elements representing the microstrip up to the feeds are also adjusted slightly over ±0.5 mils to account for possible probe tip placement variability. Both feed styles are modeled using this process over the entire 6 to 45 GHz range of frequencies with excellent fit.

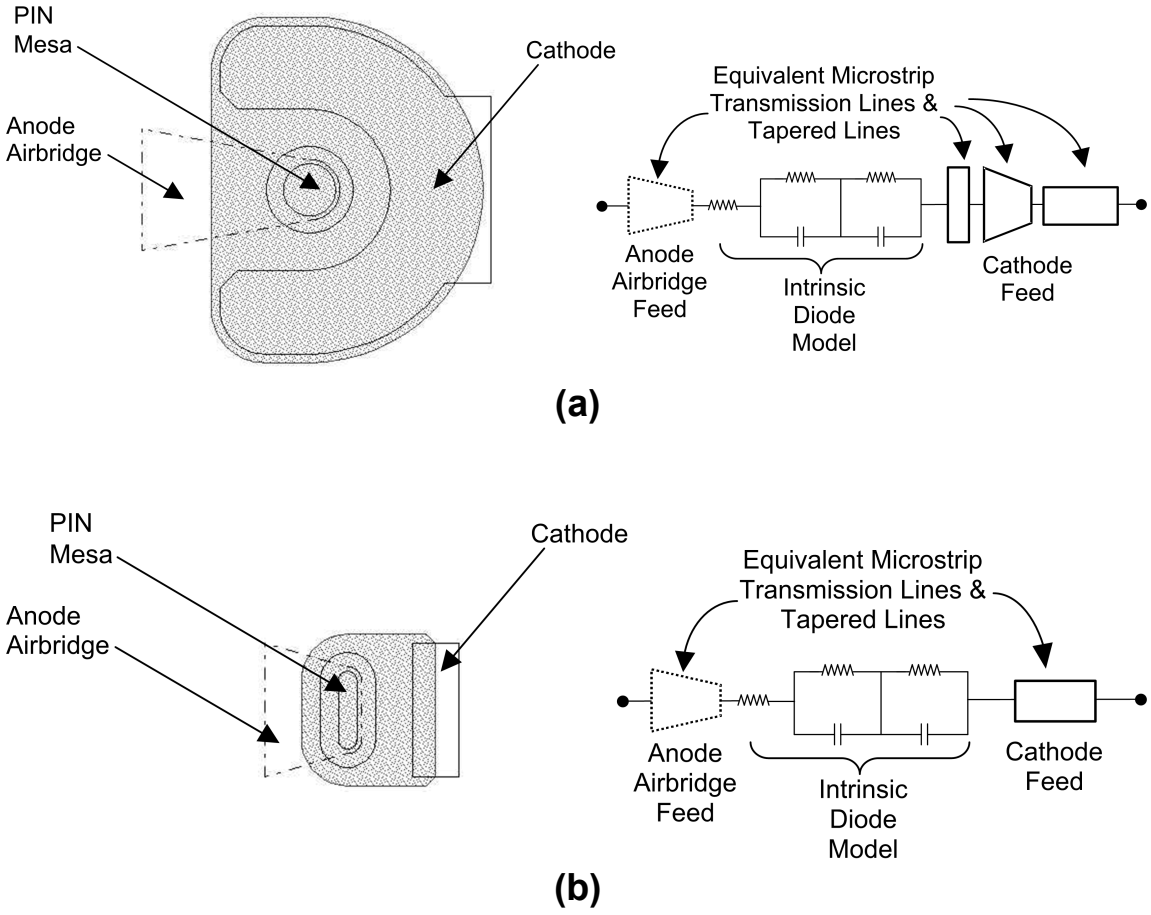

Fig. 42. Layouts and de-embedding networks for (a) round and (b) elongated diode structures.

D. Modeling Results

The modeling methodology presented above is used to study the small-signal responses of VPIN diodes from reversed through forward bias. Series and shunt test structures for elongated diodes of 80, 95, 110, and 160 μm perimeter and round diodes of 80 and 95 μm perimeter are tested at –3 V reverse bias, zero bias, and at 13 forward bias current densities from 0.3 to 100 A/mm^2. Series *S*-parameters from 6 to 45 GHz and shunt *S*-parameters from 6 to 40 GHz are de-embedded at each tested bias condition. For each diode size and layout style considered, the linear diode model is fit individually to a minimum of four series and shunt diode pairs. These results are then averaged into a single dataset for each diode and compared with averaged *S*-parameter data in terms of both magnitude and phase. Percent errors between the models and averaged measurements are well below 5% over the ranges of optimization, typically below 2.5%. To illustrate the close correspondence between the measured and modeled small-signal responses in even the transitional diode states, measured and modeled S_{11} and S_{21} for the 80 μm elongated diode at 0.33 A/mm^2 forward bias are plotted in Fig. 43. This bias state represents the "worst-case" modeling results for this particular diode layout.

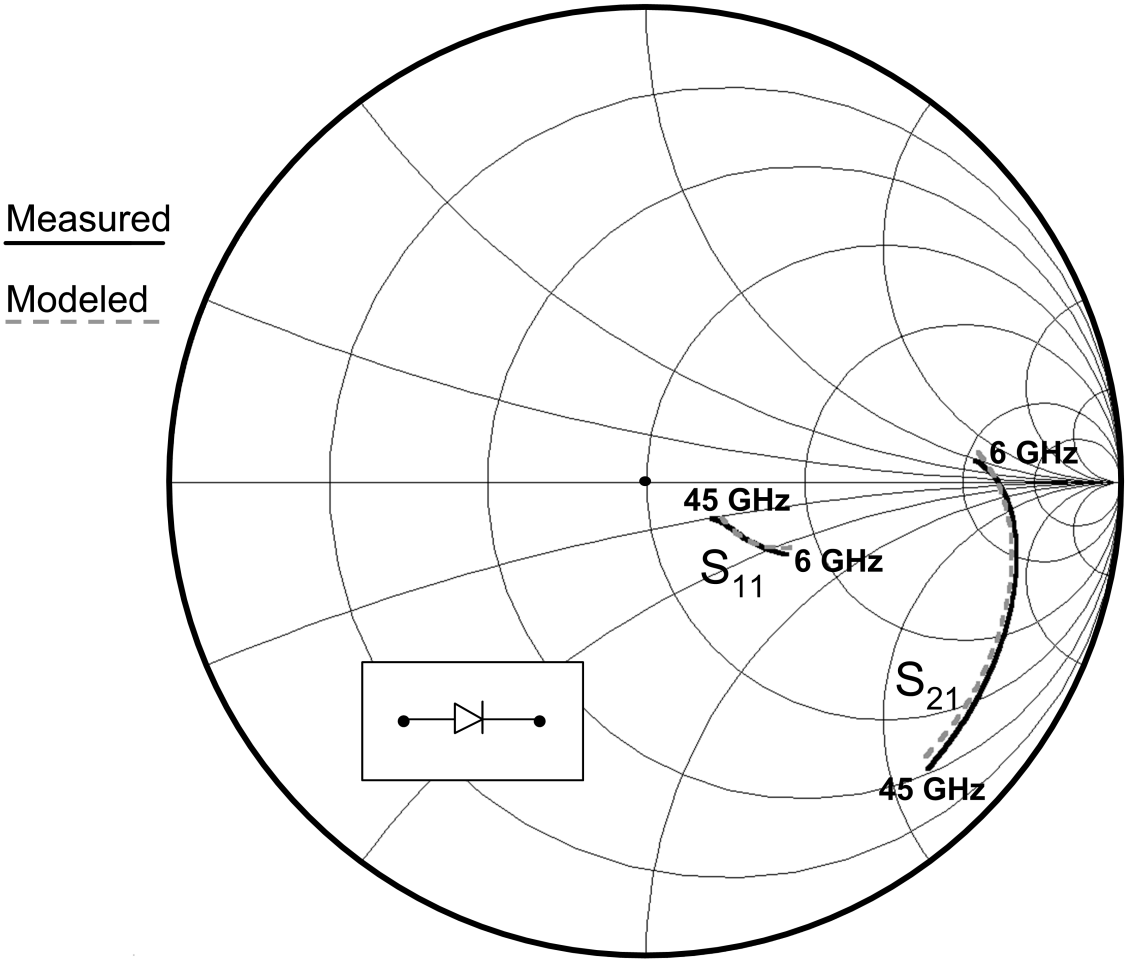

(a)

Fig. 43. Modeled values of S_{11} and S_{21} for an elongated diode 80 μm in perimeter at 0.33 A/mm^2 forward bias are plotted over the frequencies of optimization against measured data averaged from four series and shunt diode pairs. (a) Series test structure. (b) Shunt test structure. This bias state represents the "worst-case" modeling results for this particular diode layout.

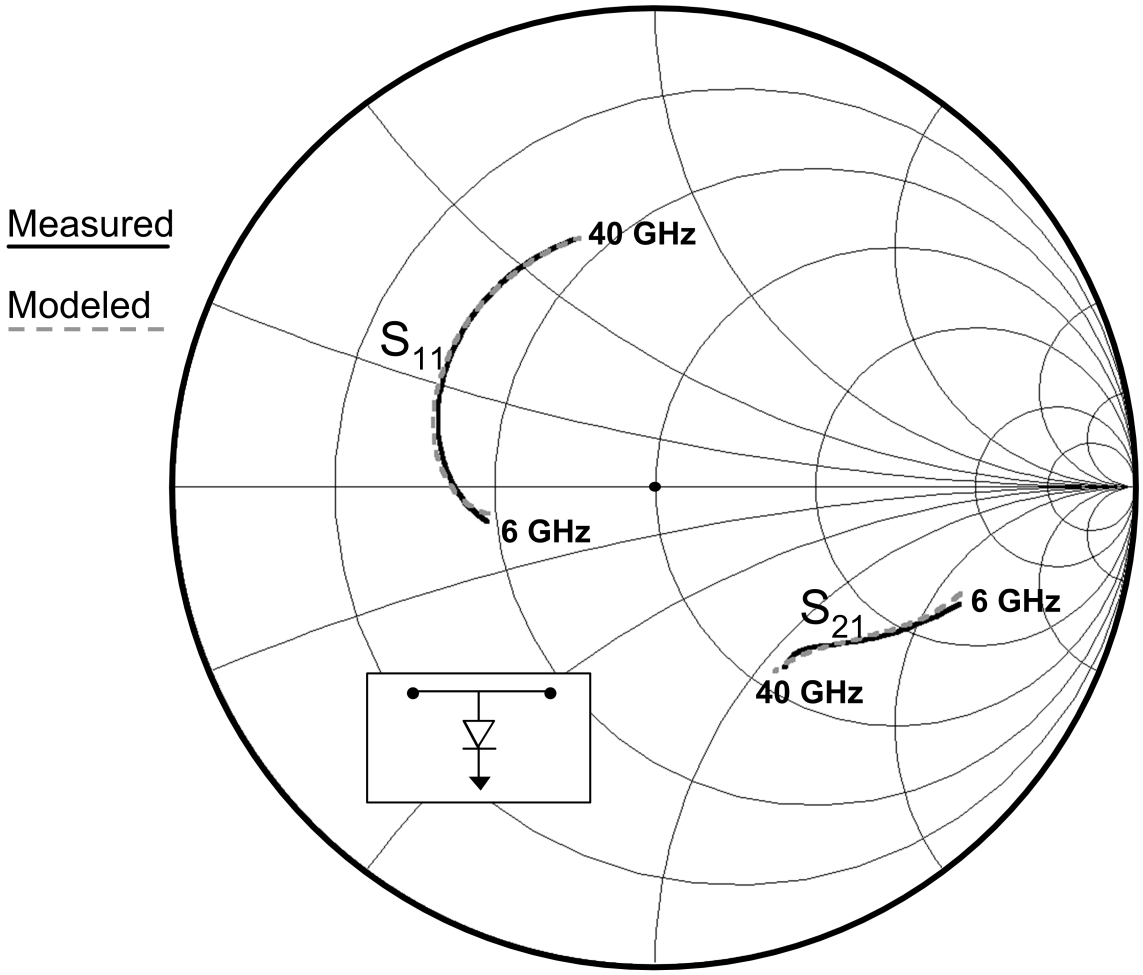

Fig. 43 continued.

Fig. 44 illustrates how the intrinsic parameters of the 80 μm elongated diode vary under forward bias. Similar trends are observed for the other diode sizes and structures. The intrinsic capacitances, C_d and C_i, increase linearly until the diodes are completely turned-on at a current density of about 15 A/mm^2. At this point, continuing to increase C_d and C_i affects the frequency response of the modeled diode parameters only

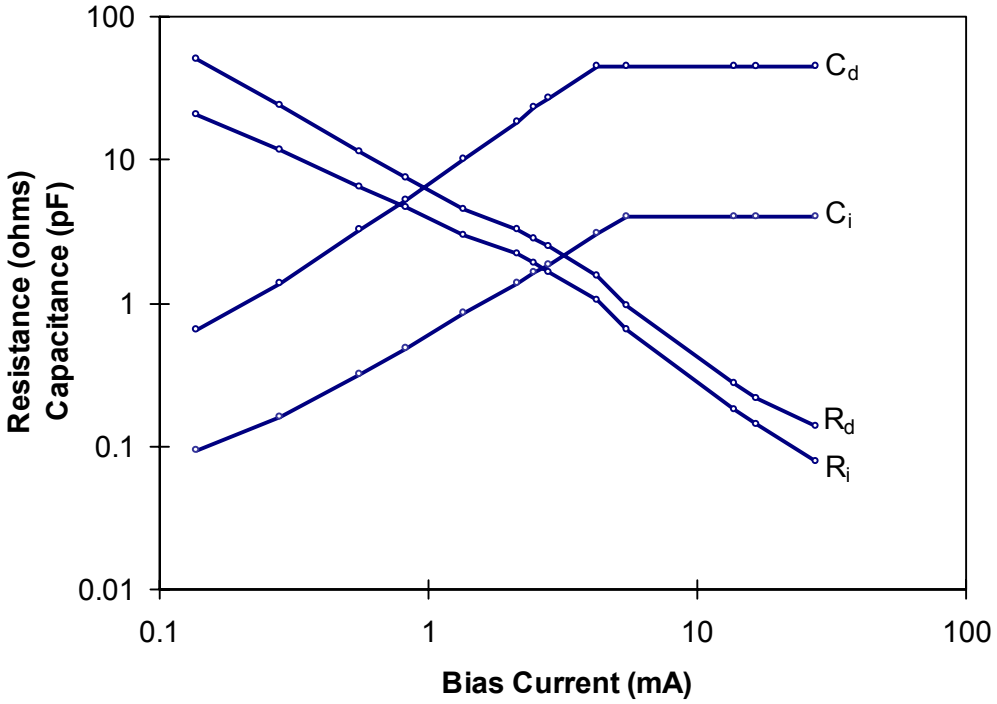

Fig. 44. Modeled intrinsic parameters versus forward bias current for an elongated diode 80 μm in perimeter.

insignificantly, and thus the optimized values are forcibly saturated. The diode resistances, R_d and R_i, decrease to very small values at high bias currents. The bulk/contact resistance, R_s, not shown in the figure, decreases weakly with increasing forward bias, by as much as 20% from its value at reverse bias. This variation occurs after the intrinsic capacitances have saturated as the *i*-layer effectively thickens under heavy forward bias to include portions of the *p*- and *n*-layers [129].

Fig. 45 illustrates the scaling of modeled parameters at reverse bias and maximum forward bias. It is noted that the 80 μm round diode, fabricated using a process that greatly reduced the diode's contact resistance, is not included in the comparison of Fig. 45(a). Fig. 45(a) illustrates how total modeled diode resistance under forward bias varies approximately linearly with diode perimeter. In addition, the reader may note that experimental findings in [130] demonstrate how the input power at which VPIN diodes experience catastrophic failure is also a strong linear function of diode perimeter. For zero and reverse bias conditions, R_d, R_i, and C_d are fixed at very large values so that the linear diode model consists only of R_s and C_i in series. As shown in Fig. 45(b), the modeled off-state capacitance of the diodes increases linearly with diode area. Both graphs demonstrate how accurate scaling coefficients can be extracted with linear curves fit by least squares regression.

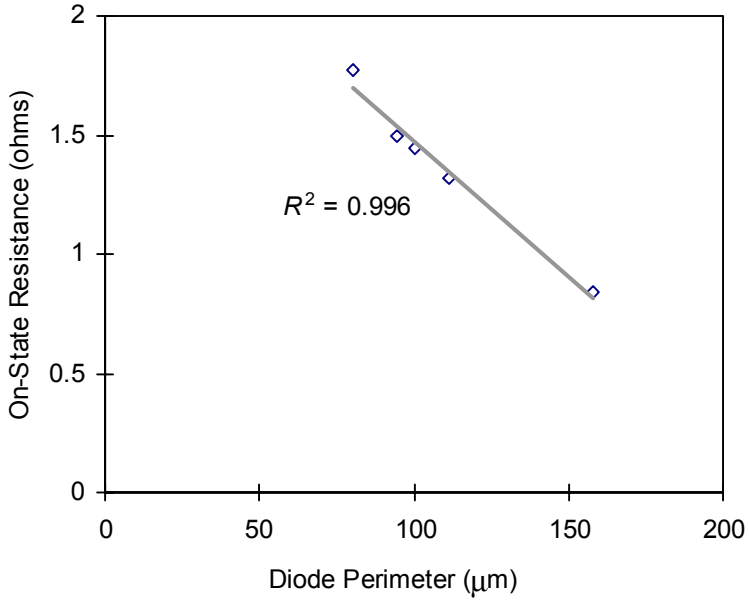

(a)

Fig. 45. Diode scaling. (a) Modeled on-state resistance vs. intrinsic diode perimeter. (b) Modeled off-state capacitance vs. intrinsic diode area. Both curves are fit to linear curves using least squares regression. Correlation coefficient (R^2) values are shown.

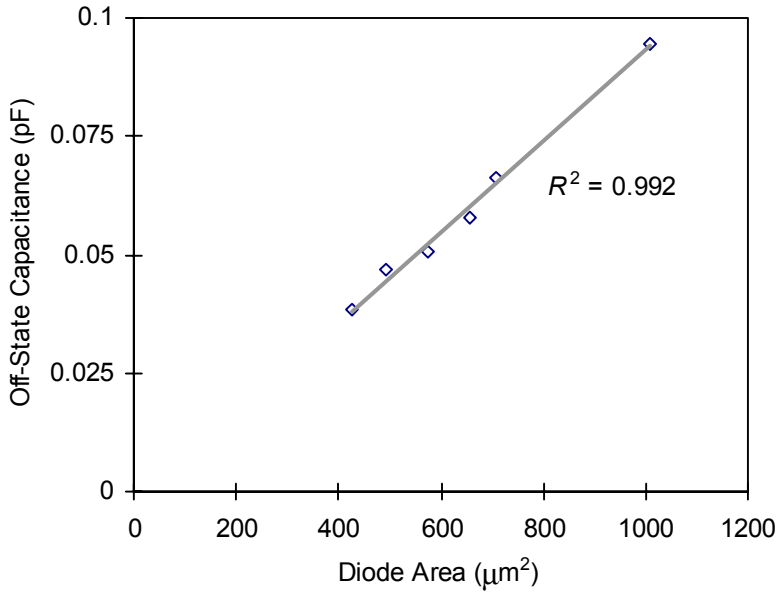

(b)

Fig. 45 continued.

E. Using the Diode Model to Compare Diode Layout Styles

The linear diode model developed in this study may be used to demonstrate the advantages of the elongated VPIN layout style over the conventional round style with respect to small-signal performance. The modeling results shown in Fig. 45 have illustrated how off-state capacitance increases linearly with intrinsic diode area while on-state resistance decreases linearly with intrinsic diode perimeter. Because the circular geometry of the round diode represents the maximum ratio of diode area to diode perimeter, it yields the highest achievable ratio of off-state capacitance to on-state resistance. Thus, an elongated diode displays less off-state capacitance for the same

amount of on-state resistance as a round diode of equal perimeter, allowing greater transmission bandwidth for the same amount of on-state signal attenuation.

As a quantitative comparison, one may consider the cutoff frequency f_c, a commonly used figure of merit in PIN applications,

$$f_c = \frac{1}{2\pi R_{on} C_{off}} \tag{19}$$

where R_{on} and C_{off} represent the equivalent on-state resistance and off-state capacitance of the diode, respectively [131]. For VPIN devices 80 μm in perimeter, the linearized models presented in Fig. 45 predict that using the elongated layout style rather that the conventional round configuration results in a 21% increase in the cutoff frequency. This increase grows linearly to 102% for diodes 160 μm in perimeter. From a design perspective, the relative increase in cutoff frequency between the two diode styles for a particular diode perimeter represents a corresponding increase in transmission bandwidth at a particular level of on-state resistance.

F. Summary

This chapter has presented a methodology for modeling the small-signal performance of monolithic PIN diodes. Using a classical linear model, intrinsic diode parameters have been de-embedded from large samples of series and shunt test structures at multiple bias

levels for different diode sizes and layout styles. The resulting intrinsic diode dataset has shown excellent agreement with measured data even at millimeter wave frequencies up to 45 GHz and has proven useful for quantitatively characterizing the diodes' nonlinear response from reversed through forward bias. In addition, the models developed using this methodology have been used successfully demonstrate a new diode layout configuration to have an intrinsic cutoff frequency up to 102% higher than that of a conventional diode of equivalent on-state resistance. These results are expected to expedite and improve MMIC designs that use monolithic PIN diodes and to hasten the acceptance of this technology in microwave and millimeter-wave phased array systems.

CHAPTER VIII

A PHASED-ARRAY ARCHITECTURE FOR RETRODIRECTIVE MICROWAVE POWER TRANSMISSION FROM THE SPACE SOLAR POWER SATELLITE*

This chapter presents a phased-array architecture for retrodirective microwave wireless power transmission from the space solar power satellite (SPS). The proposed architecture uses a 2.9-GHz pilot beam and a 5.8-GHz transmit beam, with retrodirective phasing implemented directly at RF. This design has the potential to reduce the size and cost of future SPS systems. Experimental and theoretical results are given to validate the approach.

A. Background

The SPS concept envisions a satellite placed in geosynchronous orbit for collecting and converting solar power to electrical power. The SPS satellite continuously transmits the electrical power it generates down to the earth using a microwave beam. On the earth's surface, the microwave beam can be received and converted back to electrical power on the gigawatt scale using a rectifying antenna array or "rectenna" array. To ensure

---

 Parts of this chapter are reprinted, with permission, from C.T. Rodenbeck, M. Li, and K. Chang, "A phased-array architecture for retrodirective microwave power transmission from the space solar power satellite," to appear in *Proc. IEEE MTT-S Int. Microwave Symp. Dig.*, Fort Worth, TX, June 2004.

maximum operating efficiency and to eliminate environmental concerns, the microwave transmission system uses retrodirective control. That is, a pilot beam signal transmitted from the phase center of the rectenna site to the orbiting satellite ensures that the high-power microwave beam always points on-target. The SPS system would make solar power available for baseline electrical power during 99% of the year and operate with a dc-to-dc conversion efficiency greater than 45% [132], [133].

The SPS idea originated in 1968 and was the subject of considerable investigation during the 1970's, culminating in a 1981 report to Congress [134] that identified SPS, together with nuclear fusion, as the only two foreseeable options for inexhaustible baseline electrical power. Since 1995, research on this topic has accelerated once again with teams in both the US and Japan investigating various engineering aspects of the SPS system. Recently, a fresh look has been taken at the development of modern rectenna arrays and at the design of the space-based retrodirective transmitter [133], [135], [136].

The previously proposed retrodirective array [132], [136]-[138] operates as a phased array transmitting a 1.78-GW Gaussian beam at 5.8 GHz. The array is 500 m in diameter, containing approximately 20,000 1 m x 1 m subarrays. A receive antenna nested within each of the transmit subarrays picks up the pilot beam signal incident on the face of the transmit array. The received pilot signal is down-converted at each subarray to a low frequency where digital electronics can be used to compare the received phase with an internal reference phase. The phase difference is conjugated and

then impressed on the phase of the outgoing high-power microwave signal. Conjugating the received phase across the surface of the transmit antenna ensures that the high-power microwave beam focuses in the direction of the incoming pilot beam signal. This arrangement is preferred to a simpler approach, such as monopulse tracking, since precise phasing of each subarray is required to maintain overall system efficiency. Without phased array control, small tilts in each subarray arising from thermal expansion and contraction could greatly reduce overall system efficiency.

This chapter presents an alternative architecture for retrodirective control of the SPS transmitter. Rather than convert the pilot-beam signal to a low frequency where its phase can be conjugated using digital logic, it is possible to directly conjugate the phase of the received signal at RF and then retransmit the conjugated signal. Such an arrangement has certain advantages. Fewer electronics would be needed per subarray with the potential for reduced power consumption and reduced sensitivity to thermal variations. In addition, conjugating the signal at RF allows the beam to make an instantaneous adjustment to any misalignment between the transmitter and receiver.

The proposed design is unconventional in several aspects. Unlike retrodirective arrays currently advocated for use in wireless communications, SPS system tradeoffs require that the individual subarrays be highly directive and electrically large [136]. Although using large subarrays limits the available scan range, the ultimate application only requires about 15 arcminutes of scanning. What is more, the SPS phased array

transceiver requires nearly unprecedented isolation between the transmit and receive powers, making necessary a substantial separation in frequency between the transmit and receive signals. To meet this demand, the design presented here uses a second-harmonic approach that allows a 2.9-GHz pilot beam to guide the 5.8-GHz transmit beam.

The following sections of this chapter describe this phased array architecture in greater detail, providing experimental and theoretical support for its validity.

B. Second-Harmonic Retrodirective Transceiver

Fig. 46 illustrates a single element within a classical RF retrodirective array. The element receives an incoming pilot signal of frequency ω_1 and phase ϕ_1. The received signal mixes with an internal reference source of frequency $2\omega_1$. The mixing process generates a tone at ω_1 whose phase $-\phi_1$ is the conjugate of the received signal's phase. If the internal reference source presents the same phase at each element of the array, then the retransmitted beam points in the same direction as the incident pilot beam.

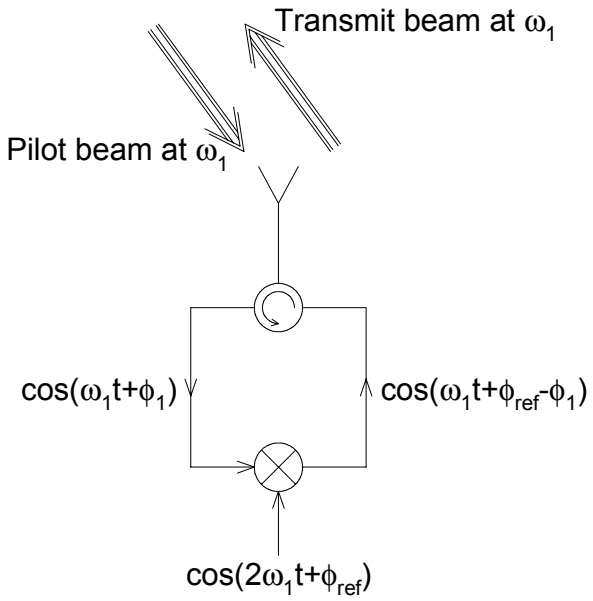

Fig. 46. A unit element within a classical RF retrodirective array.

In the present case, the goal is to receive a pilot signal at ω_1 and transmit back in the same direction but at a frequency of $2\omega_1$. Although mixing the incoming signal with a reference source at $3\omega_1$ would produce a tone at $2\omega_1$ with a phase of $-\phi_1$, a phase of $-2\phi_1$ is needed in order to steer the second-harmonic signal to the direction of the pilot beam.

A better approach is shown in Fig. 47. A receive antenna is nested within a subarray of transmit antennas (Fig. 48). Here the incident pilot beam phase is received and conjugated using the same method as shown in Fig. 46. The conjugated signal is then mixed with itself to produce a tone at $2\omega_1$ with a phase of $-2\phi_1$. The doubled, conjugated signal is transmitted from a separate transmit subarray so that the transmit beam produced by the entire phased array points in the direction of the incoming pilot signal.

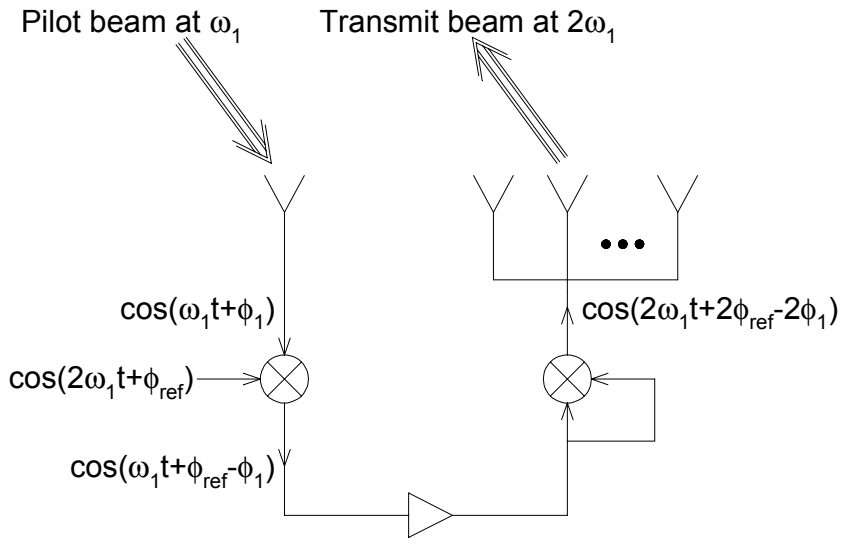

Fig. 47. A retrodirective array for the SPS system that transmits at twice the frequency of the incoming pilot beam.

A small-scale example of a 2.9-GHz receive antenna nested within a 5.8-GHz array is shown in Fig. 48.

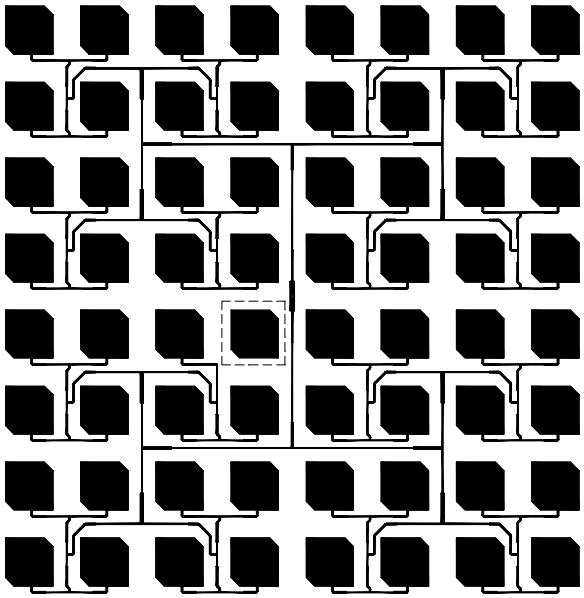

Fig. 48. A 5.8-GHz 8 x 8 circular-polarized microstrip patch antenna array. A compact 2.9-GHz patch enclosed in dashes is nested within the array. From [139].

C. Measured Results

Fig. 49 shows the block diagram of a retrodirective pair built to demonstrate the approach discussed above. Two 2.9-GHz microstrip patches receive an incoming pilot beam. The received signal is conjugated and doubled in frequency before being transmitted by two 5.8-GHz microstrip patch antenna subarrays. The phase delays of the two transceiver modules are equalized using a coaxial delay line, and the gains of the two modules are matched to within 0.5 dB. Leakage of 2.9-GHz power to the output is more than 30 dB below the main signal, and leakage of unconjugated 5.8-GHz power to the output is more than 60 dB below the main signal. Only two 5.8-GHz patches spaced

0.5λ apart are used in each subarray in order to have sufficient scanning to convincingly illustrate the retrodirective action.

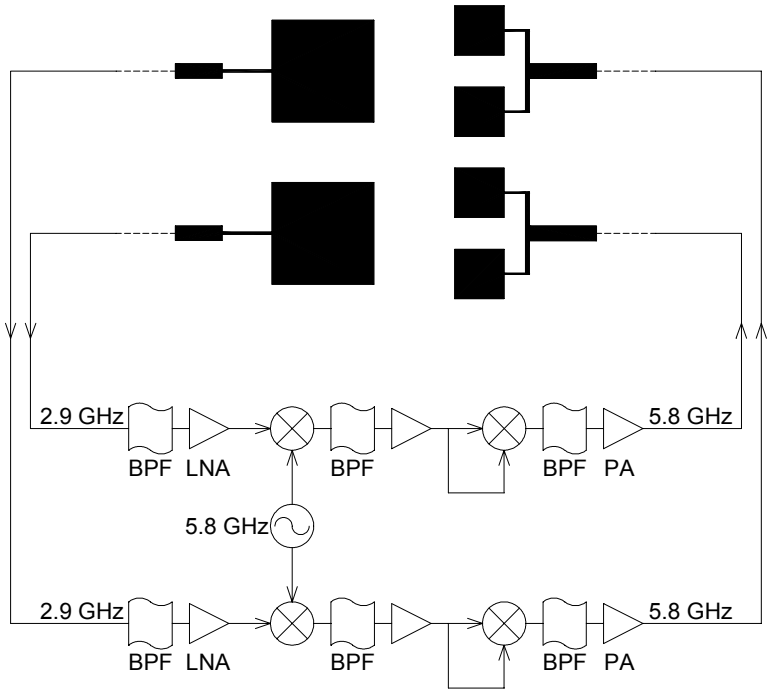

Fig. 49. Experimental demonstration of a pair of retrodirective elements that transmit a 5.8-GHz signal in the direction of a 2.9-GHz pilot beam.

The relative phase difference between the 5.8-GHz outputs of the two transceivers is tested while varying the relative phase difference at the 2.9-GHz inputs. To perform this measurement, the antenna arrays are disconnected, 2.9-GHz power is injected directly into the transceivers, and the output power is summed in-phase at 5.8 GHz using a Wilkinson combiner. A 2.9-GHz phase shifter placed at the input to one of the modules detunes the output power from its maximum value. A 5.8-GHz phase shifter placed at

the output of the same module is then tuned to restore maximum power. The phase shifters are disconnected before and after the tuning process so that their phase lengths can be measured using a network analyzer. The relative changes in phase for each tuning adjustment are plotted in Fig. 50. The 2:1 negative slope indicates that the transceivers correctly conjugate and double the phase of the received signal, thus verifying that the system operates as predicted in Fig. 47. Small deviations from the ideal curve are primarily the result of experimental errors due to flexing of the coaxial cables used and to thermal drift of the active devices.

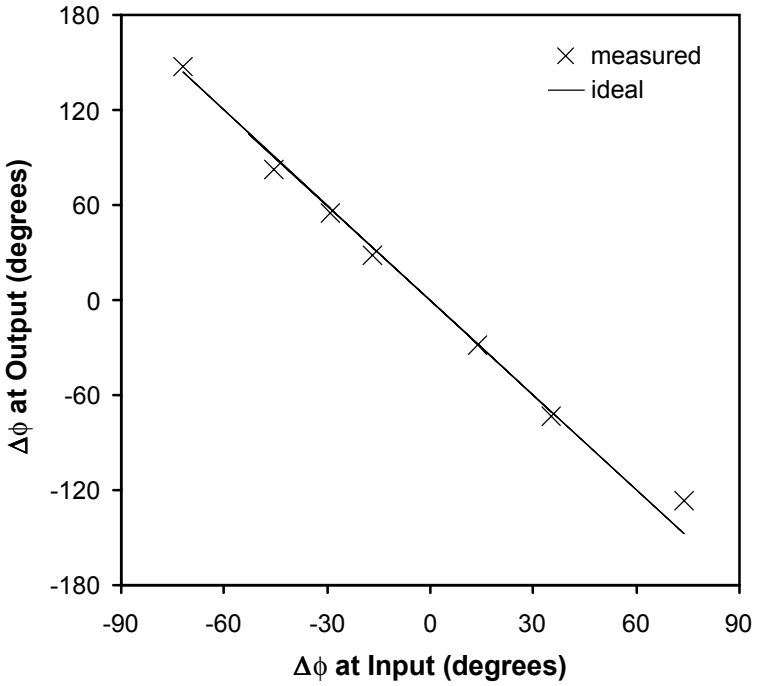

Fig. 50. Plot illustrating how the retrodirective transceiver conjugates and doubles any phase difference seen at the input.

Fig. 51 shows the measured and calculated monostatic RCS of the retrodirective transceiver across the ±10° range. This is a far-field radiation pattern measured by collocating a 2.9-GHz source and 5.8-GHz receiver in a fixed position in order to measure the power radiated at 5.8 GHz by the retrodirective array as it rotates. The resulting pattern represents the path traced by the main beam as it scans, providing evidence that the transmit beam at 5.8 GHz tracks the pilot beam signal at 2.9 GHz. Experimental errors are heavily influenced by multipath reflections in the test setup and phase/amplitude imbalances between the two subarrays. Although the beam continues to track beyond ±10°, the grating lobe becomes prohibitively large outside this range.

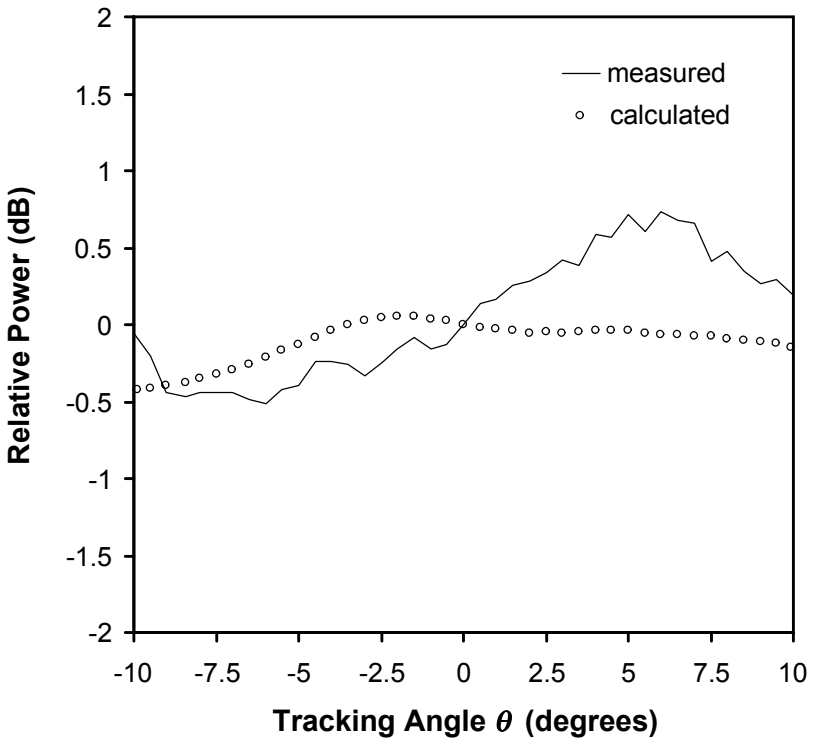

Fig. 51. Monostatic RCS measured at 5.8 GHz.

Fig. 52 illustrates measured and calculated radiation patterns that simulate the response of the retrodirective array to a pilot beam incident at 2° with respect to broadside. The measured radiation pattern is obtained by (*i*) disconnecting the 2.9-GHz antennas, (*ii*) injecting 2.9-GHz tones into the two transceivers, and (*iii*) tuning the relative phase difference between the tones so that the 5.8-GHz beam steers 2° away from broadside. The calculated curve represents the expected radiation pattern given a pilot beam signal incident at 2°. Likewise, Fig. 53 illustrates the measured and calculated radiation pattern for a pilot beam incident at 7° with respect to broadside. In both cases, measured and calculated results agree very well, indicating that the retrodirective array architecture of Fig. 47 performs as expected.

D. Summary

This chapter has demonstrated a new phased array architecture for retrodirective wireless power transmission. The design uses a second-harmonic phase-conjugating transceiver that allows a 2.9-GHz pilot beam to guide a 5.8-GHz transmit beam. When implemented together with a centrally phased reference source [138], this technique can be used to realize retrodirective phasing in large, space-based antenna arrays.

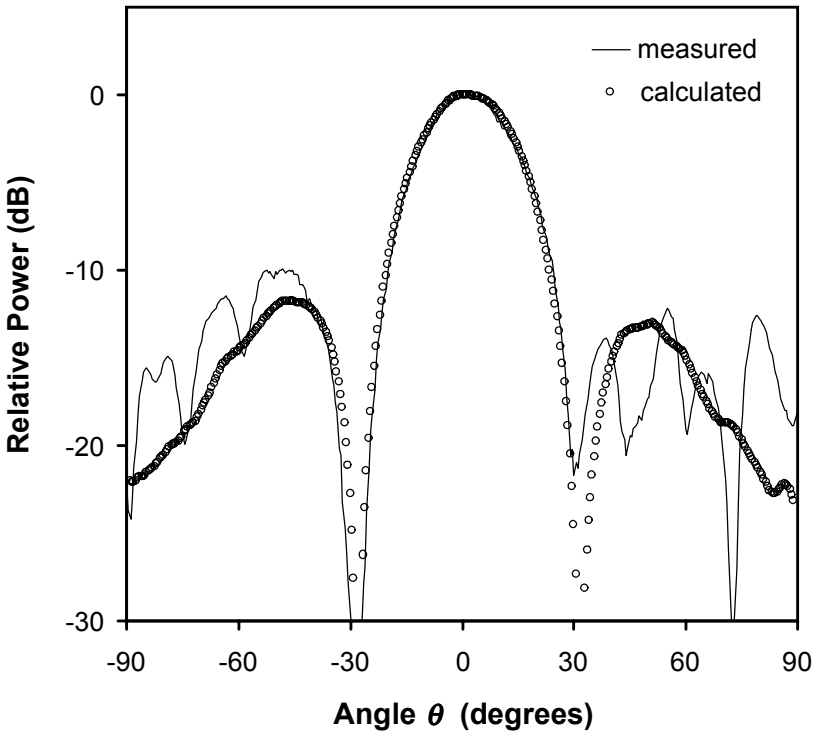

Fig. 52. Measured and calculated radiation patterns for a pilot beam incident 2° from broadside.

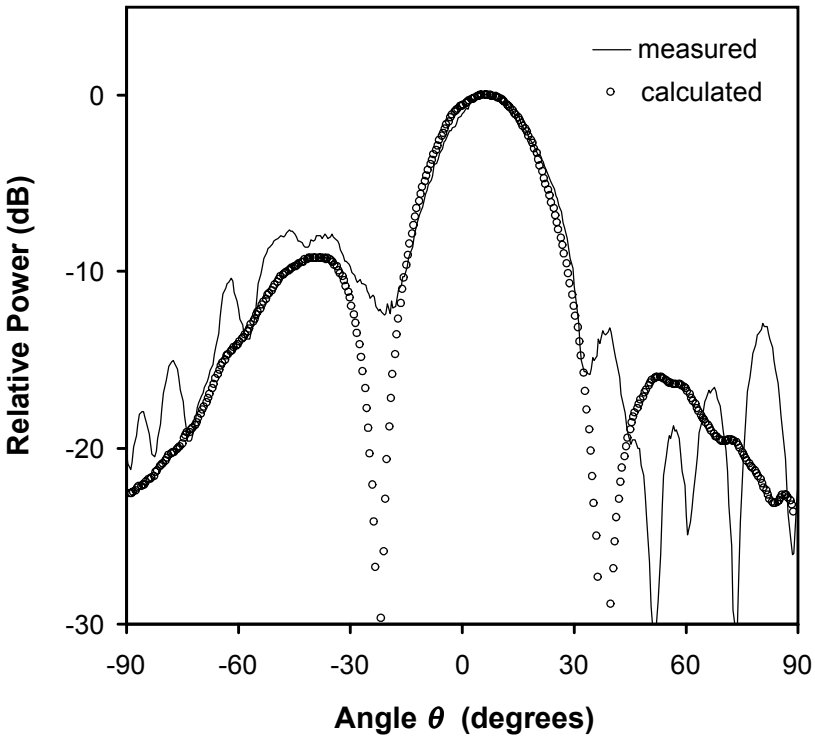

Fig. 53. Measured and calculated radiation patterns for a pilot beam incident 7° from broadside.

CHAPTER IX

CONCLUSION

Some applications of the research presented in this dissertation can be seen in the following real-life situations:

- *A light aircraft is traveling in a region where no air traffic control system is available. The pilot encounters hazardous weather and is forced to touch down on a remote airstrip. He can do so safely because his aircraft is equipped with an on-board millimeter-wave autonomous landing system.*

- *Motorists travel on a metropolitan highway at speeds in excess of 60 miles per hour, separated bumper-to-bumper by only inches. They can do so safely even in heavy traffic because their vehicles are equipped with on-board millimeter-wave collision avoidance radars networked together wirelessly within a millimeter-wave intelligent highway system.*

- *The perimeter of a highly sensitive corporate installation is kept secure without the need for the continuous presence of human guards because it is defended by a millimeter-wave intruder detection system.*

Each of the applications described above is part of a new generation of wireless technology being developed at millimeter-wave frequencies. One of the clear challenges involved in bringing such systems to market is the need for simple and inexpensive millimeter-wave phased arrays and scanning antennas. This dissertation has presented novel technologies and techniques that should dramatically reduce the cost of millimeter-wave beam steering. These include reconfigurable grating antennas, broadband phased array transceivers, and monolithic PIN diodes. In addition, this dissertation has proposed a low-cost phased-array architecture for the space solar satellite system. This work should have far-reaching impact in the future of millimeter-wave wireless technology.

A. Accomplishments

It is fitting and proper that the conclusion to a dissertation list the accomplishments of the research contained therein. Proceeding thus, Chapter III presented a novel reconfigurable antenna that achieved low loss and broad bandwidth at millimeter-wave frequencies and maintained an excellent radiation pattern across wide scan angles. The chief advantage of the invention was its extremely low cost and ease of fabrication. The design is readily scalable to frequencies up through the *W*-band and beyond.

This dissertation continued by demonstrating the versatility of this new beam steering technique. Chapter IV extended the design of the reconfigurable antenna to dual-beam operation in order to achieve beam steering across the entire ±50° range. In addition,

Chapter IV presented and validated a simple yet accurate analysis for determining the variation in the radiation pattern as the beam steers across its scan range. Finally, Chapter V adapted the method and approach of Chapter III to allow circularly polarized beam steering. Low axial ratio was achieved across a wide range of scan angles.

Chapter VI described new broadband phased array architectures for 10 to 21 GHz and 10 to 35 GHz multi-channel phased array transceivers and for an 8 to 20 GHz phased array radar. Chapter VII introduced an approach for characterizing MMIC PIN diodes. These diodes can be used to miniaturize many of the control components used in microwave and millimeter-wave phased arrays.

Chapter VIII demonstrated a new phased array architecture for retrodirective microwave power transmission from the space solar power satellite (SPS). The phased array operated entirely at RF frequencies without the need for digital control electronics.

B. Recommendations for Future Work

Several recommendations may be made regarding the new technologies and techniques presented in this dissertation.

Chapters III though V presented a novel reconfigurable grating antenna. The design should be demonstrated at *W*-band from 75 to 110 GHz in order to impress the full potential of this approach upon the technical community. The advantages of the

proposed methods should become even more clear as other scan methods become very expensive at very high frequencies. In addition, several industrial implementations of the scanning antenna are envisioned in Fig. 54. In each example, the dielectric film is wrapped around a dielectric waveguide. A simple dc motor can be used to spool the film along the waveguide much as a printing press spools paper. Two of the implementations show a dielectric waveguide embedded in a metal trough and in a flared metal trough in order to provide additional rigidity and better gain and directivity. Another suggestion, offered by Dr. J.A. Navarro of Boeing Phantom Works, is to replace the dielectric film with a flexible sheet of 1-mil-thick steel. Slots cut out of the steel film would replace the strips etched on the dielectric films used in Chapters III through V.

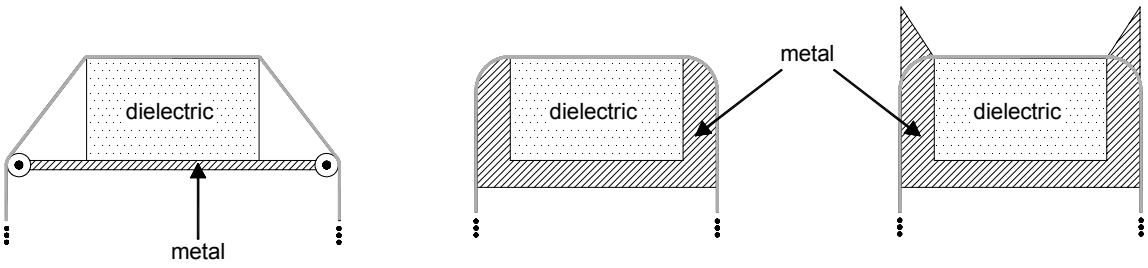

Fig. 54. Practical implementations for the novel reconfigurable antenna presented in Chapters III through V.

Chapter VI described a 10 to 21 GHz phased array transceiver and has already provided recommendations for extending that system for radar applications and for operation from 10 to 35 GHz.

The modeling methodology presented in Chapter VII is a useful tool for monolithic PIN diode design the applications of which have not yet been tapped. Additional diode layouts should be fabricated in order to demonstrate the influence of diode geometry on the extracted electrical parameters. The parameter extraction routine should continue to be executed for future production runs of standard monolithic PIN diodes in order to monitor the uniformity and reproducibility of the production process. Finally, if interest in monolithic PIN diodes continues to increase, a full nonlinear model may provide additional advantages for MMIC designers working with this technology.

Chapter VIII described a new phased array architecture for retrodirective wireless power transmission from the space solar power satellite. Although the ultimate realization of this approach is still far off, there are several steps that can be taken immediately depending on the interest of sponsoring agencies such as NASA. The new design should be compared with the previously proposed approach [138] in terms of cost, power efficiency, temperature stability, reliability, and ease of system integration. In addition, a public demonstration of a complete retrodirective wireless power transmission system should be planned.

REFERENCES

[1] G.K. Sweetnam, *The Command of Light*, Philadelphia: American Philosophical Society, 2000.

[2] M.C. Huntley, *Diffraction Gratings*, New York: Academic Press, 1982.

[3] E.G. Loewen and E. Popov, *Diffraction Gratings and Applications*, New York: Marcel Dekker, 1997.

[4] E. Hecht, *Optics*, 3rd ed., New York: Addison-Wesley, 1998.

[5] H. Hertz, *Electric Waves*, London: Macmillan and Co. Ltd., 1893.

[6] D. Pozar, *Microwave Engineering*, New York: Wiley, 1990.

[7] J.C. Bose, "On the determination of the wavelength of electric radiation by a diffraction grating," *Proc. Roy. Soc.*, vol. 60, pp. 167-178, 1897.

[8] M.L. Dakss, L. Kuhn, P.F. Heidrich, and B.A. Scott, "Grating coupler for efficient excitation of optical guided waves in thin films," *Applied Physics Lett.*, vol. 16, no. 12, pp. 523-525, June 1970.

[9] T. Itoh, "Application of gratings in a dielectric waveguide for leaky-wave antennas and band-reject filters," *IEEE Trans. Microwave Theory Tech*., vol. 25, no. 12, pp. 1134-1137, Dec. 1977.

[10] K.L. Klohn, R.E. Horn, H. Jacobs, and E. Freibergs, "Silicon waveguide frequency scanning linear array antenna," *IEEE Trans. Microwave Theory Tech*., vol. 26, no. 10, pp. 764-773, Oct. 1978.

[11] S.T. Peng and F. Schwering, "Dielectric grating antennas," U.S. Army CORADCOM, Ft. Monmouth, NJ, R&D Tech. Rep. CORADCOM 78-3, 1978.

[12] R.E. Horn, H. Jacobs, E. Freibergs, and K.L. Klohn, "Electronic modulated beam-steerable silicon waveguide array antenna," *IEEE Trans. Microwave Theory Tech*., vol. 28, no. 6, pp. 647-653, June 1980.

[13] R.E. Horn, H. Jacobs, E. Freibergs, and K.L. Klohn, "Single-frequency electronic-modulated analog line scanning using a dielectric antenna," *IEEE Trans. Microwave Theory Tech*., vol. 30, no. 5, pp. 816-820, May 1982.

[14] C.H. Walter, *Traveling Wave Antennas*. New York: McGraw-Hill, 1965.

[15] R.C. Honey, "A flush-mounted leaky-wave antenna with predictable patterns," *IEEE Trans. Antennas Propagat*., vol. 7, no. 4, pp. 320-329, Oct. 1959.

[16] J. Jacobsen, "Analytical, numerical, and experimental investigation of guided waves on a periodically strip-loaded dielectric slab," *IEEE Trans. Antennas Propagat.*, vol. 18, no. 3, pp. 379-388, May 1970.

[17] R.D. Nevels, "Periodic structures," personal notes, Department of Electrical Engineering, Texas A&M University, College Station.

[18] S.T. Peng, T. Tamir and H.L. Bertoni, "Theory of periodic dielectric waveguides," *IEEE Trans. Microwave Theory Tech*., vol. 23, no. 1, pp. 123-133, Jan. 1975.

[19] S.T. Peng, T. Tamir and H.L. Bertoni, "Correction to 'Theory of periodic dielectric waveguides'," *IEEE Trans. Microwave Theory Tech.*, vol. 24, no. 8, p. 542, Aug. 1976.

[20] P. Bhartia and I.J. Bahl, *Millimeter Wave Engineering*. New York: Wiley, 1984.

[21] A.A. Oliner, "Leaky-wave antennas," chap. 10 in *Antenna Engineering Handbook*, 3rd ed., R.C. Johnson, Ed. New York: McGraw-Hill, 1993.

[22] F.K. Schwering and S.T. Peng., "Design of dielectric grating antennas for millimeter-wave applications," *IEEE Trans. Microwave Theory Tech*., vol. 31, no. 2, pp. 199-209, Feb. 1983.

[23] S.K. Koul, *Millimeter Wave and Optical Dielectric Integrated Guides and Circuits*. New York: Wiley, 1997.

[24] M. Guglielmi and D.R. Jackson, "Broadside radiation from periodic leaky-wave antennas," *IEEE Trans. Antennas Propagat*., vol. 41, no. 1, pp. 31-37, Jan. 1993.

[25] F. Schwering and A.A. Oliner, "Millimeter-wave antennas," chap. 17 in *Antenna Handbook*, Y.T. Lo, Ed. New York: Van Nostrand Reinhold, 1988.

[26] T. Hori and T. Itanami, "Circularly polarized linear array antenna using a dielectric image line," *IEEE Trans. Microwave Theory Tech*., vol. 29, no. 9, pp. 967-970, Sept. 1981.

[27] C.T. Rodenbeck, M. Li, and K. Chang, "Circular-polarized reconfigurable grating antenna for low-cost millimeter-wave beam-steering," to appear in *IEEE Trans. Antennas Propagat.*

[28] T. Itoh and B. Adelseck, "Trapped image-guide leaky-wave antennas for millimeter-wave applications," *IEEE Trans. Antennas Propagat*., vol. 30, no. 5, pp. 505-509, May 1982.

[29] T.T. Trinh, R. Mittra, and R.J. Paleta, Jr., "Horn image-guide leaky wave antenna," *IEEE Trans. Microwave Theory Tech*., vol. 29, no. 12, pp. 1310-1314, Dec. 1981.

[30] V. Manasson and L. Sadovnik, "Scanning antenna including a dielectric waveguide and a rotatable cylinder coupled thereto," United States Patent No. 6211836 B1, U.S. Patent and Trademark Office, Apr. 2001.

[31] P. Checcacci, V. Russo, and A. Scheggi, "Holographic antennas," *IEEE Trans. Antennas Propagat.*, vol. 18, no. 6, pp. 811-813, Nov. 1970.

[32] K. Levis, A. Ittipiboon, A. Petosa, L. Roy, and P. Berini, "Ka-band dipole holographic antennas," *IEE Proc. – Microw. Antennas Propag*., vol 148, no. 2, pp. 129-132, Apr. 2001.

[33] A.E. Fathy, A. Rosen, H.S. Owen, F. McGinty, D.J. McGee, G.C. Taylor, R. Amantea, P.K. Swain, S.M. Perlow, M. ElSherbiny, "Silicon-based reconfigurable antennas-concepts, analysis, implementation, and feasibility," *IEEE Trans. Microwave Theory Tech*., vol. 51, no. 6, pp. 1650-1661, June 2003.

[34] K. Maamria, T. Wagatsuma, and T. Yoneyama, "Leaky NRD guide as a feeder for microwave planar antennas," *IEEE Trans. Antennas Propagat*., vol. 41, no. 12, pp. 1680-1686, Dec. 1993.

[35] K. Solbach, "Review of dielectric image line antennas," chap. 4 in *Infrared and Millimeter Waves*, vol. 15, K.J. Button, Ed. Orlando, FL: Academic Press, 1986.

[36] R.J. Mailloux, F.K. Schwering, A.A. Oliner, and J.W. Mink, "Antennas III: array, millimeter wave, and integrated antennas" chap. 12 in *Handbook of*

Microwave and Optical Components, vol. 1, K. Chang, Ed. New York: Wiley, 1989.

[37] C.T. Rodenbeck, M. Li, and K. Chang, "Design and analysis of a reconfigurable dual-beam grating antenna for low-cost millimeter-wave beam-steering," *IEEE Trans. Antennas Propagat*., vol. 52, no. 4, pp. 999-1006, Apr. 2004.

[38] C.T. Rodenbeck, M. Li, and K. Chang, "A novel millimeter-wave beam-steering technique using a dielectric-image line-fed grating film," *IEEE Trans. Antennas Propagat.*, vol. 51, no. 9, pp. 2203-2209, Sept. 2003.

[39] M.R. Seiler and B.M Mathena, "Millimeter-wave beam steering using 'diffraction electronics'," *IEEE Trans. Antennas Propagat*., vol. 32, no. 9, pp. 987-990, Sept. 1984.

[40] L. Huang, J.C. Chiao, and M.P. De Lisio, "An electronically switchable leaky wave antenna," *IEEE Trans. Antennas Propagat*., vol. 48, no. 11, pp. 1769-1772, Nov. 2000.

[41] A. Rosen, R. Amantea, P.J. Stabile, A.E. Fathy, D.B. Gilbert, D.W. Bechtle, W.M. Janton, F.J. McGinty, J.K. Butler, and G.A. Evans, "Investigation of active antenna arrays at 60 GHz," *IEEE Trans. Microwave Theory Tech*., vol. 43, no. 9, pp. 2117-2125, Sept. 1995.

[42] A. Alphones and M. Tsutsumi, "Leaky wave radiation from a periodically photoexcited semiconductor slab waveguide," *IEEE Trans. Microwave Theory Tech.*, vol. 43, no. 9, pp. 2435-2441, Sept. 1995.

[43] A. Alphones and M. Tsutsumi, "Leaky wave radiation of millimeter waves by photoinduced plasma grating in a semiconductor slab," *IEE Proc. – Microw. Antennas Propag.*, vol. 146, no. 1, pp. 77-83, Feb. 1999.

[44] H. Maheri, M. Tsutsumi, and N. Kumagai, "Experimental studies of magnetically scannable leaky-wave antennas having a corrugated ferrite slab/dielectric layer structure," *IEEE Trans. Antennas Propagat*., vol. 36, no. 7, pp. 911-917, July 1988.

[45] V. A. Manasson, L. S. Sadovnik, V. A. Yepishin, and D. Marker, "An optically controlled mmw beam-steering antenna based on a novel architecture," *IEEE Trans. Microwave Theory Tech.*, vol. 45, no. 8, pp. 1497-1500, Aug. 1997.

[46] H. Rutstein, personal communication, Seattle, WA, June 2002.

[47] T. Itoh and F.J. Hsu, "Distributed bragg reflector gunn oscillators for dielectric millimeter-wave integrated circuits," *IEEE Trans. Microwave Theory Tech*., vol. 82, no. 5, May 1982, pp. 724-728.

[48] J.A. Navarro and K. Chang, *Integrated Active Antennas and Spatial Power Combining*. New York: Wiley, 1996.

[49] K.B. Mallory, R.H. Miller, and P.A. Szente, "A simple grating system millimeter and submillimeter wavelength separation," *IEEE Trans. Microwave Theory Tech.*, vol. 11, no. 5, pp. 433-434, Sept. 1963.

[50] J. Meltaus, J. Salo, E. Noponen, M.M. Salomaa, V. Viikari, A. Lonnqvist, T. Koskinen, J. Saily, J. Hakli, J. Ala-Laurinaho, J. Mallat, and A.V. Raisanen,

"Millimeter-wave beam shaping using holograms," *IEEE Trans. Microwave Theory Tech*., vol. 51, no. 4, pp. 1274-1280, Apr. 2003.

[51] B. Schumann, M. Hoft, M. Saglam, H.L. Hartnagel, and R. Judaschke, "A 5 element 450 GHz HBV frequency tripler," in *Proc. IEEE MTT-S Int. Microwave Symp. Dig.*, Philadelphia, PA, June 2003, pp. 759-762.

[52] M. Hoft, J. Weinzierl, and R. Judaschke, "Broadband analysis of a *D*-band holographic power combining circuit," in *Proc. IEEE MTT-S Int. Microwave Symp. Dig*., Phoenix, AZ, May 2003, pp. 1407-1410.

[53] M. Shahabadi, K. Schunemann, "Millimeter-wave holographic power splitting/combining," *IEEE Trans. Microwave Theory Tech*., vol. 45, no. 12, pp. 2316-2323, Dec. 1997.

[54] V.A. Manasson, L.S. Sadovnik, A. Moussessian, and D.B. Rutledge, "Millimeter-wave diffraction by a photo-induced plasma grating," *IEEE Trans. Microwave Theory Tech.*, vol. 43, no. 9, pp. 2288-2290, Sept. 1995.

[55] W. Platte, S. Ruppik, and M. Guetschow, "Optically induced mask-controlled time-variable periodic microwave structures," *IEEE Trans. Microwave Theory Tech.*, vol. 48, no. 5, May 2000, pp. 846-851.

[56] G.F. Brand, "Remote millimeter-wave beam control by the illumination of a semiconductor," *IEEE Trans. Microwave Theory Tech*., vol. 48, no. 5, pp. 855-857, May 2000.

[57] R.M. Knox, "Dielectric waveguide microwave integrated circuits—an overview," *IEEE Trans. Microwave Theory Tech*., vol. 24, no. 11, pp. 806-814, Nov. 1976.

[58] T. Itoh and A. S. Herbert, "Simulation study of electronically scannable antennas and tunable filters integrated in a quasi-planar dielectric waveguide," *IEEE Trans. Microwave Theory Tech*., vol. 26, no. 12, pp. 987-991, Dec. 1978.

[59] R. Frolich and J. Litva, "Beam-steerable active array antenna," *Electron. Lett*., vol. 28, no. 2, pp. 184-185, Jan. 1992.

[60] A. Kirk and K. Chang, "Integrated image-line steerable active antennas," *Int. J. Infrared Millimeter Waves*, vol. 13, no. 6, pp. 841-851, June 1992.

[61] M.Y. Li and K. Chang, "Novel low-cost beam-steering techniques using microstrip patch-antenna arrays fed by dielectric image lines," *IEEE Trans. Antennas Propagat*., vol. 47, no. 3, pp. 453-457, Mar. 1999.

[62] M.Y. Li and K. Chang, "Novel beam-control techniques using dielectric-image-line-fed microstrip patch-antenna arrays for millimeter-wave applications," *IEEE Trans. Microwave Theory Tech.*, vol. 46, no. 11, pp. 1930-1935, Nov. 1998.

[63] I.J. Bahl, "Transmission lines," chap. 1 in *Handbook of Microwave and Optical Components*, vol. 1, Kai Chang, Ed., New York: Wiley, pp. 42-45, 1989.

[64] R.M. Knox and P.P. Toulios, "Integrated circuits for the millimeter through optical frequency range," in *Proc. Symp. Submillimeter Waves*, New York, March 1970, pp. 497-516.

[65] S. Kanamaluru, M Y. Li, and K. Chang, "Analysis and design of aperture-coupled microstrip patch antennas and arrays fed by dielectric image line," *IEEE Trans. Antennas Propagat*., vol. 44, , no. 7, pp. 964-974, July 1996.

[66] H. Tehrani, M.Y. Li, and K. Chang, "Broadband microstrip to dielectric image line transitions," *IEEE Microwave Guided Wave Lett*., vol. 10, no. 10, pp. 409-411, Oct. 2000.

[67] M. Guglielmi and H. Hochstadt, "Multimode network description of a planar periodic metal-strip grating at a dielectric interface – part III: rigorous solution," *IEEE Trans. Microwave Theory Tech*., vol. 37, no. 5, pp. 902-909, May 1989.

[68] J.A. Encinar, "Mode-matching and point-matching techniques applied to the analysis of metal-strip-loaded dielectric antennas," *IEEE Trans. Antennas Propagat*., vol. 38, no. 9, pp. 1405-1412, Sept. 1990.

[69] R. Mittra and R. Kastner, "A spectral domain approach for computing the radiation characteristics of a leaky-wave antenna for millimeter waves," *IEEE Trans. Antennas Propagat.*, vol. 29, no. 4, pp. 652-654, July 1981.

[70] "Telecommunications industry revenues: 2000," U.S. Federal Communications Commission, Industry Analysis Division, Jan. 2002, pp. XII-5.

[71] M. Richharia, *Mobile Satellite Communications: Principles and Trends*. New York: Addison-Wesley, 2001.

[72] M. Lisi, "Phased arrays for satellite communications: A system engineering approach," in *Proc. IEEE Int. Conf. Phased Array Systems Technology*, Dana Point, CA, May 2000, pp. 193-196.

[73] C. Luxey and J.M. Laheurte, "Simple design of dual-beam leaky-wave antennas in microstrips," *IEE Proc.-Microw. Antennas Propag*., vol. 144, no. 6, pp. 397-402, Dec. 1997.

[74] B. Zimmermann and W. Wiesbeck, "24 GHz microwave sensors for industrial measurement applications," *Microwave J*., vol. 39, no. 5, pp. 228-238, May 1996.

[75] J.P. Daniel, M. Himdi, and D. Thouroude, "Printed antenna arrays: Examples of commercial applications," in *Proc. 1998 IEEE AP-S Conf. Antennas and Propagation for Wireless Communications*, Waltham, MA, Nov. 1999, pp. 105-108.

[76] J. Testud and S. Oury, "The dual beam airborne technique as a tool for validation of the trmm rain radar retrieval," in *Proc. IEEE Geoscience and Remote Sensing Conf.*, Singapore, Aug. 1997, pp. 1651-1653.

[77] J. Huang and S.N. Madsen, "A dual-beam microstrip array antenna," in *Proc. IEEE AP-S Symp. Dig.*, Chicago, IL, June 1992, pp. 147-150.

[78] C.J. Wang, C.F. Jou, J.J Wu, and T.S Peng, "An active microstrip antenna for satellite communication," in *Proc. IEEE Veh. Technol. Conf*., Tokyo, May 2000, pp. 1386-1389.

[79] C.J. Wang, "Active dual-beam leaky-wave antenna with asymmetric scanning capability," *IEE Electronics Lett*., vol. 37, no. 11, pp. 672-673, May 2001.

[80] C.C. Hu, C.F. Jou, and J.J. Wu, "An aperture-coupled linear microstrip leaky-wave antenna array with two-dimensional dual-beam scanning capability," *IEEE Trans. Antennas Propag*., vol. 48, no. 6, pp. 909-913, June 2000.

[81] C.J. Wang, C.F. Jou, and J.J. Wu, "A novel two-beam scanning active leaky-wave antenna," *IEEE Trans. Antennas Propagat*., vol. 47, no. 8, pp. 1314-1317, Aug. 1999.

[82] C.J. Wang, C.F. Jou, and J.J. Wu, "A new two-terminal feeding active leaky-wave antenna," *IEEE Trans. Antennas Propagat*., vol. 46, no. 11, pp. 1749-1750, Nov. 1998.

[83] C.T. Rodenbeck, M. Li, and K. Chang, "A novel millimeter-wave beam-steering technique using a dielectric-image-line-fed grating film," in *Proc. IEEE MTT-S Int. Microwave Symp. Dig*., Phoenix, AZ, pp. 267-270, May 2001.

[84] K. Chang, M. Li, T.Y. Yun, and C.T. Rodenbeck, "Novel low-cost beam-steering techniques," *IEEE Trans. Antennas Propagat*., vol. 50, no. 5, pp. 618-627, May 2002.

[85] A. Schary, G.C. Dalman, and C.A. Lee, "Dielectric waveguide-to-coplanar transmission line transitions," United States Patent No. 5225797, U.S. Patent and Trademark Office, Jul. 1993.

[86] S. Kobayashi, R. Lampe, R. Mittra, and S. Ray, "Dielectric rod leaky-wave antennas for millimeter-wave applications," *IEEE Trans. Antennas Propagat*., vol. 29, no. 5, pp. 822-824, Sept. 1981.

[87] M. Guglielmi, "Radiation from a metal strip grating on a dielectric slab," Ph.D. dissertation, Polytechnic Univ., New York, pp. 131-152, March 1986.

[88] H. Nishihara, M. Haruna, and T. Suhara, *Optical Integrated Circuits*. New York: McGraw-Hill, pp. 62-95, 1989.

[89] M. Guglielmi and A.A. Oliner, "Multimode network description of a planar periodic metal-strip grating at a dielectric interface – part II: small-aperture and small-obstacle solutions," *IEEE Trans. Microwave Theory Tech*., vol. 37, no. 3, pp. 542-552, Mar. 1989.

[90] M. Ghomi, B. Lejay, J.L. Amalric, and H. Baudrand, "Radiation characteristics of uniform and nonuniform dielectric leaky-wave antennas," *IEEE Trans. Antennas Propagat.*, vol. 41, no. 9, pp. 1177-1186, Sept. 1993.

[91] S.D. Gedney, J.F. Lee, and R. Mittra, "A combined FEM/MoM approach to analyze the plane wave diffraction by arbitrary gratings," *IEEE Trans. Microwave Theory Tech.*, vol. 40, no. 2, pp. 363-370, Feb. 1992.

[92] M. Chen, B. Houshmand, T. Itoh, "FDTD analysis of a metal-strip-loaded dielectric leaky-wave antenna," *IEEE Trans. Antennas Propagat*., vol. 45, no. 8, pp. 1294-1301, Aug. 1997.

[93] A.F. Peterson, S.L. Ray, and R. Mittra, *Computational Methods for Electromagnetics*. New York: IEEE Press, pp. 261-297, 1998.

[94] T. Itoh and W. Menzel, "Full-wave analysis method for open microstrip structures," *IEEE Trans. Antennas Propagat*., vol. 29, , no. 1, pp. 63-67, Jan. 1981.

[95] F.B. Gross and W.J. Brown, "Two analytic frequency dependent current density approximations for TE scattering from a conducting strip grating," *IEEE Trans. Antennas Propagat.*, vol. 42, no. 7, pp. 1022-1028, July 1994.

[96] F.B. Gross and W.J. Brown, "New frequency-dependent edge mode current density approximations for TM scattering from a conducting strip grating," *IEEE Trans. Antennas Propagat.*, vol. 41, no. 9, pp. 1302-1307, Sept. 1993.

[97] R.J. Mailloux, *Phased Array Antenna Handbook*. Boston: Artech House, pp. 36-37, 1994.

[98] T.N. Trinh, J.A.G. Malherbe, and R. Mittra, "A novel metal-to-dielectric waveguide transition with application to millimeter-wave integrated circuits," in *Proc. IEEE MTT-S Int. Microwave Symp. Dig*., Washington, DC, May 1980, pp. 205-207.

[99] T. Hori and T. Itanami, "Circularly polarized linear array antenna using a dielectric image line," *IEEE Trans. Microwave Theory Tech*., vol. 29, no. 9, pp. 967-970, Sept. 1981.

[100] K. Nakaoka, "Experiments of circularly polarized printed slot array antenna," *IEE Proc. – Pt. H*, vol. 136, no. 1, pp. 70-72, Feb. 1989.

[101] K. Iigusa, T. Teshirogi, M. Fujita, S. Yamamoto, and T. Ikegami, "A slot-array antenna on coaxial cylinder with a circularly-polarized conical beam," *Electronics and Communications in Japan – Part 1*, vol. 83, no. 3, pp. 74-87, Mar. 2000.

[102] J. Hirokawa, M. Ando, and N. Goto, "Analysis of slot coupling in a radial line slot antenna for DBS reception," *IEE Proc. – Pt. H*, vol. 137, no. 5, pp. 249-254, Feb. 1990.

[103] T.Y. Yun and K. Chang, "A low-loss time-delay phase shifter controlled by piezoelectric transducer to perturb microstrip line," *IEEE Microwave Guided Wave Lett*., vol. 10, no. 3, pp. 96-98, Mar. 2000.

[104] C.L. Wang and K. Chang, "Microstrip multiplexer with four channels for broadband system applications," *Int. J. RF Microwave CAE*, vol. 11, no. 1, pp. 48-54, Jan. 2001.

[105] T.Y. Yun, C.L. Wang, P. Zepeda, C.T. Rodenbeck, M.R. Coutant, M. Li, and Kai Chang, "A 10- to 21-GHz, low-cost, multifrequency, and full-duplex phased-array antenna system," *IEEE Trans. Antennas Propagat.*, vol. 50, no. 5, pp. 641-650, May 2002.

[106] J.D. Taylor, *Ultra-Wideband Radar Technology*. Boca Raton, FL: CRC Press, 2001.

[107] J.F. White, "Semiconductor control devices: pin diodes," chap. 4 in *Handbook of Microwave and Optical Components*, vol. 2, K. Chang, Ed. New York: Wiley, 1990.

[108] J.L. Lee, D. Zych, E. Reese, and D.M. Drury, "Monolithic 2-18 GHz low loss, on-chip biased PIN diode switches", *IEEE Trans. Microwave Theory Tech*., vol. 43, no. 2, pp. 250-256, Feb. 1995.

[109] E.C. Niehenke, P.A. Stenger, and J.E. Degenford, "A GaAs MMIC PIN diode receiver protector with switchable attenuator," in *Proc. IEEE MTT-S Int. Microwave Symp. Dig*., San Francisco, CA, June 1996, pp. 1589-1592.

[110] R. Coats, J. Klein, S.D. Pritchett, and D. Zimmermann, "A low loss monolithic five-bit pin diode phase shifter," in *Proc. IEEE MTT-S Int. Microwave Symp*., Dallas, TX, May 1990, pp. 915-918.

[111] D. Seymour, D. Heston, and R. Lehmann, "X-band and Ka-band monolithic GaAs PIN diode variable attenuation limiters," in *Proc. IEEE Microwave Millimeter-Wave Monolithic Circuits Symp.*, New York, May 1988, pp. 147-150.

[112] H. Takasu, F. Sadaki, M. Kawano, and S. Kamihashi, "Ka-band low loss and high power handling GaAs PIN diode MMIC phase shifter for reflected-type phased array systems," in *Proc. IEEE MTT-S Int. Microwave Symp*., Anaheim, CA, June 1999, pp. 467-470.

[113] D. Zych, J. Beall, D. Seymour, J. Delaney, B. Mercer, J. Stidham, and M. Wdowik, "A GaAs vertical PIN diode production process," in *Proc. IEEE GaAs IC Symp. Tech. Dig*., New Orleans, LA, Oct. 1990, pp. 241-244.

[114] D. Leenov, "The silicon PIN diode as a microwave radar protector at megawatt levels," *IEEE Trans. Electron Devices*, vol. 11, no. 2, pp. 53-61, Feb. 1964.

[115] L.S. Senhouse, Jr., "Reverse biased PIN diode eqivalent circuit parameters at microwave frequencies," *IEEE Trans. Electron Devices*, vol. 13, no. 3, 314-322, Mar. 1966.

[116] A. Gopinath and H. Atwater, "Simulation of GaAs p-i-n diodes," *IEEE Trans. Electron Devices*, vol. 35, pp. 414-417, Apr. 1988.

[117] G. Pfund and P. Chen, "Measurements yield frequency-dependent PIN-diode parameters," *Microwaves & RF*, vol. 28, no. 5, pp. 151-156, May 1989.

[118] R.H. Caverly and G. Hiller, "The frequency-dependent impedance of p-i-n diodes," *IEEE Trans. Microwave Theory Tech*., vol. 37, no. 4, pp. 787-790, April 1989.

[119] R.H. Caverly and G. Hiller, "The small signal a.c. impedance of gallium arsenide and silicon p-i-n diodes," *Solid State Electronics*, vol. 33, no. 10, pp. 1255-1263, Oct. 1990.

[120] K. Fujii, Y. Hara, and H. Ishikawa, "High accuracy measurement of PIN diode parameters in microwave region," in *Proc. Asia-Pacific Microwave Conf*., Adelaide, Australia, Aug. 1992, pp. 855-858.

[121] R.H. Caverly and G. Phaneuf, "Nonlinear and transient microwave and rf modeling of the pin diode," in *Proc. IEEE Int. Symp. Circuits Systems*, Portland, OR, May 1989, pp. 2209-2214.

[123] R.H. Caverly and M.J. Quinn, "Time domain modeling of pin control and limiter diodes," in *Proc. IEEE MTT-S Int. Microwave Symp*., Anaheim, CA, June 1999, pp. 719-722.

[124] A.G.M. Strollo and E. Napoli, "Improved PIN diode circuit model with automatic parameter extraction technique," *IEE Proc – Circuits Devices Syst.*, vol. 144, no. 6, pp. 329-334, Dec. 1997.

[125] B. Shuts, L. Dunleavy, A. Fejzuli, and D. Allen, "Small signal modeling of GaAs PIN diodes aided by electromagnetic analysis," *Int. J. RF Microwave CAE*, vol. 11, no. 2, pp. 61-68, Mar. 2001.

[126] A. Fejzuli, L. Dunleavy, A. Snider, and D. Allen, "Bias-dependent small-signal modeling of GaAs PIN diodes," *Int. J. RF Microwave CAE*, vol. 11, no. 2, pp. 99-106, Mar. 2001.

[127] W. Shuts, "Microwave PIN diode modeling," Master's thesis, University of South Florida, Tampa, July 1996.

[128] D. Seymour, D. Heston, R. Lehmann, and D. Zych, "X-band monolithic GaAs PIN diode variable attenuation limiter," in *Proc. IEEE MTT-S Int. Symp*., Dallas, TX, May 1990, pp. 841-844.

[129] H.M. Olson, "p-i-n diodes," chap. 9 in *Microwave Semiconductor Devices and Their Circuit Applications*, H. A. Watson, Ed. New York: McGraw-Hill, 1969.

[130] D.G. Smith, D.D. Heston, and D.L. Allen, "Designing high-power limiter circuits with GaAs PIN diodes," in *Proc. IEEE MTT-S Int. Microwave Symp*., Anaheim, CA, June 1999, pp. 329-332.

[131] E. Alekseev, D. Pavlidis, and D. Cui, "InGaAs pin diodes for high-isolation *W*-band monolithic integrated switching applications," in *Proc. IEEE High Speed Semiconductor Devices Circuits Conf.*, Ithaca, NY, Aug. 1997, pp. 332-340.

[132] W.C. Brown, "Solar power satellites: microwaves deliver the power," *IEEE Spectrum*, vol. 16, no. 6, pp. 36-42, June 1979.

[133] J.O. McSpadden and J.C. Mankins, "Space solar power programs and microwave wireless power transmission technology," *IEEE Microwave Magazine*, vol. 3, no. 4, pp. 46-57, Dec. 2002.

[134] Solar Power Satellites, Office of Technology Assessment, US Congress, OTA-E-144, Aug. 1981.

[135] B.H. Strassner and K. Chang, "5.8-GHz circularly polarized rectifying antenna for wireless microwave power transmission," *IEEE Trans. Microwave Theory Tech.*, vol. 50, no. 8, pp. 1870-1876, Aug. 2002.

[136] G.D. Arndt and P.H. Ngo, "Wireless microwave power transmission antenna analysis," in *Proc. 53rd Int. Astronautical Congress*, Houston, TX, Oct. 2002, IAC-02-R.P.09.

[137] W.C. Brown, "Status of the microwave power transmission components for the solar power satellite," *IEEE Trans. Microwave Theory Tech*., vol. 29, no. 12, pp. 1319-1327, Dec. 1981.

[138] R.C. Chernoff, "Large active retrodirective arrays for space applications," *IEEE Trans. Antennas Propag.*, vol. 27, no. 4, pp. 489-496, July 1979.

[139] L.H. Hsieh, B.H. Strassner, S.L. Kokel, C.T. Rodenbeck, M. Li, K. Chang, F.E. Little, G.D. Arndt, and P.H. Ngo, "Development of a retrodirective wireless microwave power transmission system," in *Proc. IEEE AP-S Int. Symp. Digest*, Columbus, OH, June 2003, pp. 393-396.

VITA

Christopher Timothy Rodenbeck was born in Southern Illinois in March 1977. He received the B.S. degree (summa cum laude) in electrical engineering from Texas A&M University in 1999 and the M.S. degree in electrical engineering from the same university in 2001. He is the grateful recipient of a National Merit Scholarship, a fellowship from the State of Texas "to advance the state of the art in telecommunications," a NASA-TGSC Graduate Fellowship, and a Texas A&M Graduate Merit Fellowship. His graduate research projects have been supported by grants from the NSF, U.S. Air Force, NASA Jet Propulsion Laboratory, NASA Glenn Research Center, U.S. Army, U.S. Navy, Raytheon, and TriQuint Semiconductor. During the summer months of 1998, 1999, and 2000, he worked in Dallas for TriQuint Semiconductor as an intern in the MMIC design group.

Dr. Rodenbeck can be contacted c/o Professor Kai Chang, Texas A&M University, Department of Electrical Engineering, College Station, TX 77843-3128.